University of Mohamed Boudiaf-M'sila

FACULTY OF TECHNOLOGY

DEPARTMENT OF ELECTRONIC

Serial number: .....
Registration number: DE/ /

THESIS

A dissertation submitted in fulfillment of the requirements for the degree of

DOCTOR OF SCIENCES IN ELECTRONIC

Field: Electronic
Option: Micro-electronic

By: **Ali-Saoucha Salim**

Theme:

Study, fabrication and characterization of thin films for CZTS solar cells

Presented and publicly defended the 9th of May, 2024

JURY MEMBERS:

Hamza BENNACER	Professor	University of M'sila	Chairman
Idris BOUCHAMA	Professor	University of M'sila	Supervisor
Mohamed Amine GHEBOULI	Senior Lecturer	University of M'sila	Co-Supervisor
Abdelmadjid BOUHEMADOU	Professor	University of Setif	Examiner
Lahcen ZIET	Professor	University of Setif	Examiner
Abdelhak FERHAT HAMIDA	Professor	University of Setif	Examiner

2023/2024

Dedication

I dedicate this thesis

To my cherished parent, whose invaluable affection and love have been my pillars of strength.

To my wife, whose unwavering support made the completion of this work much easier

To my lovely daughters, and to my beloved sisters, brother, and all those who stood by me throughout these years.

May God protect them.

Acknowledgements

First and foremost, I extend my sincere appreciation to my advisor, **Prof. Idris BOUCHAMA**, for guiding me through my Ph.D. journey and providing continuous support throughout my academic endeavors, studies, and related research. I am deeply thankful for his patience, motivation, and immense knowledge.

I also express my profound gratitude to my Co-Supervisor **Dr. Mohamed Amine GHEBOULI** from M'sila University for his valuable inputs and feedback at key stages of the research process.

I would like to express my gratitude to all members of the Inorganic Materials Laboratory (IML) at the University of M'sila, with a special mention to **Prof. Achour DAKHOUCHE** for generously hosting and assisting me during my experimental studies. I extend my profound and respectful gratitude to **Mr. Abdelghani RAHAL** from the Unit of Emerging Materials Research (URME) at the University of Setif and **Dr. Samah BOUDOUR**, Senior Researcher in the Thin Films Development and Applications Unit (UDCMA-CRTI), for their generous reception and invaluable assistance.

Special thanks to **Pr. Hamza BENNACER**, professor at the University of M'sila for the honor of chairing the jury for my defense.

My Sharp thanks to the jury members, **Pr. Abdelmadjid BOUHEMADOU**, **Pr. Lahcen ZIET, Pr. Abdelhak FERHAT HAMIDA** from Setif University, for their keen interest in my work and gracious agreement to examine my research.

Salim Ali-Saoucha

LIST OF FIGURES

CHAPTER I: Thin-film solar cells

CHAPTER II: Performances optimization of CZTS thin film solar cells

CHAPTER III: Study of $ZnS_{1-x}O_x$ material using Wien2k package

CHAPTER IV: Fabrication and characterization of ZnO:S thin films

LIST OF TABLES

CHAPTER I: Thin-film solar cells

CHAPTER II: Application of TCO thin films as a widow layer for CZTS solar cells

CHAPTER III: Study of $ZnS_{1-x}O_x$ material using Wien2k package

CHAPTER IV: Fabrication and characterization of ZnO:S thin films

TABLE OF CONTENTS

General introduction

General introduction

Fueled by the growth in population and increasing prosperity, global energy consumption has undergone rapid expansion in recent decades, surpassing 442 EJ in 2023 from diverse sources such as oil, natural gas, nuclear energy, and renewables [1]. Regrettably, the escalating reliance on fossil fuels and nuclear energy presents substantial environmental challenges, with total carbon dioxide emissions reaching 40.7 Gt CO_2 yr^{-1} in 2022 [2]. In response to these challenges and in pursuit of a sustainable future, renewable energies, particularly solar power, have played a pivotal role in addressing climate change and moving towards sustainability. Solar electricity, including solar photovoltaics, is projected to contribute approximately 20.2% to global electric power by 2026 [3].

As the industry progresses, researchers persist in the exploration of novel materials and technologies. Promising advancements, such as thin film solar cells and tandem solar cells, are anticipated to enhance efficiency and lower costs. Additionally, the integration of solar cells into building materials and wearable devices has become a notable area of interest, creating fresh opportunities for energy generation.

The initial generation of solar cells employs silicon wafers, the oldest and most widely used material, known for its relatively high-power conversion efficiencies ranging from 10.5% to 26.8% [4]. However, the production and manufacturing costs associated with silicon wafers are relatively high. To tackle this challenge, thin films composed of cost-effective materials such as amorphous silicon, Cadmium Telluride (CdTe), and $Cu_2ZnSn(S,Se_2)$ have been utilized. These thin films are produced using methods like spin-coating, sputtering, plasma-enhanced chemical vapor deposition, and physical vapor deposition. The highest recorded power conversion efficiency (PCE) for thin-film technology solar cells falls within the range of 21.1% to 23.3% [4].

Among these materials, CZTS and CZTSe absorbers present a more sustainable and environmentally friendly option when compared to CIGS, CdTe, and CIS. Their direct energy bandgaps, ranging from 1 eV to 1.5 eV [5], position them favorably for efficient absorption of solar radiation, with a high optical absorption coefficient exceeding 10^4 cm^{-1} [6]. This characteristic allows for reduced material usage, typically resulting in a thinner absorber layer typically around 2 µm, while still maintaining high performance [7,8,9].

The selection of absorber material is contingent upon several factors, encompassing cost, efficiency, stability, and compatibility with other layers in the solar cell structure,

particularly the back contact and the buffer. Computational software tools such as Wien2k, CASTEP, offer the capability to scrutinize the structural, electronic, and optical properties of these materials, while software tools such as AMPS, SCAPS, and Silvaco simulate various configurations for CZTS solar cells.

This study aims to delve into CZTS thin-film solar cells, commencing with numerical modeling of conventional CZTS solar cells and proposing diverse layer materials and parameter optimizations. The second facet involves the practical implementation and characterization of Sulfur-doped ZnO, a pivotal Transparent Conductive Oxide (TCO) extensively used in CZTS thin-film solar cells, serving as either a buffer or a window layer [10-12].

In the inaugural chapter of this thesis, we introduce the foundational concepts of semiconductors and photovoltaics, elucidating the electrical models applied to general photovoltaic cells. To estimate the five parameters of the one-diode model for a commercial solar module (MSX60) [13], we employ iterative methods and vertical optimization methods grounded in genetic algorithms.

The second chapter employs (2D) Silvaco/TCAD tool to project the electrical and optical characteristics, encompassing current-voltage traits and quantum efficiency, of a substrate Mo/CZTS/CdS/ZnO/ZnO:Al thin-film solar cell. Several materials, including In_2S_3, ZnS, and ZnO:S layers, are suggested as substitutes for the environmentally problematic CdS layer. The potential use of Molybdenum disulfide (MoS_2) [14] is also explored as both a buffer layer material and an undesired BSF layer. A bifacial CZTS solar cell, achieving an efficiency of 15.7% [15] under front side illumination, is simulated using AMPS-1D software. The final configuration discussed in this chapter employs the CZTSe absorber to construct a tandem CZTS/CZTSe solar cell.

The third chapter delves into examining how different concentrations of oxygen impact the structural, electronic, and optical characteristics of the $ZnS_{1-x}O_x$ alloy within the wurtzite crystal structure, utilizing the Wien2k computer package. Computational analyses are executed to scrutinize the structural, electronic, and optical properties of the $ZnS_{1-x}O_x$ alloy.

In the final chapter, we delve into the production of Sulfur-doped ZnO thin films, presenting the experimental conditions and procedural steps essential for generating and assessing thin films of ZnO material. This involves ZnS film, undoped ZnO film and sulfur-

doped with various sulfur concentrations: 0%, 2%, 4%, 8%, utilizing the Sol-Gel spin coating method. The assessment of the resulting thin films is conducted through various techniques, including X-ray diffraction (XRD), atomic force microscopy (AFM), and UV-Visible spectrophotometry.

References

[1] International Energy Agency (IEA). World Energy Outlook 2023. https://iea.blob.core.windows.net/assets/86ede39e-4436-42d7-ba2a-edf61467e070/WorldEnergyOutlook2023.pdf

[2] Friedlingstein, P. et al. "Global Carbon Budget 2023." Earth Syst. Sci. Data, vol. 15, no. 12, 2023, pp. 5301-5369, doi:10.5194/essd-15-5301-2023.

[3] International Energy Agency (IEA). Renewables 2022. https://iea.blob.core.windows.net/assets/ada7af90-e280-46c4-a577-df2e4fb44254/Renewables2022.pdf

[4] Green, Martin A. et al. "Solar Cell Efficiency Tables (Version 63)." Progress in Photovoltaics: Research and Applications, vol. 32, no. 1, 2023, pp. 3-13, doi:10.1002/pip.3750.

[5] Pandharkar, Subhash et al. "Probing the Effect of Selenium Substitution in Kesterite-Cu_2ZnSnS_4 Nanocrystals Prepared by Hot Injection Method." Journal of Materials Science: Materials in Electronics, vol. 30, no. 15, 2019, pp. 14781-90, doi:10.1007/s10854-019-01851-7.

[6] Rondiya, Sachin et al. "CZTS/CdS: Interface Properties and Band Alignment Study Towards Photovoltaic Applications." Journal of Materials Science: Materials in Electronics, vol. 29, no. 5, 2017, pp. 4201-4210, doi:10.1007/s10854-017-8365-5.

[7] Jhuma, Farjana Akter et al. "Towards High-Efficiency CZTS Solar Cell through Buffer Layer Optimization." Materials for Renewable and Sustainable Energy, vol. 8, no. 1, 2019, doi:10.1007/s40243-019-0144-1.

[8] Prabeesh, P. et al. "CZTS Solar Cell with Non-Toxic Buffer Layer: A Study on the Sulphurization Temperature and Absorber Layer Thickness." Solar Energy, vol. 207, 2020, pp. 419-27, doi:10.1016/j.solener.2020.06.103.

[9] Devendra, K. C. et al. "Enhanced Solar Cell Efficiency: Copper Zinc Tin Sulfide Absorber Thickness and Defect Density Analysis." Journal of Materials Science: Materials in Electronics, vol. 34, no. 24, 2023, doi:10.1007/s10854-023-11125-y.

[10] Buffiere, M. et al. "Effect of the Chemical Composition of Co-Sputtered Zn(O,S) Buffer Layers on $Cu(In,Ga)Se_2$ Solar Cell Performance." physica status solidi (a), vol. 212, no. 2, 2015, pp. 282 - 290, doi:10.1002/pssa.201431388.

[11] Hsieh, Tsung-Min et al. "Characterizations of Chemical Bath-Deposited Zinc Oxysulfide Films and the Effects of Their Annealing on Copper–Indium–Gallium–Selenide Solar Cell Efficiency." Journal of Power Sources, vol. 246, 2014, pp. 443-448, doi:10.1016/j.jpowsour.2013.07.090.

[12] Minemoto, Takashi et al. "Sputtered ZnO-Based Buffer Layer for Band Offset Control in Cu(in,Ga)Se2 Solar Cells." Thin Solid Films, vol. 519, no. 21, 2011, pp. 7568-7571, doi:10.1016/j.tsf.2010.12.117.

[13] http://www.solarelectricsupply.com/media/sparsh/product_attachment/custom/upload/Solarex-MSX64.pdf, Consulted on June 18, 2023.

[14] Musztyfaga-Staszuk, Małgorzata et al. "Review of the Chosen Methods of Producing Front Contacts to Transparent Conductive Oxides Layers in Photovoltaic Structures." Energies, vol. 15, no. 23, 2022, doi:10.3390/en15239026.

[15] Bouchama, Idris and Salim Ali-Saoucha. "Effect of Wide Band-Gap TCO Properties on the Bifacial CZTS Thin-Films Solar Cells Performances." Optik, vol. 144, 2017, pp. 370-377, doi:10.1016/j.ijleo.2017.07.009.

Chapter I: Thin-film solar cells

Chapter I

Thin-film solar cells

I.1 Introduction

Driven by population growth and increasing prosperity, global energy consumption has experienced rapid growth in recent decades, exceeding 440 EJ in 2021 across various sources such as oil, natural gas, nuclear energy, and renewables [1]. Unfortunately, the escalating use of fossil fuels remains the primary contributor to climate change and poses significant environmental challenges. In 2021, global CO_2 emissions from energy and industrial processes reached 36.1 billion metric tons [2]. Although nuclear energy does not directly emit carbon dioxide, it presents substantial risks to human safety and the environment due to potential accidents and the long-term management of nuclear waste.

To address these concerns and strive for a sustainable future, renewable energies, particularly solar energy, have emerged as a crucial solution. The solar potential on Earth is immense, estimated to be around 10.000 times the current energy consumption of humanity. Solar electricity, including solar photovoltaics is projected to play a significant role, accounting for approximately 20.2% of global electric power by 2026 [3]. Fig. I.1 present the cumulative power in function of technology where the photovoltaic energy evaluated quickly between 2010 and 2027.

In this chapter, we provide the fundamental principles of photovoltaic solar cells. We begin by discussing key concepts in the field of solar energy, including solar radiation and air mass. Next, we explain the p-n junction and the photovoltaic effect. We then delve into the functioning and structure of standard photovoltaic cells, exploring their main characteristics and the equivalent circuit model. Additionally, we discuss the various generations of photovoltaic cells. Finally, we present the composition of the cell structure.

I.2 History of solar cells

The history of solar cells leading up to 2023 is a tale of innovation, research, and technological advancements. It all began in 1839 when the French physicist Alexandre-Edmond Becquerel discovered the photovoltaic effect, establishing the foundation for solar cell development [4]. However, practical applications did not emerge until much later. In 1954, Bell Laboratories in the United States achieved a significant breakthrough by creating

the first silicon solar cell, with a conversion efficiency of around 6% significantly higher than the previous selenium cells [5,6].

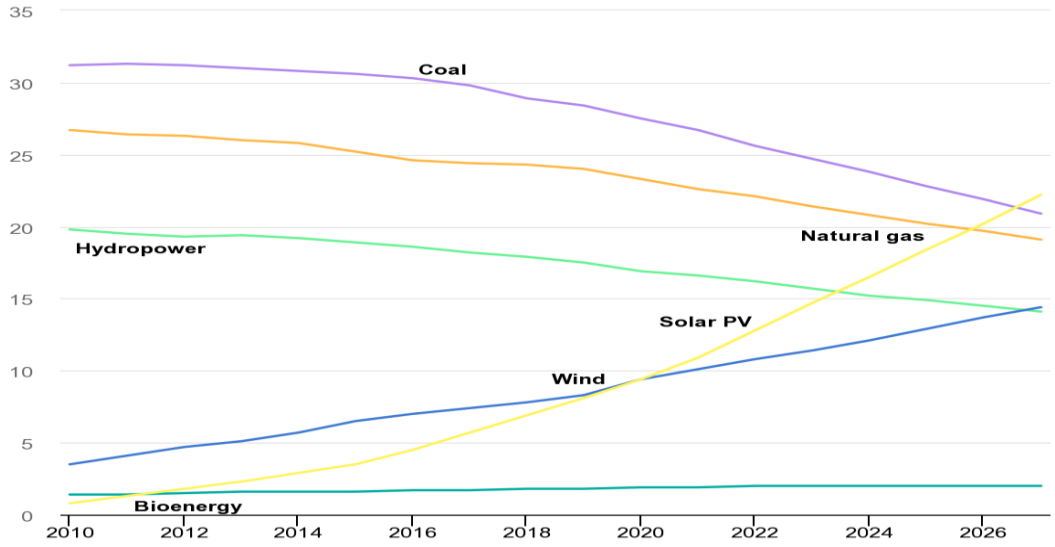

Fig. I.1: Cumulative power capacity in function of technology between 2010 - 2027 [3].

During the following decades, researchers and engineers focused on improving efficiency and reducing costs. In the 1970s, spurred by the global energy crisis and nuclear power plants incidents such Three Mile Island (USA 1979) and Tchernobyl (URSS 1986), solar energy gained attention as a viable alternative to fossil fuels. Governments and organizations began investing in research and development, leading to steady progress in solar cell efficiency. By the 1980s, the efficiency had reached around 20%, opening up new possibilities for practical applications.

In the 1990s and early 2000s, advancements in manufacturing techniques and material innovations, such as thin-film solar cells, emerged. These developments allowed for more cost-effective production and expanded the potential applications of solar cells. Additionally, governments worldwide introduced incentives like feed-in tariffs and tax credits to promote solar energy adoption, which further accelerated the growth of the industry.

By the early 21st century, solar cells became increasingly common on rooftops, powering homes and businesses. The push for renewable energy and sustainability led to substantial investments in solar power infrastructure, including the establishment of large-scale solar farms and utility-scale installations.

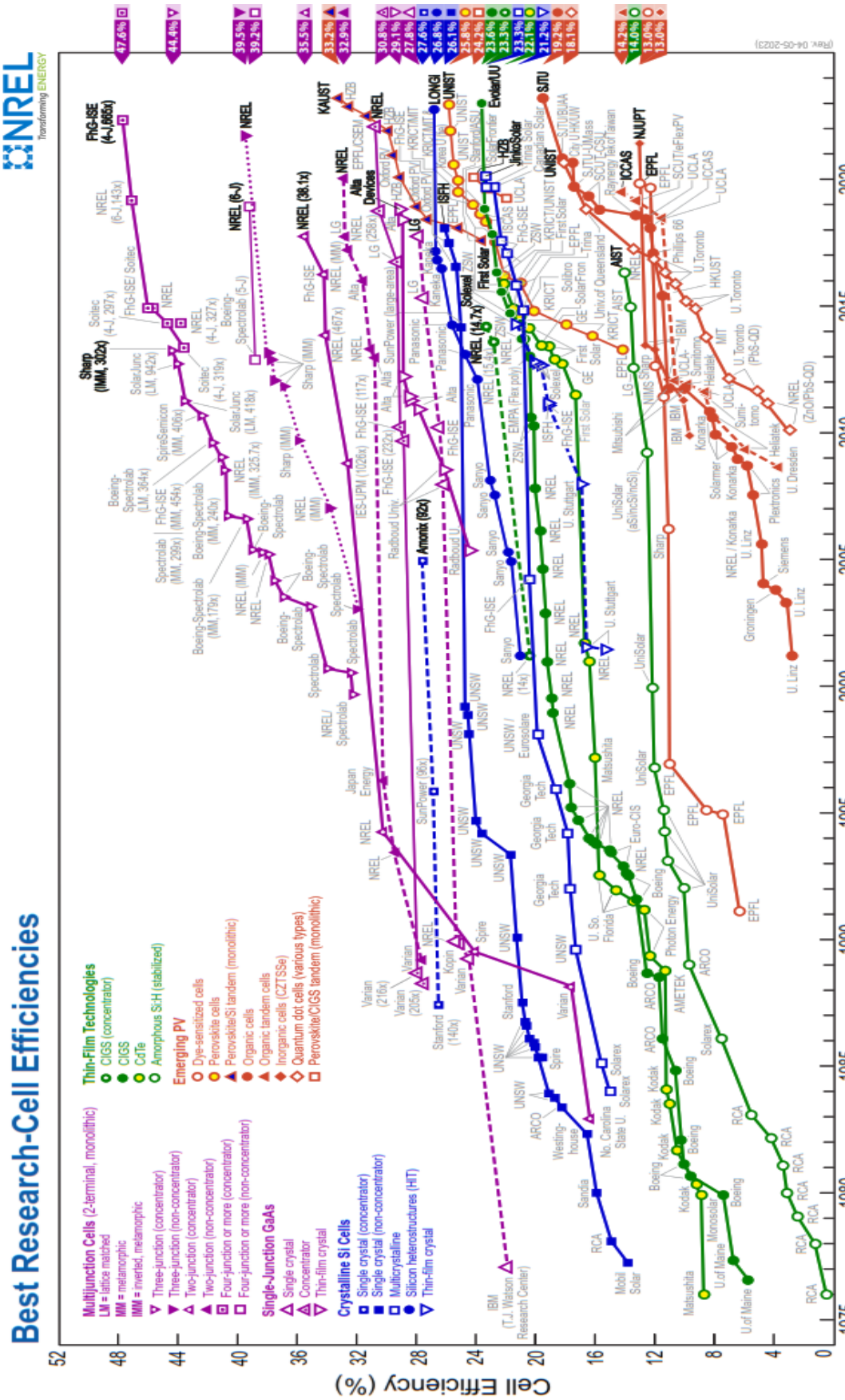

Fig. I.2: The highest confirmed conversion efficiencies for research cells for a range of photovoltaic technologies from 1976 (Rev.04/06/2023) [7].

As the industry progressed, researchers continued to explore new materials and technologies. Emerging technologies like perovskite solar cells and tandem solar cells showed promise in increasing efficiency and reducing costs. Furthermore, the integration of solar cells into building materials and wearable devices became areas of interest, offering new avenues for energy generation.

By 2023, solar cells had become a mainstream and rapidly growing segment of the global energy landscape. With increasing efficiency levels, declining costs, and widespread adoption, solar energy played a crucial role in mitigating climate change and transitioning towards a sustainable future. Fig. I.2 show the highest confirmed conversion efficiencies for research cells for a range of photovoltaic technologies from 1976, ongoing research and development aimed to further enhance solar cell efficiency, storage capabilities, and integration into smart grids, fueling optimism for a renewable energy revolution powered by the sun.

1.3 Photovoltaic solar cell principal of function

1.3.1 Solar radiation and Air Mass

The Sun emits energy in all directions, and the Earth receives a portion of this energy as it intercepts the solar radiation. At the top of the Earth's atmosphere, the power flux of solar radiation is measured at 1400 Watts/m^2. However, the Earth's relatively dense atmosphere filters out about 400 Watts/m^2 [8], including a significant portion of ultraviolet rays. These radiations belong to the electromagnetic spectrum, which spans from ultraviolet to infrared wavelengths, with the visible spectrum having the highest intensity.

The solar radiation reaching the Earth's surface is influenced by the atmospheric thickness that the light rays traverse, resulting in spatial variations across the globe. To account for the energy loss due to atmospheric absorption, the concept of "Air Mass" is introduced and represented as AMx. The Air Mass value is calculated using the formula $AM = 1/\sin \theta$, where θ represents the solar elevation angle, as illustrated in Fig. I.3, ‘θ’ is the angle between the solar radiation and the horizontal plane on Earth.

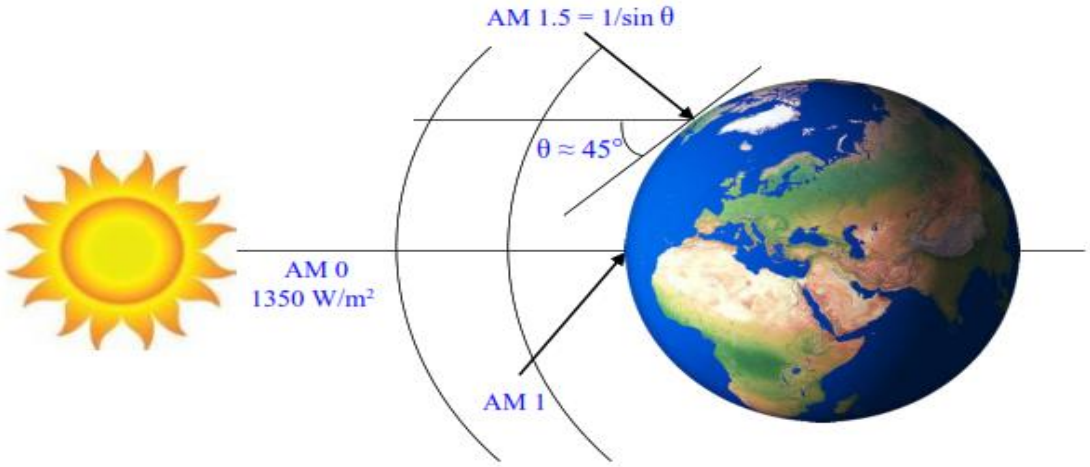

Fig. I.3: Air mass in function of sun height angle (θ).

Fig. I.4 illustrates the spectrum of solar irradiation. Different standards, specifically ASTM G173-03 [9], are employed to describe these spectra: AM0 refers to the solar spectrum observed by satellites outside the atmosphere, characterized by an integrated power density of 1367 W/m^2. Solar cells designed for space applications are optimized for this particular spectrum. AM1.5 represents the spectrum of direct sunlight reaching the Earth's surface when the sun's rays pass through the atmosphere 1.5 times. This corresponds to a zenith angle of 48.19°. The AM1.5 spectrum includes light from a 2.5° cone, totaling 900 W/m^2, and is utilized in concentrating solar power plants. For most applications like flat photovoltaic or thermal modules, the AM1.5G spectrum is employed, totaling 1000 W/m^2. This spectrum combines the direct light from the AM1.5 spectrums with diffuse light resulting from scattering and multiple reflections. Consequently, it intensifies the blue component of the solar spectrum.

1.3.2 Semiconductors

Semiconductors are materials that exhibit electrical properties lying between those of conductors and good insulators. When a semiconductor is undoped or in its pure form, it is referred to as an intrinsic semiconductor. In this state, semiconductors do not possess characteristics of either a good insulator or a good conductor. In terms of energy bands, semiconductors have an almost filled valence band and an empty conduction band, with a very small forbidden energy gap, as illustrated in Fig. I.5. At a temperature of absolute zero, the conduction band is devoid of electrons, while the valence band is filled. As the temperature increases, the width of the forbidden energy gap decreases. Consequently, some valence electrons gain sufficient energy to transition into the conduction band. This

phenomenon leads to an increase in the conductivity of the semiconductor with temperature [10].

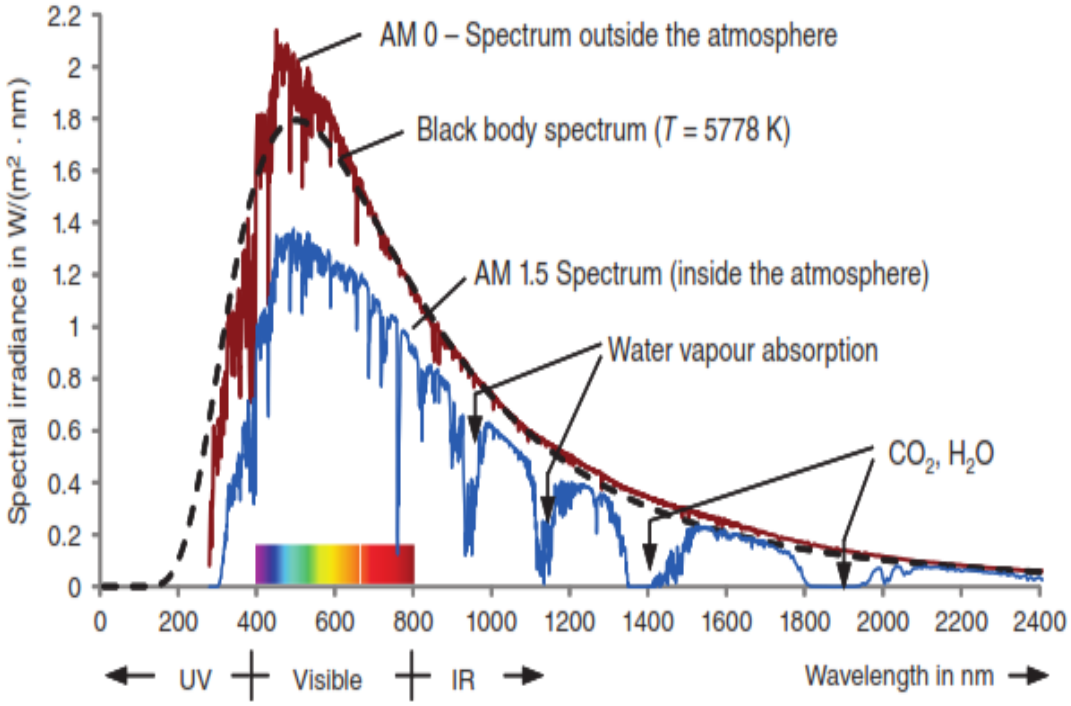

Fig. I.4: AM0 and AM1.5 spectrums, outside and inside the atmosphere [8].

Semiconductors can be composed of a single element, such as Ge and Si, or they can be compounds like ZnO, ZnS, InP, GaAs, CdTe, as well as alloys like CIGS or $CZTS_xSe_{1-x}$.

Intrinsic semiconductors have high resistance and allow only a very small amount of current to flow. However, there conducting ability can be significantly modified by introducing specific impurities. When impurities are intentionally added to intrinsic semiconductors, they are referred to as extrinsic semiconductor materials. Extrinsic semiconductors exhibit higher electrical conductivity compared to intrinsic semiconductors, making them suitable for production of electronic devices like diodes and transistors. Several substances can serve as sources of impurities, including phosphorus (P), arsenic (As), indium (In), boron (B), aluminum (Al), and gallium (Ga). Based on the nature of the added impurities (pentavalent or trivalent), two distinct types of extrinsic semiconductors can be generated.

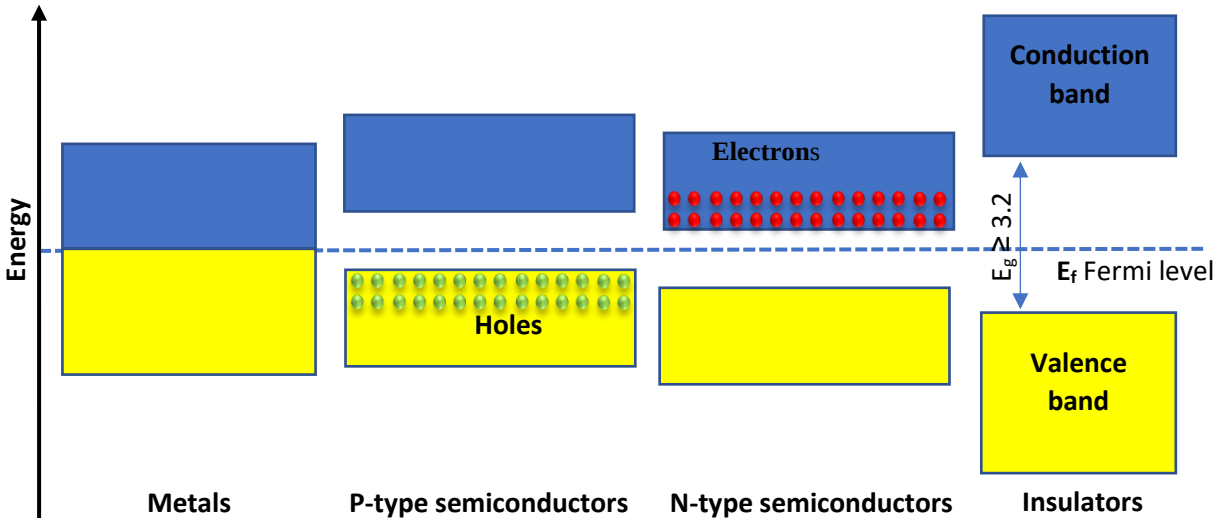

Fig. I.5: Energy diagrams of different type of materials.

P-type semiconductor

A p-type semiconductor is created by doping an intrinsic semiconductor with trivalent material (In, B, Al, and Ga). In this type of semiconductor, the majority of charge carriers are holes, resulting in a higher hole density compared to electron density. The acceptor energy level of the p-type semiconductor is situated near the valence band and away from the conduction band.

N-type semiconductor

An n-type semiconductor is formed by doping an intrinsic semiconductor with pentavalent materials (Sb, P, and As) as impurities. In this case, the majority of charge carriers are electrons, while holes are considered minority carriers. The electron density in an n-type semiconductor is significantly higher than the hole density. The donor energy level is positioned near the conduction band and away from the valence band.

I.3.3 P-N junction

To comprehend photovoltaic devices, it is essential to have a fundamental grasp of the p-n junction. A p-n junction semiconductor diode is created by introducing doping of P-type and N-type impurities onto a wafer, as depicted in Fig. I.6. The region where the two semiconductor regions meet forms a boundary interface known as the junction. The junction plane theoretically exhibits an equal density of donors and acceptors.

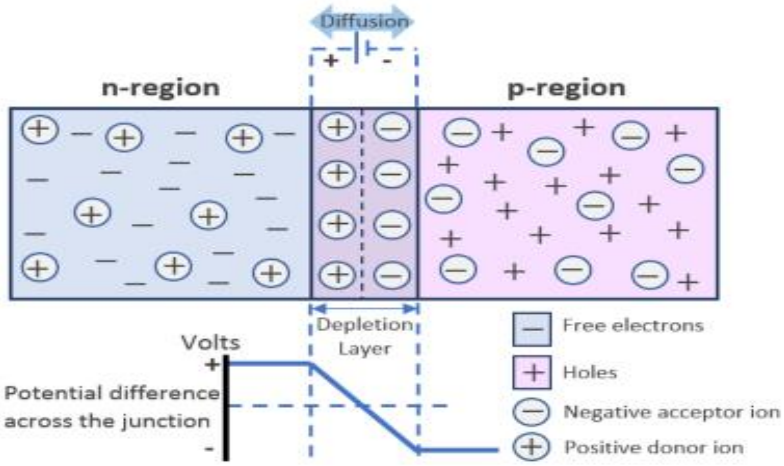

Fig. I.6: P-N junction in semiconductors.

P-N junctions are formed in single crystal semiconductors through a process called doping. Several phenomena occur at the junction: When the p-n junction is initially formed, electrons are predominantly located in the N-region, while holes are concentrated in the P-region. Electrons act as minority carriers in the P-region, whereas holes act as minority carriers in the N-region. As the p-n junction is formed, electron diffusion occurs from the N-region to the P-region, resulting in the accumulation of positive charge near the junction. Conversely, hole diffusion takes place from the P-region to the N-region, resulting in the accumulation of negative charge near the junction. This generation of positive and negative charges creates a barrier potential, also known as the depletion layer or VB, as illustrated in Fig. 1.5. The depletion layer is rapidly established across the junction and is much thinner compared to the P and N regions.

The barrier potential prevents the flow of charge carriers across the junction, unless provided with external energy from a voltage source. At room temperature (300 K), the barrier potential is approximately 0.7 V for silicon (Si) and 0.3 V for germanium (Ge).

In thermal equilibrium, the potential difference across the junction, referred to as the built-in potential or junction potential, restricts the further movement of charge carriers. The built-in potential is influenced by the doping levels of the P and N regions. when a voltage is applied to the p-n junction externally, it can be forward-biased or reverse-biased:

- **Forward bias**: When the positive terminal of the voltage source is connected to the P-side and the negative terminal to the N-side, the p-n junction is forward-biased. This reduces the potential barrier and allows the majority carriers to move across the

junction easily, resulting in a current flow. The forward biased p-n junction is commonly used in diodes and transistors.

- **Reverse bias**: When the positive terminal of the voltage source is connected to the N-side and the negative terminal to the P-side, the p-n junction is reverse-biased. This increases the potential barrier, preventing the majority carriers from crossing the junction. In this state, only a small reverse current (leakage current) flows, primarily due to the minority carriers. The reverse biased p-n junction is often used in diodes as a means of blocking current in one direction.

Usually, one can find five different types of semiconductor junctions that have application in photovoltaic solar cells, Homojunction, Heterojunction, metal-semiconductor junctions, and semiconductor-electrolyte junctions [11].

I.3.4 Photovoltaic effect

Light is made up of packets of energy, called photons, whose energy depends only upon the frequency of the light; the energy of a photon could be calculated using Planck's equation:

$$E = h\nu = c / \lambda \tag{I.1}$$

Where ν is the frequency of the light in Hz and c is the speed of light in a vacuum ($c = 3 \times 10^8 m/s$), h is the Planck's constant ($h = 6.626 \times 10^{-34}\ Js$).

When light strikes the surface of a pure metal substance and the energy surpasses a certain threshold, electrons within the material are elevated to higher energy levels. However, these excited electrons quickly return to their ground state. In a photovoltaic device, however, an inherent asymmetry prevents the electrons from relaxing and instead directs them towards an external circuit. This process, known as the photovoltaic effect as illustrated in Fig. I.7, involves three fundamental steps:

- Generation of charge carriers due to photon absorption;
- Separation of the photo generated charge carriers;
- Extraction of the photo generated charge carriers.

If the energy of the incident photon is sufficiently high ($h\nu = E_g$, where E_g is the band gap energy), the photon can cause an electron to transition from the valence band to the conduction band of the semiconductor material without energy loss, resulting in the creation of an electron-hole pair. These electrons and holes are separated by an internal

electric field at the junction and collected between a grid (front side) and a back contact (rear side), and then discharged into the load. If the photon energy is great than the band gap energy $hv > E_g$, a part of the energy is thermalized, while if hν > Eg the photon is not absorbed.

Recombination occurs between electron-hole pairs, where the electron falls back to its initial energy state and releases energy either through radiative recombination (photon emission) or non-radiative recombination (transfer of energy to other holes and electrons). The solar cell is designed in such a way that the electron-hole pairs must reach the membrane before recombination can take place. This requires the time required for these charge carriers to reach their respective membranes to be shorter than their lifetime, which imposes a limit on the thickness of the absorber.

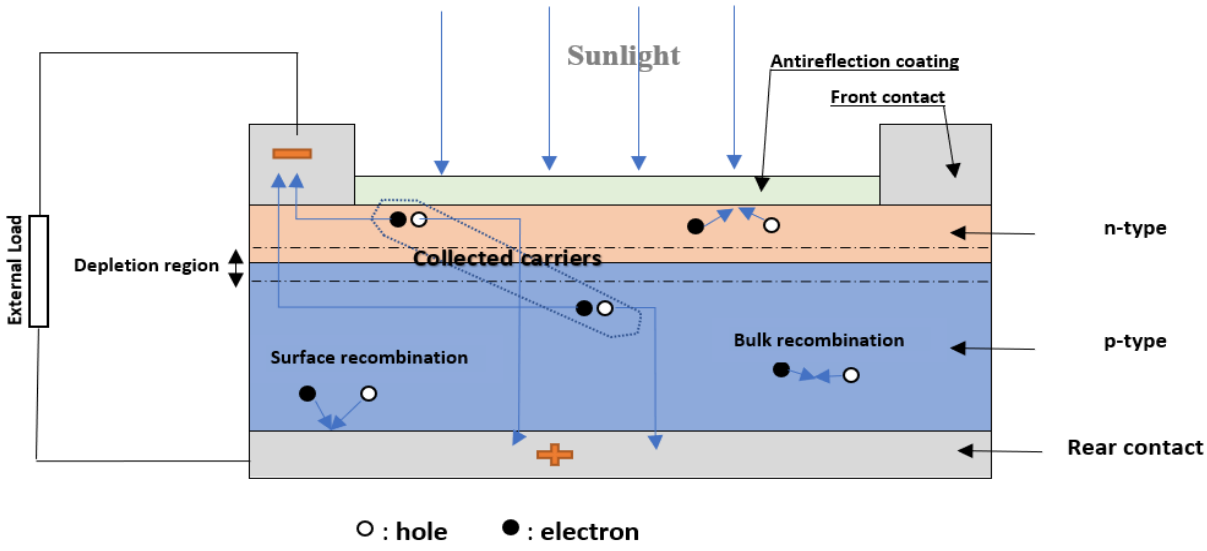

Fig. I.7: Generation, separation and collect of charge carrier by photon absorption.

I.4 Solar cells association

Solar cells are typically not used individually; instead, they are connected to form a module or panel, which enables them to generate higher power outputs. When exposed to peak sunlight conditions (100 mW/cm²), a single silicon cell can only produce a maximum voltage of around 600 mV while the maximum current delivered by a cell is approximately 30 mA/cm², to achieve the desired voltage, the cells are connected in series. For a nominal 12 Volt charging system, approximately 36 series cells are commonly employed. Additionally, to obtain the desired current, the cells are connected in parallel. Fig. I.8

illustrates a typical solar module consisting of *n* branches, with each branch composed of *m* cells connected in series.

Ideally, cells in a module are identical, so the module's current-voltage (I-V) curve would mirror the shape of the individual cells' I-V curves, albeit with a scaling change for the axes. Consequently, when *n* cells are connected in series and *m* cells are connected in parallel:

$$I_{Total} = mI_{cell} \;\&\; V_{Total} = nV_{cell} \tag{I.2}$$

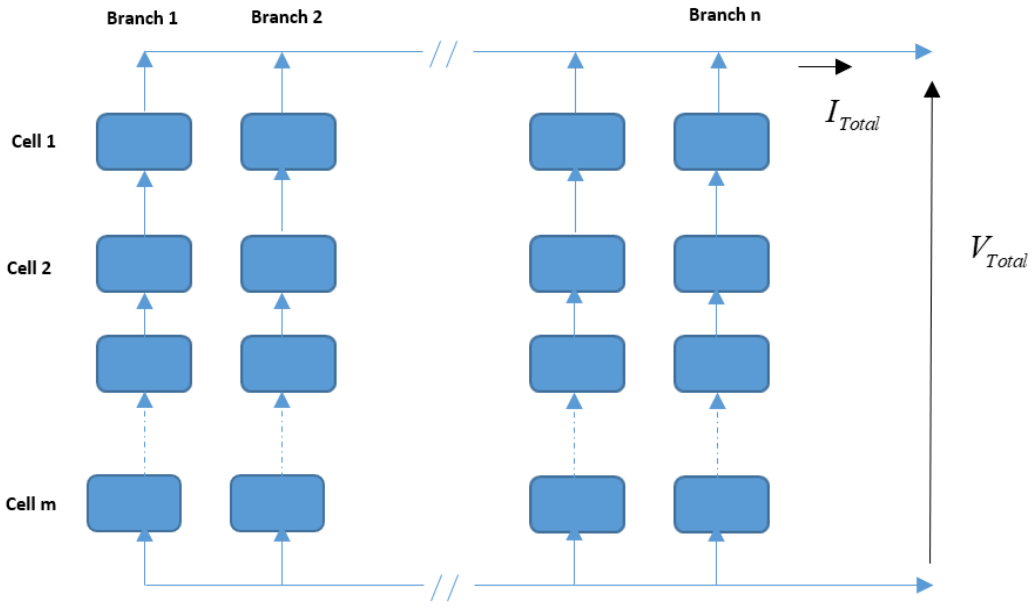

Fig. I.8: Connection of single solar cells into a module.

I.5 Modeling of photovoltaic generator

The output characteristics of a photovoltaic (PV) generator system depend on the solar insolation, the cell temperature and the output voltage of the PV module. An accurate knowledge of this characteristic curves is of vital importance to extract the maximum of the PV power and ensure the optimal use of the available solar energy. This necessitates an accurate simulation model of the PV module.

I.5.1 Photovoltaic module modeling

Illuminated current-voltage (I-V) of a solar module under different operating conditions may be described by a lumped parameter equivalent circuit model. The simplest approach represented in Fig. I.9, uses single diode model i.e. a current source in parallel to

a diode, in series with a resistor R_S which represent the internal losses due to the current flow. For more accuracy and to represent the leakage current of the p-n junction, a shunt resistance R_{Sh} must be added to the circuit in parallel to the diode.

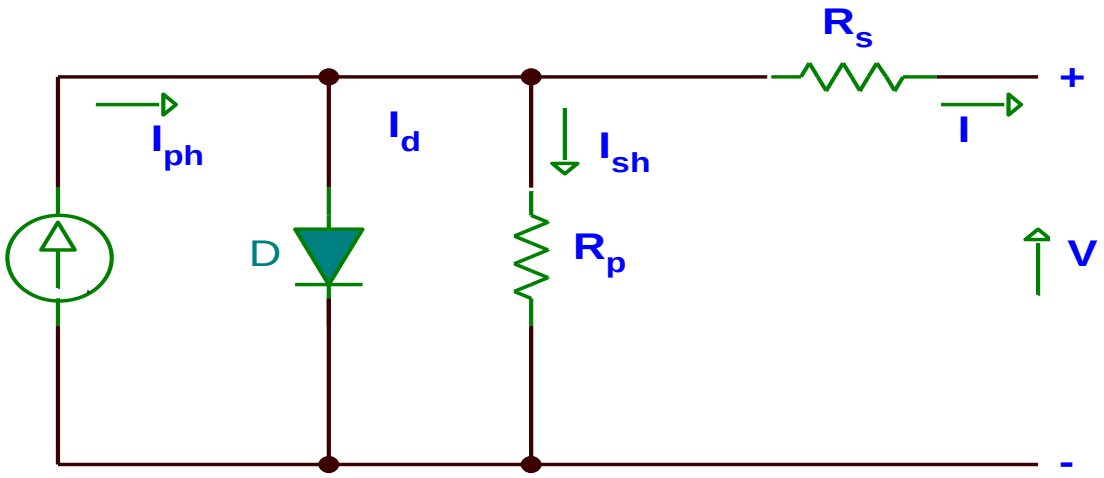

Fig. I.9: Equivalent circuit for one-diode model.

The output current for this model can be written as:

$$I = I_{ph} - I_0\left[\exp(\frac{V+IR_s}{aV_T})-1\right]-\left(\frac{V+IR_s}{R_p}\right) \qquad \text{(I.3)}$$

Where I_{ph} is the light generated current, I_0 is the reverse saturation current, $V_T = N_s kT/q$ is the thermal voltage of the entire module composed of N_s solar cells connected in series, q is the electron charge ($1.602217646 \times 10^{-19}$ C) , k is the Boltzmann constant ($1.3806503 \times 10^{-23}$ J/K), T is the cells absolute temperature in Kelvin , a is the diode ideality factor.

The single diode model is widely used in literature for its simplicity, however it doesn't take in consideration the recombination loss in the depletion region, for more accurate model a second diode must be add in parallel to the first [12] as showed in Fig. I.10. The output current for this model can be written as:

$$I = I_{ph} - \sum_{i=1}^{2} I_{0i}\left[\exp(\frac{V+IR_s}{aV_T})-1\right]-\left(\frac{V+IR_s}{R_p}\right) \qquad \text{(I.4)}$$

Where I_{01} and I_{02} are the reverse saturation current for diode 1 and diode 2, a_1 and a_2 are the diode ideality factors.

Although a significant improvement is achieved, the double-diodes model demands significant computational effort. The single-diode model is preferred for its simplicity.

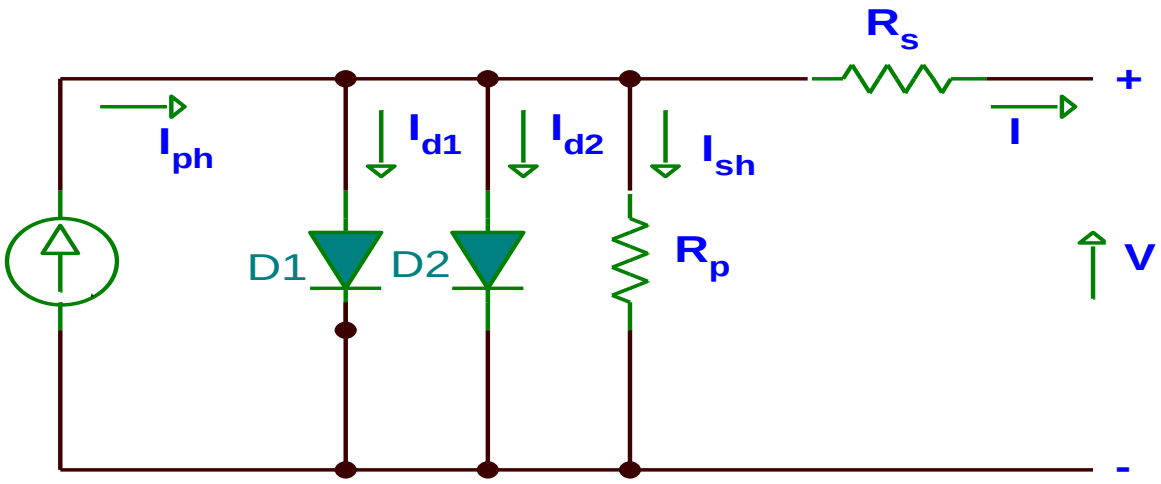

Fig. I.10: Equivalent circuit for double-diodes model.

I.5.2 Numerical methods for PV cells simulation

The implicit transcendental equation (I.3) can't be solved explicitly for I or V using common elementary functions but can be solved using numerical methods such Newton-Raphson's method with is widely used in iterative computational application to find the roots of nonlinear equations for its simplicity and fast convergence. From (I.3) we can get:

$$F(I) = I - I_{ph} + I_0\left[\exp(\frac{V+IR_s}{aV_T}) - 1\right] + \left(\frac{V+IR_s}{R_p}\right) = 0 \qquad \text{(I.5)}$$

The roots of (I.5) can be iteratively estimated as:

$$I_{n+1} = I_n - \frac{F(I_n)}{F'(I_n)} \qquad \text{(I.6)}$$

Ortiz-Conde et al propose to use the Lambert function to get an exact explicit analytical solution for (3) [13]:

$$I = \frac{aV_T}{R_s} W_0\left\{\frac{I_0 R_s}{aV(1+\frac{R_s}{R_p})}\exp\left[\frac{V+R_s(I_0+I_{ph})}{aV_T(1+\frac{R_s}{R_p})}\right]\right\} + \left(\frac{V/Rp-(I_0-I_{ph})}{aV_T(1+\frac{R_s}{R_p})}\right) = 0 \qquad \text{(I.7)}$$

where "W_0" is the principal branch of the Lambert W function.

Fig. I.11 and Fig. 1.12 show result of simulation of of '*MSX60* module' a commercial polycrystalline silicon cell from *SOLAREX* for various temperatures and irradiation levels,

respectively. Table I.1 presents '*MSX60* module' characteristics given in the datasheet at the STC [14].

Table I.1: Parameters of msx60 solar module at 25°C, AM1.5, 1 kw/m^2.

V_{mp}	17.1V
I_{mp}	3.5A
I_{sc}	3.8A
V_{oc}	21.1V
K_i	3 mA/°C
K_v	-(80±10)mV/°C
N_s	36

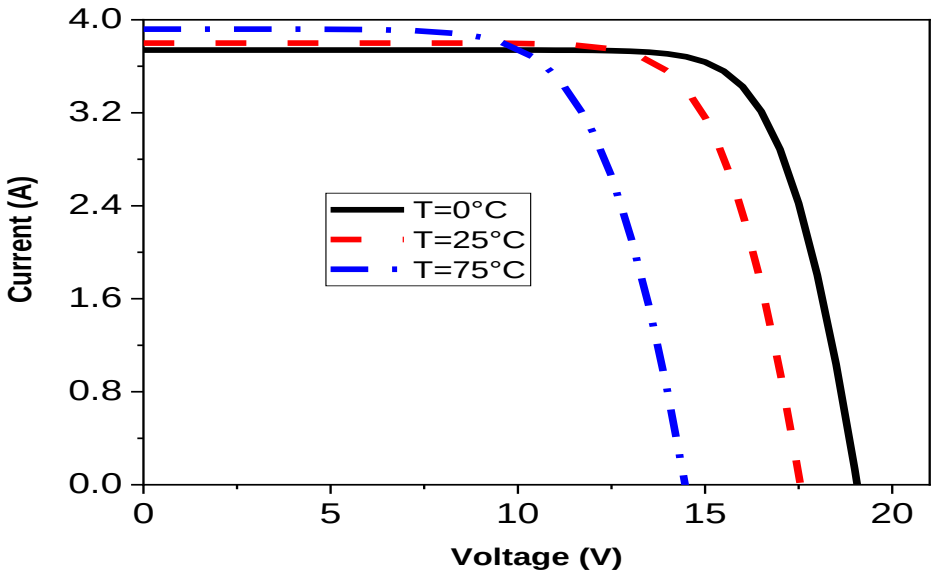

Fig. I.11: I-V curves for various temperatures (MSX-60, G = 1 kW/m²).

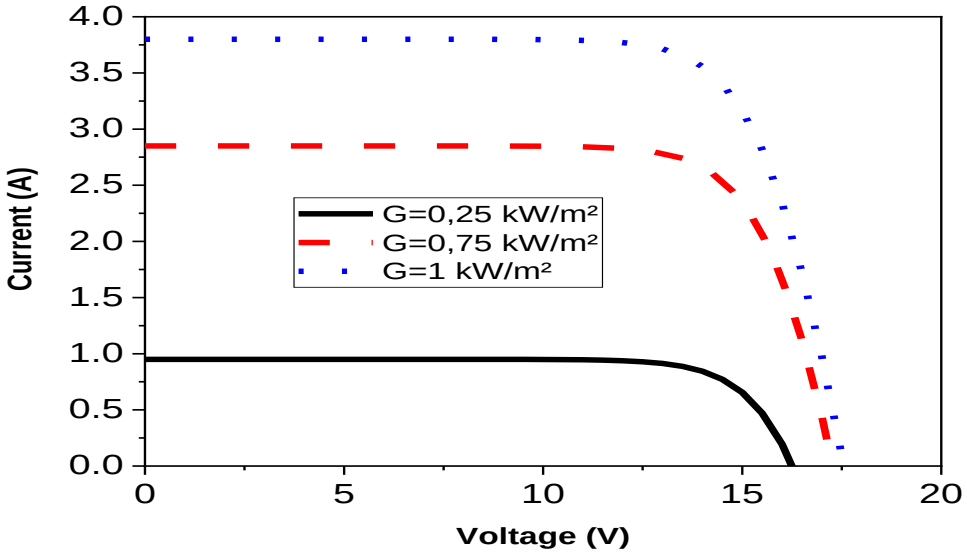

Fig. I.12: I-V curves for various irradiation (MSX-60, T = 25°C).

1.5.3 Model parameters extraction

In literature several methods are proposed to estimate the five parameters of the one-diode model:

a) Iterative methods

The aim of the iterative method is to use only the minimum information usually given by the manufacturer in the module datasheet to find the value of Rs and Rp [15]. The datasheet brings the following experimental information with reference to standard test conditions (STC):

- The nominal Open-Circuit ($V_{oc,n}$).
- The nominal Short-Circuit ($I_{sc,n}$).
- The current (I_{mp}) and the voltage (V_{mp}) at the maximum power point (MPP).

The equation for the light-generated current as a function of temperature and irradiance can be written as:

$$I_{ph} = \frac{G}{G_n}\left[I_{ph,n} + k_i (T - T_n) \right] \tag{I.8}$$

where K_i is the short circuit current coefficient, $I_{Ph,n}$, G_n, T_n are the light generated current, the irradiance and the temperature under STC.

The diode saturation current is strongly dependent on temperature. At the STC it can be expressed as [8]:

$$I_{0,n} = \frac{I_{sc,n}}{\exp(V_{oc,n} / aV_T) - 1} \tag{I.9}$$

An equation to describe the saturation current in function of the temperature variations is given by:

$$I_0 = \frac{I_{sc,n} + K_i (T - T_n)}{\exp\left[(V_{oc,n} + K_v (T - T_n) / aV_T) \right] - 1} \tag{I.10}$$

where K_v is the Open-Circuit voltage coefficient.

The constant a represent the degree of ideality of the diode, usually chosen arbitrary between 1 and 2. So three parameters of the one-diode model are easily determined. The two remaining parameters R_s and R_p may be estimated based on the fact that there is only one

pair (R_s, R_p) that verified that the estimated maximum power ($PM_{,max}$) calculated based on (3) is equal to the maximum power ($PE_{,max}$) given by the manufacturer, R_s is slowly increment starting from R_s =0. This requires several iterations until $PM_{,max} = PE_{max}$.

R_p may be found by resolving the equation:

$$PM_{\max} = V * I = PE_{\max} \tag{I.11}$$

$$R_p = \frac{V_{mp} + I_{mp} R_s}{Iph - I_0 \left[\exp\left(\frac{V_{mp} + I_{mp} R_s}{aV_T} \right) \right] - PE_{\max} / V_{mp}} \tag{I.12}$$

b) Vertical optimization methods

Unlike the iterative methods witch use only the tree remarkable points provided by the manufacturer (Short-circuit, Open-Circuit, Maximum power). The vertical optimization methods have the advantage of using all I-V points experimentally measured or given by the manufacturer, based on the minimization of the vertical quadratic error (the cost function) S on the vertical axis which is the current with respect to the set of parameters p [16]:

$$S(p) = \sum_{i=1}^{N} \left[I_{\exp,i} - I_{\mathrm{mod},i}(V_i, p) \right]^2 \tag{I.13}$$

Where p is the set of unknown parameters $(I_{ph}, I_o, a, R_s, R_p)$, N is the number of I-V measured points, $I_{mod,i}$and $I_{exp,i}$ are respectively theoretically and measured current for a given voltage V_i.So the model parameters extraction is converted to a nonlinear least squares problems. The Levenberg-Marquardt (LM) method is a standard technique for resolving such problem. The vector p is updated following the rule:

$$P_k = P_{k-1} - \left[H_{k-1} + \lambda_{k-1} \right]^{-1} \nabla J_{k-1} \tag{I.14}$$

where J is the Jacobean matrix and H is the Hessian matrix, λ is a scalar representing the adjustment step.

LM is one of faster and more accurate curve fitting algorithm, but like all Newton's method suffer from the great problem of initial values chose which is critical requirement for the convergence [17]. To overcome this critical problem and to proceed to the global solutions and overcome the local minima problem, Stochastic optimization techniques must be used.

The Genetic Algorithm (GA) is a method for solving both constrained and unconstrained optimization problems that are not well suited for standard optimization

algorithms, including problems in which the objective function is discontinuous, non - differentiable, or highly nonlinear [15]. GA is based on natural selection. Repeatedly a population of individual solutions may be modified. At each step, the genetic algorithm selects randomly individuals from the current population to be parents and uses them to produce the children for the next generation. Over successive generations, the population "evolves" toward an optimal solution. The initial population is composed of N chromosomes p which is the vector containing the five unknown parameters (I_{ph}, I_o, a, R_s, R_p). To create the next generation from the current one, GA applied three stochastic genetic operators:

- Selection rules Select parent chromosomes from a population according to their fitness
- Crossover rules with a crossover probability combine the parents to form a new offspring for the next generation.
- Mutation rules apply random changes to individual parents to form children.

Unlike LM algorithm, we haven't to provide an initial solution, simply we have to determine a search interval for the vector (I_{ph}, I_o, a, R_s, R_p).

For the iterative method as implemented by Villalva et al [15] , we chose arbitrary the diode ideality factor $a/Ns = 1.3$. R_s is slowly incremented by a step of 0.01 Ω. For the GA we use the Matlab optimization toolbox with prescribed terminologies. Table I.2 shows the model extracted parameters; the three methods are compared in term of mean squared error (MSE) defined as:

$$MSE = \frac{1}{N}\sum_{i=1}^{N}\left[I_{\exp,i} - I_{\mathrm{mod},i}(V_i, p)\right]^2 \qquad \text{(I.15)}$$

Table I.2: Extracted parameters of msx60 solar module.

Parameters	Iterative Method	GA	LM
$I_{ph}[A]$	3.8025	3.8263	3.8446
$I_s[\mu A]$	0.0928	0.5700	0.8089
a/Ns	1.3	1.4505	1.4858
$R_s[\Omega]$	0.1800	0.1737	0.1802
$R_p[\Omega]$	299.2488	819.2769	310.5626
MSE	$15\ 10^{-3}$	$2.63\ 10^{-4}$	$11\ 10^{-3}$

Fig. I.13 shows the I-V characteristic of the MSX60 module at the STC, the model curve based on the iterative method much exactly with the experimental value at the three remarkable points (P_1, P_2, P_3), however it has the worst MSE and this method is very sensible to the series resistance increment. In similarly to LM algorithm where the method

convergence depends critically on the initial values choose the GA based method has by far the best MSE with a guaranteed convergence to the global optimal values.

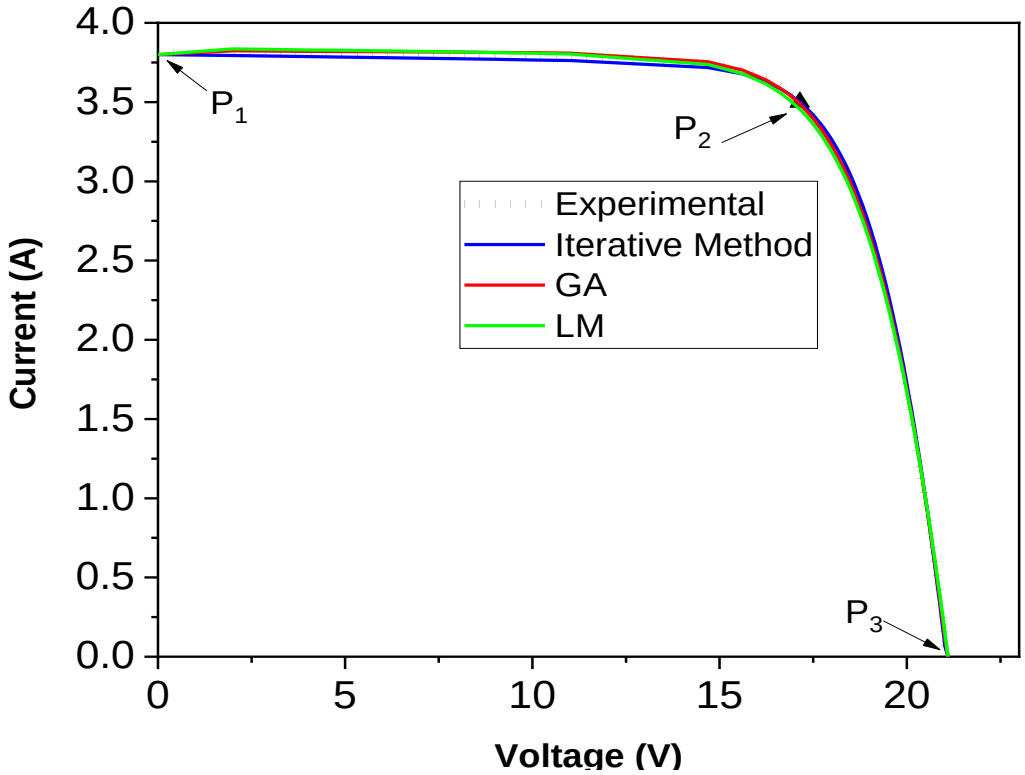

Fig. I.13: I-V curves for MSX60 solar module, at 25°C, AM1.5 and 1 kw/m^2.

I.6 Different generations of solar cells

Solar cells have undergone substantial advancements over the past forty years, resulting in significant improvements in their power conversion efficiency. Generally, solar cells can be categorized into three types:

I.6.1 First-generation of photovoltaic solar cell: crystalline silicon cells

The initial generation of solar cells is manufactured using silicon wafers. This technology, known as first-generation solar cells, is the oldest and most widely used due to its relatively high-power conversion efficiencies, typically ranging from 15% to 26%. Compared to non-silicon-based solar cells, this technology offers better efficiency and longer lifespan. However, it is more susceptible to efficiency loss at higher temperatures.

W. Shockley and H. Queissier were established that the maximum theoretical power conversion efficiency (PCE) of a single junction solar cell is approximately 33% [19]. Most solar cells utilizing polycrystalline silicon achieve PCEs around 15% to 26% [20,21]. Mono-crystalline silicon solar cells, on the other hand, have fewer defects in the silicon lattice and

typically exhibit higher PCEs, with the highest recorded efficiency reaching 26.8% [22], but their production and manufacturing costs are relatively expensive. Within the silicon wafer-based technology, there are two subcategories [23-26]:

- Single/Mono-crystalline silicon solar cells;
- Poly/Multi-crystalline silicon solar cells.

I.6.2 Second-generation of solar cells: thin-films solar cell

This cell generation class is also known as thin film solar cells because of using only few micrometer thicknesses of different layer materials in comparison of crystalline silicon-based cells. In the past decade, there has been an immense amount of research conducted on the production of more cost effective thin-film solar cells [27].

In this generation, use of silicon wafers is avoided while low-cost material like amorphous silicon, Cadmium Telluride CdS/CdTe, and Cu(In,Ga)Se_2 are used. They are produced by methods such as sputtering, plasma-enhanced chemical vapor deposition and physical vapor deposition. The highest record of PCE for thin-film technology solar cells are 21.1% – 23.3%, certified by National Renewable Energy Laboratory USA. Although their efficiencies due to less crystallized structure and presence of impurities remain lower than those of the first-generation, this type of cells prompted the development of light weight and flexible panels at relatively lower cost.

I.6.3 Third-generation of solar cell

Third-generation solar cells refer to a class of emerging photovoltaic technologies that aim to overcome the limitations of traditional first- and second-generation solar cells. These third-generation cells utilize alternative materials and novel device architectures to achieve higher efficiency, lower cost, and improved functionality. Third-generation solar cell technologies include organic photovoltaic cells with a power-conversion efficiency (PCE) record of 19.31% [28]. Dye-sensitized solar cells (DSSCs) with PCE reaches up to 12% [29]. Quantum dot solar cells: quantum dot solar cells employ nanoscale semiconductor crystals called quantum dots as the light-absorbing layer, but the most promising are:

- Perovskite solar cells: Perovskite solar cells utilize typically hybrid organic-inorganic lead halide compounds, as a light-absorbing layer. They have gained significant attention for their rapid efficiency improvement achieving recently 25.3% efficiency [30].

- Tandem and multi-junction cells: tandem and multi-junction solar cells combine multiple layers with different bandgaps to capture a wider range of the solar spectrum. By utilizing complementary absorber materials, these cells can achieve higher efficiency levels. Recently scientists led by Saudi Arabia's KAUST have achieved a power conversion efficiency of 33.7% for a perovskite-silicon tandem solar cell [31].

I.7 Thin-film solar cell structure

The key component of a solar cell is the P-N junction, which is formed by connecting a p-type semiconductor (absorber) with an n-type semiconductor (buffer) using various techniques. To optimize the functioning and achieve high efficiency, additional layers may be incorporated. These layers can include a Transparent Conductive Oxide (TCO) layer, as well as an anti-reflective coating (ARC). Fig. I.14 illustrates a typical solar cell structure, showcasing these essential elements. We can note the presence of several thin layers within the structure, which typically play a significant role in determining its overall performance. Below, we present the characteristics and functions of each layer:

I.7.1 Window layer

A Transparent Conducting Oxide (TCO), referred as a window layer, is a thin film material known for two significant attributes: Transparency (≥ 80%) and electrical conductivity (103 s.cm-1) [32]. Placed on top of the structure within a solar cell, the TCO layer serves as the front contact. Its main purpose is to enable the passage of visible sunlight, minimizing absorption or reflection, and allowing it to reach the underlying semiconductor layers. Additionally, it provides a conductive pathway for the generated electric current to exit the cell.

By incorporating a TCO layer, such as indium tin oxide (ITO), fluorine-doped tin oxide (FTO), ZnO:Al [33], or graphene [34], onto the solar cells, several benefits can be achieved:

- Conductive front contact: The TCO layer provides a conductive pathway for the generated electric current, allowing it to be extracted and utilized in external circuits.

- Electrical isolation: The TCO layer acts as a barrier, electrically isolating the front contact from the underlying semiconductor layers to prevent electrical shorts.
- Anti-reflective properties: In addition to its conductivity, the TCO layer can be engineered with anti-reflective properties to further minimize light reflection and maximize light absorption.

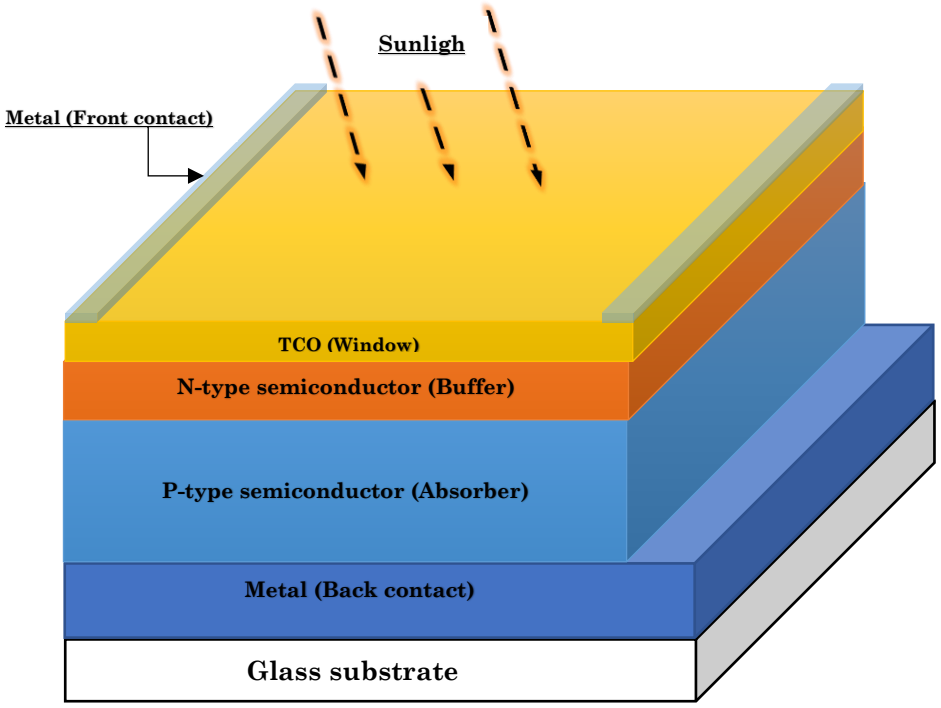

Fig. I.14: Schematic representation of a typical solar cell structure.

I.7.2 Buffer layer

The buffer layer, positioned between the absorber (p-type semiconductor) and the transparent conducting oxide (TCO), serves the purpose of establishing the P-N junction. In the buffer layer, a wider band-gap layer is typically employed to facilitate maximum light transmission, minimize absorption losses, and reduce recombination losses. Moreover, it facilitates the efficient transfer of photo-generated carriers to the external circuit and maintains an optimal thickness to minimize series resistance. By optimizing the parameters of the buffer layer, significant improvements can be achieved in the open-circuit voltage (V_{oc}) of solar cells [35]. The buffer layer performs several crucial functions, including:

- Interface optimization: The buffer layer helps to optimize the interface between the absorber and the TCO layer. It acts as a transition layer, ensuring better compatibility

between the different materials and minimizing interface defects or energy barriers that could impede the flow of charge carriers.

- Band alignment: The buffer layer can also help align the energy bands between the absorber and the TCO layer. It assists in achieving a favorable band alignment, which promotes efficient charge carrier collection and reduces losses due to carrier recombination at the interfaces.
- Carrier transport: The buffer layer facilitates the transport of charge carriers, both electrons and holes, from the absorber to the TCO layer. It provides a pathway for the charge carriers to move through and reach the front contact, improving the overall conductivity and current collection efficiency of the solar cell.
- Surface passivation: In certain cases, the buffer layer may serve as a surface passivation layer. It helps to reduce surface recombination by minimizing defects or trap states at the absorber surface.

The selection of materials for the buffer layer relies on the specific requirements of the solar cell structure and the type of absorber material employed. Typically, cadmium sulfide (CdS) [36,37] is a commonly used buffer layer material. However, CdS possesses a relatively narrow bandgap (E_g = 2.4 eV), which typically results in parasitic absorption of the incoming light that does not contribute to the photocurrent. CdS is not a perfect buffer layer material, also Cadmium and its compounds are known to be carcinogenic. Initially, Cadmium-free options such as ZnS and $In(OH)_3$ [38] were investigated. Another approach involves utilizing a $ZnO_{1-x}S_x$ buffer layer in conjunction with an ALD-grown $Zn_{1-x}Mg_xO$ as the second buffer layer [39]. Furthermore, Molybdenum disulfide (MoS_2) [40] has also been considered as a potential buffer layer material.

I.7.3 Absorber layer

The absorber layer holds great importance within the solar cell as it serves a critical function of capturing photons from sunlight and converting them into electron-hole pairs. It is typically constructed using a p-type semiconductor material that possesses a band-gap energy aligned with the photon-rich region of the solar spectrum. Common materials used include silicon (Si), amorphous silicon (a-Si), gallium arsenide (GaAs), cadmium telluride (CdTe), indium phosphide (InP), copper indium gallium selenide (CIGS) and copper zinc tin sulfide (CZTS) [41].

The thickness of the absorber layer is carefully selected to optimize the absorption of light while minimizing losses caused by recombination. Typically, it is selected within the range of the charge carrier diffusion length (DL) to facilitate effective collection and extraction of the generated current.

Among the mentioned materials, CZTS and/or CZTSe absorber layers offer several advantages:

- They provide a more sustainable and environmentally friendly alternative compared to CIGS, CdTe and CIS.
- CZTS and CZTSe have direct energy bandgaps ranging from 1.0 eV to 1.52 eV and from 0.9 eV to 1.12 eV, respectively, making them well-suited for efficient absorption of solar radiation.
- These materials exhibit high optical absorption coefficients above 10^4 cm^{-1}, indicating their ability to effectively capture photons and convert them into electrical energy [42].
- The charge carrier diffusion lengths for CIGSSe and CZTSSe are in the range of 2 -3.6 µm and 0.73 - 1 µm, respectively [43]. This allows for a thinner absorber layer, typically around 1 - 4 µm, reducing material usage while maintaining high performance.

The choice of absorber material depends on various factors: including cost, efficiency, stability, and compatibility with other layers in the solar cell structure.

I.7.4 Front and Back contacts

The back contact in the solar cell plays a critical role in collecting and effectively conducting the generated electrical current from the absorber layer to the external circuit. Commonly used materials for the back contact include metals like aluminum (Al), silver (Ag), molybdenum (Mo), and indium tin oxide (ITO). The choice of the back contact material depends on the specific absorber used in the solar cell.

To establish an efficient charge carrier transport, the back contact must form an ohmic contact with the absorber layer, ensuring a low resistance interface. The work function (W_b) of the back contact material plays a significant role in determining the Schottky barrier height between the rear contact and the absorber layer. Increasing the work function can decrease the Schottky barrier height, enabling better hole carrier collection at the back contact [44].

However, molybdenum (Mo), which is commonly used as a back contact material in CIGS and CdTe thin film solar cells, is not suitable for CZTS absorbers. This is because:

- CZTS has a bandgap of 1.54 eV and an electron affinity of 4.5 eV. Mo has a low work function value, leading to the formation of a Schottky barrier on the p-type CZTS/Mo interface [45].
- During thermal processing, the CZTS absorber layer may decompose into Cu_2S, ZnS, and SnS, while MoS_2 can grow, further hindering its suitability.

For CZTS absorber layers, a metal with a higher work function, such as nickel (W_{Ni} = 5.15 eV), is required to establish an ohmic contact with CZTS absorber layer [46].

I.8 Solar cell configuration using CZTS absorber layer

CZTS (Copper Zinc Tin Sulfide) absorber-based solar cells are thin-film solar cells that utilize CZTS as the semiconductor material in the absorber layer. These solar cells have gained attention as a promising alternative to traditional photovoltaic technologies due to:

- The constituent elements of CZTS are abundant in the earth's crust, making CZTS a sustainable and environmentally friendly choice.
- CZTS has a band-gap range of 1.4 to 1.7 eV, which aligns well with the solar spectrum, allowing for efficient absorption and conversion of sunlight into electricity.
- CZTS solar cells are typically fabricated as thin films using deposition techniques like sputtering, chemical vapor deposition (CVD) and/or electrodeposition techniques. The thin-film structure enables lightweight and flexible solar cell designs, making them suitable for curved surfaces and portable devices.

However, the current research results show that conversion efficiency (η) of CZTS solar cells has a great amelioration from 0.66% for the first CZTS solar cell (vacuum deposited) reported in 1997 [47] to 14.9% [48], which is below the enhancement in the theoretical value of 29.86% for FTO/ZnO/CdS/CZTS/CZTSe/Pt [49]. The primary reason for the poor efficiency is lower open circuit voltage (V_{oc}) due to the back contact, TCO material choice or band alignment. Many optimization are made in device structure and used materials.

I.8.1 Substrate configuration of CZTS thin-film solar cell

Similar to CIGS thin-film solar cells (CIGS TFSC), a conventional CZTS TFSC follows the substrate structure configuration. In this structure, the solar cell device as indicated in Fig.I.15(a), it consists of:

- Back contact metal (Mo, Ni and ITO) coated glass substrate with thickness of 800 nm.
- CZTS layer with a thickness ranging from 1 µm to 5 µm, acts as the light absorber in the solar cell [46,50,51].
- Buffer layer of 0.1 µm to 0.2 µm n-type semiconductor material (CdS, ZnS and ZnO) placed on top of the CZTS absorber layer to form a P-N junction [46, 50,51].
- A thin layer of transparent conductive oxide (TCO), often ZnO:Al, deposited on top of the buffer layer.
- Electrical contact: An electrical contact layer typically made of aluminum (Al) and nickel (Ni).

I.8.2 Superstrate configuration of CZTS thin-film solar cell

As mentioned in previous paragraph, CZTS and Mo interface is chemically unstable during thermal processing. To overcome these drawbacks, superstrate configuration is proposed as a solution to this problem. As shown in Fig I.15(b) the back contact in this architecture consists of transparent conductive oxide electrode (FTO or ITO). This electrode serves as the foundation for depositing all other layers involved in electron transport, such as photoactive CZTS layer [52]. Simultaneously, the transparent nature of the transparent conductive oxide and the glass enables the passage of light.

A good comparison of superstrate and substrate configuration and deposition of CZTS/CdS using SILAR method made by Kaza Jasmitha et *al.* [53], demonstrate an amelioration in the superstrate cell efficiency, due to the augmentation of the open-circuit voltage (2.45% and 0.73 V for FTO/CdS/CZTS structure and 1.02%, 0.41 V for Mo/CZTS/CdS structure.

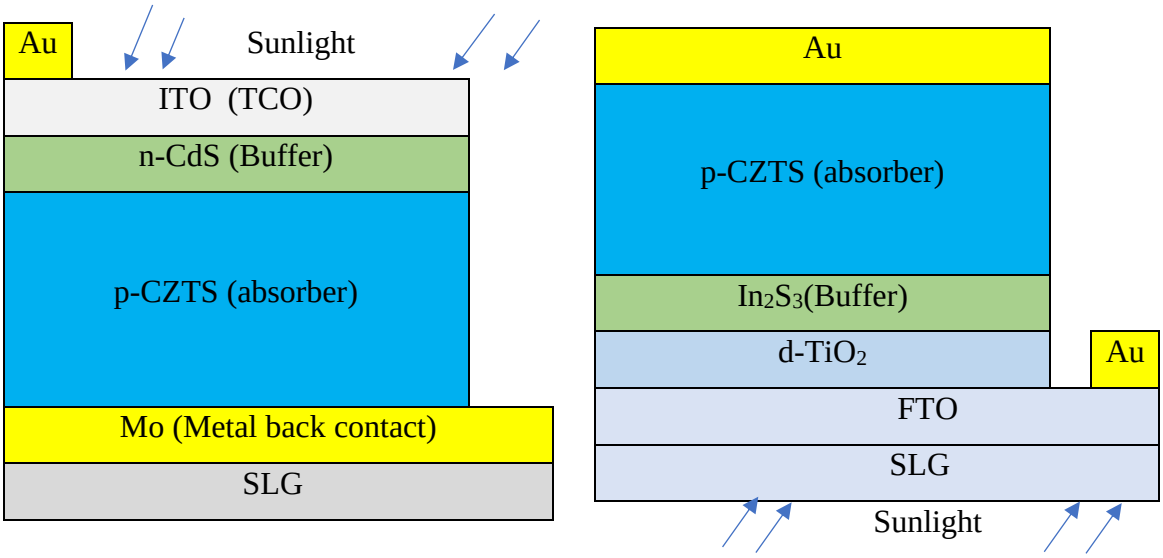

(a) (b)

Fig. I.15: (a) Substrate configuration [54] and (b) Superstrate configuration [55] of CZTS solar cell.

I.8.3 Bifacial configuration of CZTS solar cell

Bifacial configuration of CZTS solar cell, as shown in Fig. I.16, are designs that enable the sunlight to pass from both sides of the cell. This configuration take advantage of the albedo effect, which refers to the reflection of sunlight by surrounding surfaces in the solar installation area. Bifacial flexible CZTSSe solar cell proposed by Hui Deng [56], with a double-sided symmetrical structure: Ag/ITO/ZnO/CdS/CZTSSe/$MoSe_2$/Mofoil/$MoSe_2$/CZTSSe/CdS/ZnO/ITO/Ag, this structure achieve an efficiency of 9.3% for the front side and 9% for the backside [57].

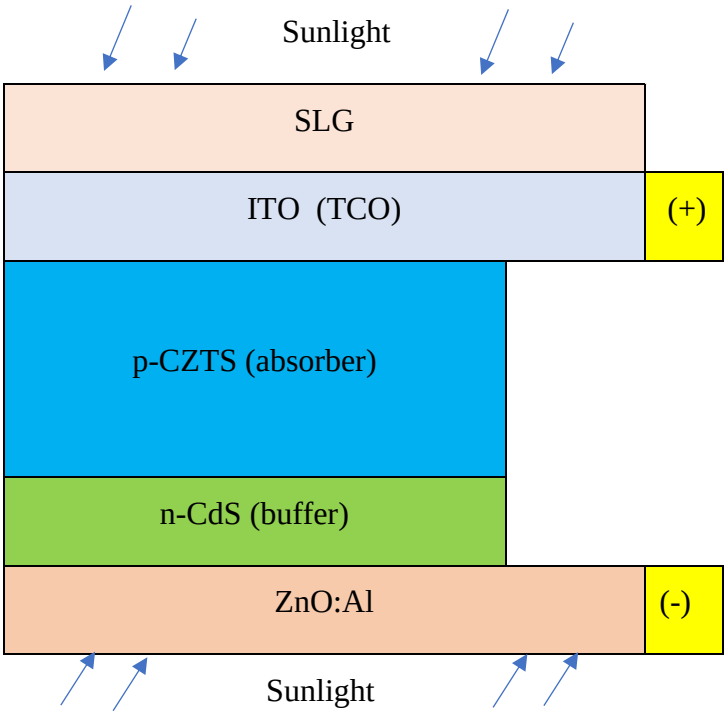

Fig. I.16: Bifacial configuration of CZTS solar cell [44].

I.8.4 Tandem CZTS solar cell

The aim of tandem CZTS thin-film solar cells also known as multi-junction solar cells is to enhance the efficiency of CZTS-based photovoltaic devices by combining multiple absorber layers with different band-gaps. Various multi-junctions cell configurations have been proposed. Fig. I.17 represent a CZTS/Si tandem device demonstrated experimentally by Alireza Hajijafarassar et al. [57]. The CZTS layer is designed to absorb higher-energy photons, while the Si layer absorbs lower-energy photons, maximizing the utilization of the solar spectrum.

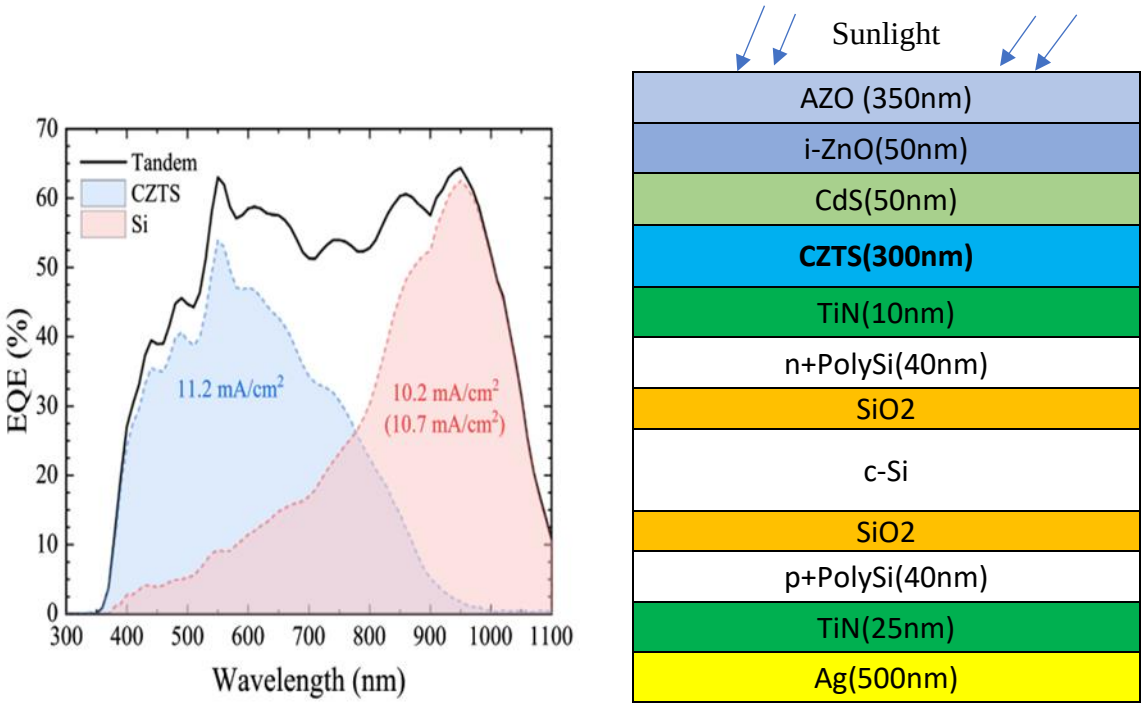

(a) (b)

Fig. I.17: (a) EQE of both CZTS and c-Si sub-cells and that of Tandem CZTS/c-Si contribution and (b) Alireza Hajijafarassar et *al.* Tandem solar cell scheme.[57]

I.9 Conclusion

This chapter provided an overview of the principal functioning of photovoltaic solar cells, starting from sunlight and progressing to the modeling of solar cell panels. The P-N junction, was discussed in detail, followed by an exploration of numerical methods for solar cell modeling and techniques for parameter extraction. The chapter concluded with a focus on the structure of CZTS solar cells and the various configuration options available.

In the following chapter, we will discuss the structural, electrical, and optical properties of transparent and conductive oxides (TCO), which are commonly used in thin-film solar cells based on CZTS absorbers. A simulation study using Silvaco and AMPS-1D softwares was presented for multiple configurations.

References

[1] International Energy Agency (IEA). (2022). Energy Efficiency 2022. www.iea.org.

[2] Taseska, T., Yu, W., Wilsey, M. K., Cox, C. P., Meng, Z., Ngarnim, S. S., & Müller, A. M. (2023). Analysis of the Scale of Global Human Needs and Opportunities for Sustainable Catalytic Technologies. Topics in Catalysis. doi:10.1007/s11244-023-01799-3

[3] International Energy Agency (IEA). (2022). Renewables 2022. www.iea.org.

[4] Fatet, J. (2005). Les recherches d'Edmond Becquerel sur la nature de la lumière entre 1839 et 1843 Histoire d'une interaction réussie entre science et photographie. Claude Bernard university Lyon 1, France.

[5] Chapin, D. M., Fuller, C. S., & Pearson, G. L. (1954). A new silicon p-n junction photocell for converting solar radiation into electrical power. Journal of Applied Physics, Vol. 25, Issue 5, pp. 676–677. doi:10.1063/1.1721711.

[6] Lincot, D. (2017). The new paradigm of photovoltaics: From powering satellites to powering humanity. Comptes Rendus Physique, Vol. 18, Issues 7–8, pp. 381–390. doi:10.1016/j.crhy.2017.09.003.

[7] https://www.nrel.gov/pv/cell-efficiency.html, National Renewable Energy Laboratory (NREL), Consulted on June 18, 2023.

[8] Mertens, K., Photovoltaics: Fundamentals, Technology and Practice, John Wiley & Sons, Chichester, UK, 2014, p. 24.

[9] Wenham, S. R. (2007). Applied photovoltaics. Earthscan. ISBN 978-1-84407-401-3.

[10] UMESH, K. M., JASPRIT, S. (2008). Semiconductor device physics and design. Netherlands, Springer.

[11] Messei, N. (2016). Study of the effect of grading in composition on the performance of thin film solar cells based on AlGaAs and CZTSSe, a numerical simulation approach. Doctorate thesis, university frères Mentouri Constantine1, Algeria.

[12] Yahfdhou, A., Menou, M. M., Yahya, A. M., Eida, Ne. D., Mahmoud, A. K., & Youm, I. (2016). Valuation and Determination of Seven and Five Parameters of Photovoltaic Generator by Iterative Method. Smart Grid and Renewable Energy, Vol. 07(09), pp.247–260. doi:10.4236/sgre.2016.79019.

[13] Ortiz-Conde, A., García Sánchez, F. J., & Muci, J. (2006). New method to extract the model parameters of solar cells from the explicit analytic solutions of their illuminated I-V characteristics. Solar Energy Materials and Solar Cells, Vol. 90(3), pp. 352–361. doi:10.1016/j.solmat.2005.04.023

[14] http://www.solarelectricsupply.com/media/sparsh/product_attachment/custom/upload/Solarex-MSX64.pdf, Consulted on June 18, 2023.

[15] Villalva, M. G. et al. "Comprehensive Approach to Modeling and Simulation of Photovoltaic Arrays." IEEE Transactions on Power Electronics, vol. 24, no. 5, 2009, pp. 1198-208, doi:10.1109/tpel.2009.2013862.

[16] Toumi, S. and Z. Ouennoughi. "A Vertical Optimization Method for a Simultaneous Extraction of the Five Parameters Characterizing the Barrier Height in the Mo/4h–Sic Schottky Contact." Indian Journal of Physics, vol. 93, no. 9, 2019, pp. 1155-62, doi:10.1007/s12648-019-01393-y.

[17] Wilamowski, B. M., & Yu, H. (2010). Improved computation for Levenberg Marquardt training. IEEE Transactions on Neural Networks, Vol. 21(6), pp. 930–937. doi:10.1109/TNN.2010.2045657.

[18] Ismail, M. S., Moghavvemi, M., & Mahlia, T. M. I. (2013). Characterization of PV panel and global optimization of its model parameters using genetic algorithm. Energy Conversion and Management, Vol. 73, pp. 10–25. doi:10.1016/j.enconman.2013.03.033.

[19] Shockley, W., & Queisser, H. J. (1961). Detailed balance limit of efficiency of p-n junction solar cells. Journal of Applied Physics, Vol. 32(3), pp. 510–519. doi:10.1063/1.1736034.

[20] Jay, F., Muñoz, D., Desrues, T., Pihan, E., Amaral De Oliveira, V., Enjalbert, N., & Jouini, A. (2014). Advanced process for n-type mono-like silicon a-Si:H/c-Si heterojunction solar cells with 21.5% efficiency. Solar Energy Materials and Solar Cells, Vol. 130, pp. 690–695. doi: 10.1016/j.solmat.2014.02.02.

[21] Park, K. M., Lee, M. B., & Choi, S. Y. (2015). Investigation of surface features for 17.2% efficiency multi-crystalline silicon solar cells. Solar Energy Materials and Solar Cells, Vol. 132, pp. 356–362. doi: 10.1016/j.solmat.2014.07.023.

[22] Green, Martin A. et al. "Solar Cell Efficiency Tables (Version 63)." Progress in Photovoltaics: Research and Applications, vol. 32, no. 1, 2023, pp. 3-13, doi:10.1002/pip.3750.

[23] Chopra, K. L., Paulson, P. D., & Dutta, V. (2004). Thin-film solar cells: An overview. Progress in Photovoltaics: Research and Applications, *Vol.* 12(2–3), pp. 69–92. doi:10.1002/pip.541.

[24] Fahrenbruch, A.L. and Bube, R.H. (1983). Fundamentals of Solar Cells. Academic Press Inc., New York.

[25] Mohammad Bagher, A. (2015). Types of solar cells and application. American Journal of Optics and Photonics, Vol. 3(5), pp. 94. doi: 10.11648/j.ajop.20150305.17.

[26] Sharma S, Jain KK, Sharma A. (2015). Solar Cells: In Research and Applications—A Review. Materials Sciences and Applications. vol. 06(12), 2015, pp. 1145–1155, doi:10.4236/msa.2015.612113.

[27] Komilian, S. (2019). Investigation into Device Optimization of Organic Solar Cells Using Narrow Bandgap Polymer and the Role of Acceptor Material. Doctorate thesis, Staffordshire University, England.

[28] Fu, J., Fong, P. W. K., Liu, H., Huang, C. S., Lu, X., Lu, S., Abdelsamie, M., Kodalle, T., Sutter-Fella, C. M., Yang, Y., & Li, G. (2023). 19.31% binary organic solar cell and low non-radiative recombination enabled by non-monotonic intermediate state transition. Nature Communications, Vol. 14(1), pp. 1760. doi:10.1038/s41467-023-37526-5.

[29] Sharma, K., Sharma, V., & Sharma, S. S. (2018). Dye-Sensitized Solar Cells: Fundamentals and Current Status. Nanoscale Research Letters 13. Article number: 381. Springer New York LLC. doi:10.1186/s11671-018-2760-6.

[30] Yang, T., Gao, L., Lu, J., Ma, C., Du, Y., Wang, P., Ding, Z., Wang, S., Xu, P., Liu, D., Li, H., Chang, X., Fang, J., Tian, W., Yang, Y., Liu, S., & Zhao, K. (2023). One-stone-for-two-birds strategy to attain beyond 25% perovskite solar cells. Nature Communications, Vol. 14, Article number 839. doi:10.1038/s41467-023-36229-1.

[31] https://www.pv-magazine-india.com, Consulted on June 20, 2023.

[32] Stadler, A. (2012). Transparent conducting oxides - An up-to-date overview. Materials, Vol. 5(12), pp. 661–683. doi:10.3390/ma5040661.

[33] Kawashima, T., Ezure, T., Okada, K., Matsui, H., Goto, K., & Tanabe, N. (2004). FTO/ITO double-layered transparent conductive oxide for dye-sensitized solar cells. Journal of Photochemistry and Photobiology A: Chemistry, Vol. 164(1–3), pp. 199–202. doi:10.1016/j.jphotochem.2003.12.028.

[34] Patel, K., & Tyagi, P. K. (2015). Multilayer graphene as a transparent conducting electrode in silicon heterojunction solar cells. AIP Advances, Vol. 5(7), pp. 077165-077165. doi:10.1063/1.4927545.

[35] Sozzi, G., Troni, F., & Menozzi, R. (2014). On the combined effects of window/buffer and buffer/absorber conduction-band offsets, buffer thickness and doping on thin-film solar cell performance. Solar Energy Materials and Solar Cells, Vol. 121, pp. 126-136. doi:10.1016/j.solmat.2013.10.037.

[36] Niki, S., Contreras, M., Repins, I., Powalla, M., Kushiya, K., Ishizuka, S., & Matsubara, K. (2010). CIGS absorbers and processes. Progress in Photovoltaics: Research and Applications, Vol. 18(6), pp. 453-466. doi:10.1002/pip.969.

[37] Katagiri, H., Jimbo, K., Maw, W. S., Oishi, K., Yamazaki, M., Araki, H., & Takeuchi, A. (2009). Development of CZTS-based thin film solar cells. Thin Solid Films, Vol. 517(7), pp. 2455-2460. doi:10.1016/j.tsf.2008.11.002.

[38] Hariskos, D., Spiering, S., & Powalla, M. (2005). Buffer layers in $Cu(In,Ga)Se_2$ solar cells and modules. Thin Solid Films, Vol. 480–481, pp. 99-109. doi:10.1016/j.tsf.2004.11.118.

[39] Nakamura, M., Yamaguchi, K., Kimoto, Y., Yasaki, Y., Kato, T., & Sugimoto, H. (2019). Cd-Free $Cu(In,Ga)(Se,S)_2$ thin-film solar cell with record efficiency of 23.35%. IEEE Journal of Photovoltaics, Vol. 9(6), pp. 1863-1867. doi:10.1109/JPHOTOV.2019.2937218.

[40] Musztyfaga-Staszuk, M., Czupryński, A., & Radev, R. (2022). Review of the Chosen Methods of Producing Front Contacts to Transparent Conductive Oxides Layers in Photovoltaic Structures. Energies, Vol. 15(23), pp. 9026-9026, MDPI. doi:10.3390/en15239026.

[41] Miles, R. W. (2006). Photovoltaic solar cells: Choice of materials and production methods. Vacuum, Vol. 80(10), pp. 1090–1097. doi:10.1016/j.vacuum.2006.01.006.

[42] Rondiya, S, Avinash, R. Sharma, P. et al. (2017). CZTS/CdS: interface properties and band alignment study towards photovoltaic applications. Journal of Materials Science: Materials in Electronics, vol. 29(5), pp. 4201–4210. doi:10.1007/s10854-017-8365-5.

[43] Gokmen, T., Gunawan, O., Mitzi, D. B. (2013). Minority carrier diffusion length extraction in $Cu_2ZnSn(Se,S)_4$ solar cells. Journal of Applied Physics, Vol. 114(11), pp. 114511-114511, doi:10.1063/1.4821841.

[44] Bouchama, I., Ali-Saoucha, S. (2017). Effect of wide band-gap TCO properties on the bifacial CZTS thin-films solar cells performances. Optik, Vol. 144, pp. 370–377. doi:10.1016/j.ijleo.2017.07.009.

[45] Scragg, J. J., Wätjen, J. T., Edoff, M., Ericson, T., Kubart, T., & Platzer-Björkman, C. (2012). A detrimental reaction at the molybdenum back contact in $Cu_2ZnSn(S,Se)_4$

thin-film solar cells. Journal of the American Chemical Society, Vol. 134(47), pp. 19330-19333. doi:10.1021/ja308862n.

[46] Kumar, A., Singh, N. P., & Sundaramoorthy, A. (2021). Comparative device performance of CZTS solar cell with alternative back contact. Materials Letters, Vol. 12. pp. 100092-100092. doi:10.1016/j.mlblux.2021.100092.

[47] Katagiri, H., Sasaguchi, N., Hando, S., Hoshino, S., Ohashi, J., & Yokota, T. (1997). Preparation films by and evaluation of Cu_2ZnSnS_4 thin sulfurization of E-B evaporated precursors. Solar Energy Materials and Solar Cells, Vol. 49(1-4), pp. 407-414 doi:10.1016/S0927-0248(97)00119-0.

[48] Green, Martin A. et al. "Solar Cell Efficiency Tables (Version 63)." Progress in Photovoltaics: Research and Applications, vol. 32, no. 1, 2023, pp. 3-13, doi:10.1002/pip.3750.

[49] Rana, M. S., Islam, M. M., & Julkarnain, M. (2021). Enhancement in efficiency of CZTS solar cell by using CZTSe BSF layer. Solar Energy, Vol. 226, pp. 272–287. doi:10.1016/j.solener.2021.08.035.

[50] Sadanand, & Dwivedi, D. K. (2020). Numerical Simulation for Enhancement of the Output Performance of CZTS Based Thin Film Photovoltaic Cell. Advanced Science, Engineering and Medicine, Vol. 12(1), pp. 88–94. doi:10.1166/asem.2020.2526.

[51] Tripathi, S., Sadanand, Lohia, P., & Dwivedi, D. K. (2020). Contribution to sustainable and environmental friendly non-toxic CZTS solar cell with an innovative hybrid buffer layer. Solar Energy, Vol. 204, pp. 748–760. doi:10.1016/j.solener.2020.05.033.

[52] Wang, Z., Brodusch, N., Gauvin, R., & Demopoulos, G. P. (2018). Lithium-doped Cu_2ZnSnS_4 superstrate solar cells with 5% efficiency – An alternative to thin film kesterite photovoltaics. Nano Energy, Vol. 53, pp. 130–134. doi:10.1016/j.nanoen.2018.08.049.

[53] Kaza, J., Pasumarthi, M. R., & Avadhani, P. S. (2020). Superstrate and substrate thin film configuration of CdS/CZTS solar cell fabricated using SILAR method. Optics and Laser Technology, Vol. 131. pp. 106413-16413. doi:10.1016/j.optlastec.2020.106413.

[54] Prima, E. C., Wong, L. H., Ibrahim, A., Nugraha, & Yuliarto, B. (2021). Solution-processed pure Cu_2ZnSnS_4/CdS thin film solar cell with 7.5% efficiency. Optical Materials, Vol. 114. doi:10.1016/j.optmat.2021.110947.

[55] Lee, D., & Yang, J. Y. (2020). Superstrate structured FTO/TiO_2/In_2S_3/Cu_2ZnSnS_4 solar cells fabricated by a spray method with aqueous solutions. Coatings, Vol. 10(6), pp. 548-548. doi:10.3390/COATINGS10060548.

[56] Deng, H. et al. "Novel Symmetrical Bifacial Flexible CZTSSe Thin Film Solar Cells for Indoor Photovoltaic Applications." Nat Commun, vol. 12, no. 1, 2021, p. 3107, doi:10.1038/s41467-021-23343-1.

[57] Hajijafarassar, Alireza et al. "Monolithic Thin-Film Chalcogenide–Silicon Tandem Solar Cells Enabled by a Diffusion Barrier." Solar Energy Materials and Solar Cells, vol. 207, 2020. doi:10.1016/j.solmat.2019.110334.

Chapter II: Performances optimization of CZTS thin film solar cells

Chapter II

Performances optimization of CZTS thin film solar cells

II.1 Introduction

Due to its potential to replace costly and scarce elements like In and Ga with more abundant and cost-effective Zn and Sn in $Cu(In,Ga)Se_2$ (CIGSe) absorber layers [1]. Unlike the materials traditionally used in thin-film solar cells, such as In, Ga, Se, Cd, and Te, which are rare and expensive [2], Cu_2ZnSnS_4 (CZTS) material is being actively explored as a new material for solar devices. CZTS exhibits a direct band gap within the optimal range for efficient solar absorption (1.4 - 1.5 eV), similar to CIGS, and boasts a high absorption coefficient ranging from 10^4 - 10^5 cm^{-1} [3].

Despite the interesting optical properties, the highest achieved conversion efficiency with CZTS-based solar cells remains modest at 12.6% [4] compared to the 20.4% efficiency reached by CIGS [5]. The relatively low efficiency can be partially ascribed to challenges in synthesizing the absorber layer or suboptimal selection of the metal or transparent conducting oxide (TCO) back contact layers. CZTS solar cell devices commonly utilize molybdenum (Mo) as a back contact, restricting light transmission to the front side only. Conversely, a bifacial configuration, allowing light entry from both sides of the device, can be achieved by employing Transparent Conductive Oxide (TCO) materials as back contacts. This configuration has already been successfully demonstrated in CIGS thin-film solar cells [6]. Moreover, employing TCO substrates as back contacts opens up the opportunity to create semi-transparent thin-film solar cells and tandem solar cells. However, in contrast to CIGS thin-film solar cells, limited research has been conducted on substrate, bifacial and tandem structures utilizing CZTS absorbers using Transparent Conducting Oxides layers.

Numerous factors constrain the performance of bifacial CZTS solar cells, with one crucial aspect being the band alignment effect at the CZTS/TCO interface. The work function of the Transparent Conductive Oxide (TCO) films (WTCO) holds significant importance in the performance of optoelectronic devices, influencing both the energy barrier height at the heterojunction interface and electron field emission [7]. The alteration in work function and the barriers for electron/hole injection are associated with band alignment. Utilizing high work function values for Transparent Conductive Oxide (TCO) is advantageous for injecting holes into the back contact barrier, emphasizing the preference

for maximizing work functions. Ritzau *et al.* [8] investigated the impact of work function and back contact barrier height on the performance of a-Si:H solar cells. Abbes Belfar [9] conducted a simulation-based study on the influence of Transparent Conductive Oxide (TCO) work function (WTCO) using AMPS-1D simulation tools. The study focused on the performance of n–i–p+ and n–i–p–p+ solar cells with hydrogenated amorphous silicon (a-Si:H) and hydrogenated nanocrystalline silicon (nc-Si:H) absorber layers. However, there is currently no available research discussing the effect of WTCO and barrier height in bifacial CZTS solar cells.

In this Chapter, we will begin by examining various CZTS solar cell structures, aiming to determine the optimal thickness and carrier concentration in both CZTS absorber and CdS buffer layers. Following this analysis, we will investigate the feasibility of utilizing a Cd-free buffer material for CZTS solar cells. Our exploration will extend to evaluating the influence of the barrier height at the CZTS/TCO interface for bifacial CZTS solar cells, considering illumination from both the front and back sides. Lastly, we will delve into the application of Transparent Conductive Oxides (TCOs) in tandem CZTS/CZTSe solar cell configurations. This exploration is substantiated by a comprehensive simulation study utilizing Silvaco-Atlas and AMPS-1D software.

II.2 TCO layer utility in CZTS solar cell structure

Transparent conductive oxides (TCO) find diverse applications, serving as charge carrier layers in transparent transistors, solar cells, dye-sensitive solar cells, and organic solar cells. In the realm of solar cell applications, TCOs play a crucial role as a window layer, forming a PN junction with the absorber layer in conjunction with the buffer layer. Particularly in bifacial solar cells, TCOs are essential as the rear back contact. In tandem cells, TCOs function as an intermediate layer between the top and bottom cells.

The key criteria for an ideal window layer in thin film photovoltaic applications revolve around superior opto-electrical properties. Specifically, the semiconductor material should exhibit high transparency within the visible and near-infrared (NIR) wavelength range, aligning with the greater intensity of the solar spectrum. This desirable characteristic is achieved by ensuring the semiconductor's band gap is suitable ($E_g > 3$ eV). Additionally, a resistivity below $\rho \leq 10^{-3}$ **Ω**.cm is necessary to achieve a conductive yet relatively thin layer of Transparent Conductive Oxide (TCO) [10].

TCO layers typically take the form of compound semiconductors, represented as M_xO_y:D, where 'M' denotes the metal or combination of metals, 'O' signifies oxygen, and 'D' indicates potential dopants. These oxides are characterized as wide band gap (E_g) semiconductors, featuring conductivity within the range of 10^2 to 1.2×10^6 S. Conductivity is achieved through doping, either by introducing oxygen vacancies or incorporating extrinsic dopants. In the absence of doping, these oxides function as highly effective insulators. However, attaining both excellent electrical conductivity and high transparency simultaneously can be challenging.

The resistivity (ρ) of a semiconductor is influenced by both the charge carrier density (N) and carrier mobility (μ), and can be expressed through the following relationship:

$$1/\rho = N\mu e \tag{II.1}$$

Here, e represents the electronic charge ($1.60210^{-19} C$).

Optimal carrier concentrations typically fall within the range of 10^{20} cm^{-3} to $10^{21}cm^{-3}$. However, a high charge carrier density may result in undesirable free-carrier absorption or parasitic absorption [11]. Rather than increasing the carrier density (*N*), achieving high mobility Transparent Conductive Oxides (TCOs) is feasible by enhancing carrier mobility (μ), allowing for reduced doping concentrations and consequently lower resistivity ($\rho \approx 10^{-4}$ Ω.cm). This approach maintains excellent transmission in the near-infrared (NIR) range. The crystalline structure of TCO thin films can be improved through heat treatment, leading to enhanced mobility. Another critical characteristic of TCO materials is their thermal and chemical stability during the deposition process. For example, In_2O_3 is an intriguing TCO with a high mobility of 62.5 $cm^2V^{-1}s^{-1}$, NIR transparency, and low resistivity (10^{-4} Ω.cm) [12]. However, it has been observed that In_2O_3 faces challenges in crystallizing on CdS buffer layer [13].

Another crucial aspect of TCO layers is the presence of a transmission window that spans a significant portion of the visible spectrum, ranging from 400 nm to 700 nm. The optical properties, including the refractive index (n) and extinction coefficient (k), of TCOs are highly dependent on the deposition process. Consequently, for a given TCO material, no single set of (n) and (k) can accurately represent all films.

N-type Transparent Conductive Oxides (TCOs) play a crucial role in thin film solar cell production, with notable examples being indium-tin oxide (ITO) and the cost-effective aluminum-doped zinc oxide (ZnO:Al):

- **Indium Tin Oxides (ITO):** Sn-doped indium oxide (In_2O_3:Sn) stands out as the most widely used and developed material among transparent conductive oxides. Thin film ITO finds applications in transparent electrodes for displays, photovoltaic devices, sensors, and transparent electronics. High-quality ITO exhibits an internal transmittance of 80 - 85% and a resistivity within the range of 2×10^{-4} Ω.cm [14].
- **Doped Zinc Oxides (ZnO):** Although ITO is predominant, zinc oxide (ZnO) and related compositions have become competitive alternatives, particularly in light of the global depletion of indium. Aluminum-doped ZnO is increasingly employed as a transparent conductive contact in thin film solar cells. ZnO films typically doped with Al have a resistivity ranging around 1×10^{-4} Ω.cm [14] and an internal transmittance of 80 - 85% [15].

II.3 Simulation Tools

In this study, we utilized the one-dimensional device simulation software AMPS and two-dimensional Silvaco/Atlas TCAD. These programs are specifically engineered to calculate the steady-state band diagram, recombination profile, and carrier transport. This is accomplished by solving the Poisson equation, in conjunction with the hole and electron continuity equations, providing a comprehensive analysis of semiconductor device behavior.

II.3.1 Silvaco simulation environment

The utilization of Silvaco ATLAS simulation software to model a CZTS cell and assess its performance for different configurations and variations of cell parameters involves five main steps. The etch step is accomplished through a specified set of statements [16]:

1) Structure specification:

The initial step involves establishing a mesh on which the cell is constructed through the utilization of mesh statements.

Mesh space.mult = "value"

"space.mult" is a scaling factor that can changed at will, for simplicity its value is chosen in order to obtain a total surface area opposite to the light source of 1 cm².

x.mesh location= "value" spacing = "value"

"x.mesh" defines the horizontal mesh divisions in microns along with their corresponding spacing.

y.mesh location= "value" spacing = "value"

"x.mesh" defines the vertical mesh divisions in microns along with their corresponding spacing.

A fine defined mesh will lead to more accurate results, Fig. II.1 depict an example of well-defined mesh.

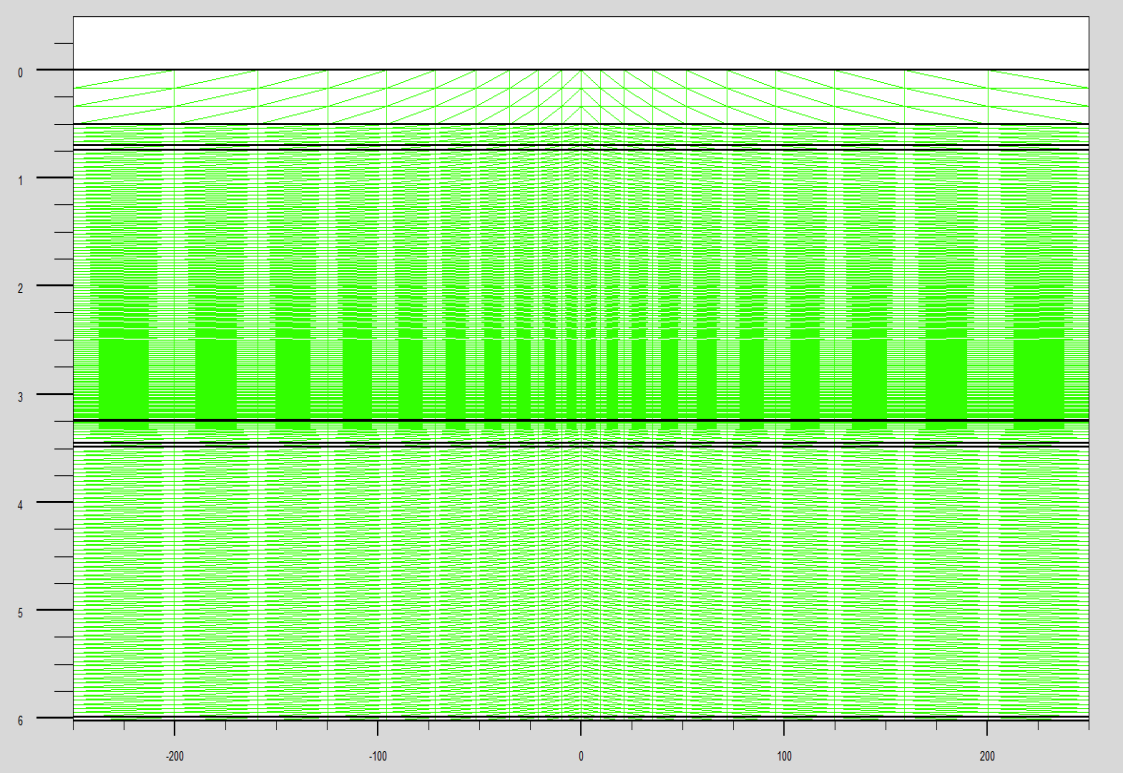

Fig. II.1: Example of well-defined mesh.

The mesh will be divided into numbered areas called regions, where each one is associated with a specific material with the following statements:

region number= "integer" "material type" "region_limits"

For solar cell simulation, we need at least to define a pair of cathode and anode electrodes using the following statements:

electrode name= "name" "position"

Anode and cathode positions can be specified by "bottom" and "top" statements. In multi-junction structures more electrodes are used, their positions must be determined by "x.min", "x.max", "y.min", "y.max" statements.

The type and concentration of doping in etch region can be specified using the

following statements:

doping "distribution type" "dopant type" "region= integer" conc= "value"

doping distributions can be uniform, Gaussian or user defined.

2) Material model specification

In this step the user has to define:

- The material for etch region including all electrical parameters (electrons and holes mobility and lifetimes, permittivity, affinity, bandgap …) and optical parameters (extinction coefficient, refractive coefficient) by the statements:

material "region=Integer" "material-definition"

These material properties and physical parameters are defined in the Atlas library, for our case CZTS, In_2S_3, CZTSe materials aren't included, so we have to define them manually as user materials.

- The physical models suitable for evaluating the structure (SRH, Auger, Commob…) by the statements:

models "model flag" "general and model dependent parameter"

- Light beam that illuminates the cell as in real conditions, simulating different regions of the solar spectrum, by the statements:

beam num= "integer" "origin position"

- The interface between semiconductors and insulators, their charge density and recombination velocity are defined by statement:

interface "position" "parameters"

3) Numerical method selection

The Atlas library provides three methods for solving the required differential equations, which determine the operating characteristics of the cell. The "Gummel" method iteratively solves for each unknown while keeping the other variables at their original values, continuing until a stable solution is achieved. The "Newton" technique resolves the entire system of unknowns collectively. The "Block" method combines both the Newton and Gummel methods.

4) Solution specification

The simulation characteristics can be stored in a log file through the "log" statement.

Subsequently, the "solve" statement is employed to obtain the solution for specified bias points. The "save" and "load" statements are utilized to save all information, including structures and parameters, acquired for a node to an output file and to load it later.

5) Result extraction and analysis

The concluding section of the input deck involves the extraction and visualization of data. The "Extract" statement, with its versatile syntax, enables users to manipulate the saved log file, extract specific device parameters, or construct a tailored solution data file. The "tonyplot" statement allows users to access an interactive graphics package for plotting and analyzing the log files.

II.3.2 AMPS-1D simulator

AMPS-1D is freely available one-dimensional Analysis of Microelectronic and Photonic Structures (AMPS-1D) program was developed in 1990's by professor Stephen J. Fonash and students at the Pennsylvania State University [17] in order to analyze and design the transport of charge carrier in microelectronic and photonic devices such solar cells. AMPS-1D solves the dipolar problems of device-based semiconductors according to the Poisson equation and the continuity equations for electrons and holes. While Silvaco-Atlas uses instructions script to build the solar cell structure, solve the equations and extract the results, AMPS-1D use a graphic simple interface.

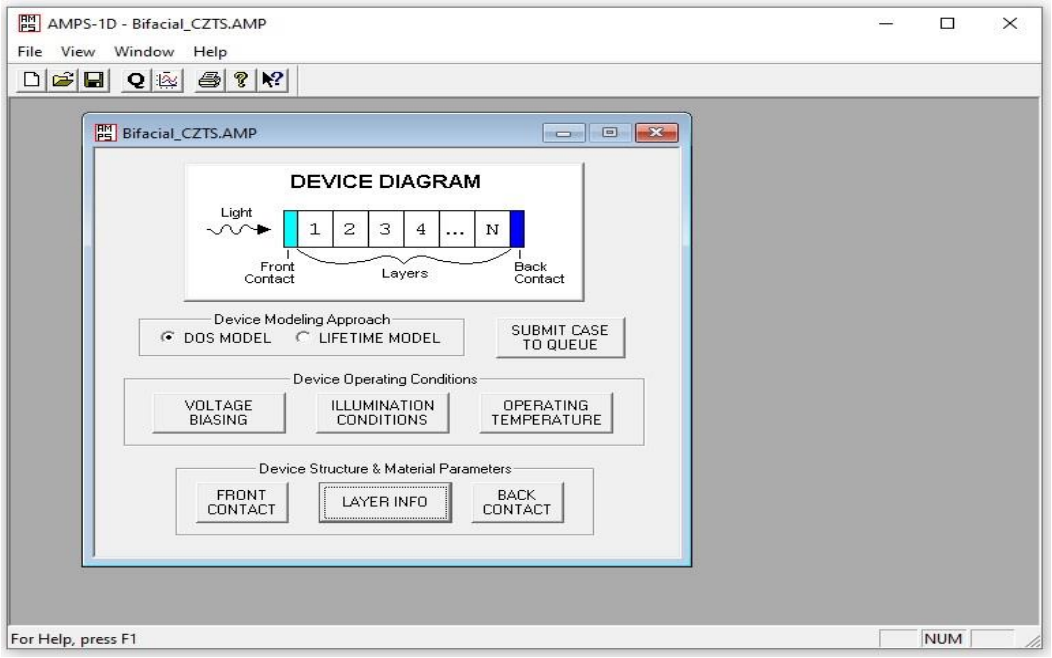

Fig. II.2: AMPS-1D graphic interface.

In this chapter, we use Silvaco simulation environment to simulate and study the substrate CZTS solar cell and the tandem CZTS/CZTSe Cell, while AMPS-1D is used to simulate the Bifacial CZTS solar cell and to study the TCO back side work function effect on their performance.

II.4 TCO's application in CZTS cell structures

II.4.1 Substrate CZTS solar cells

The initial structure subjected to simulation is the conventional substrate CZTS solar cell, comprising a Cu_2ZnSnS_4 (CZTS) absorber layer on a Molybdenum (Mo) back contact, a Cadmium sulfide (CdS) buffer layer, and a Zinc oxide (ZnO) window layer, with a Transparent Conductive Oxide (TCO) such as ZnO:Al serving as the front contact [18,19]. All these layers are assumed to be deposited on Soda Lime Glass (SLG).

Fig. II.3(a) illustrates the schematic representation of the CZTS/CdS/ZnO/ZnO:Al device to be simulated, while Fig. II.3(b) provides a Scanning Electron Microscopy (SEM) cross-section of an experimental CZTS/CdS/ZnO/ZnO:Al solar cell realized by Wangperawong *et al.* (2011) [20].

The material parameters utilized for numerical analysis, sourced from the literature, are systematically presented in Table II.1. The two-dimensional Silvaco-Atlas simulator requires the determination of the wavelength-dependent refractive index n(λ) and extinction coefficient k(λ) for the etch-used layer. Typically, these parameters are obtained from the Atlas database. In our research, we derived the refractive index n(λ) and extinction coefficient k(λ) for CZTS layers from Mirzaei *et al.* (2021) [22]. For CdS and ZnO materials we derived n(λ) and k(λ) from Nima (2014) [23]. Optical constants for the metal contact material (Mo) and ZnO:Al (TCO) were acquired from the Sopra database within the SILVACO/Atlas simulator for inclusion in our simulations. Throughout the study, the surface recombination velocities for holes/electrons (S_n/S_p) at the front and back contacts were set at 1×10^7 cm/s, and the operating temperature of the solar cells was maintained at 300 K.

Poly-crystalline materials such as CIGS and CZTS likely harbor numerous defect states within their material's band gap, to the extent that they can be viewed as continuous. While defects in CIGS have been extensively studied, the understanding of defects in CZTS thin films remains relatively scarce.

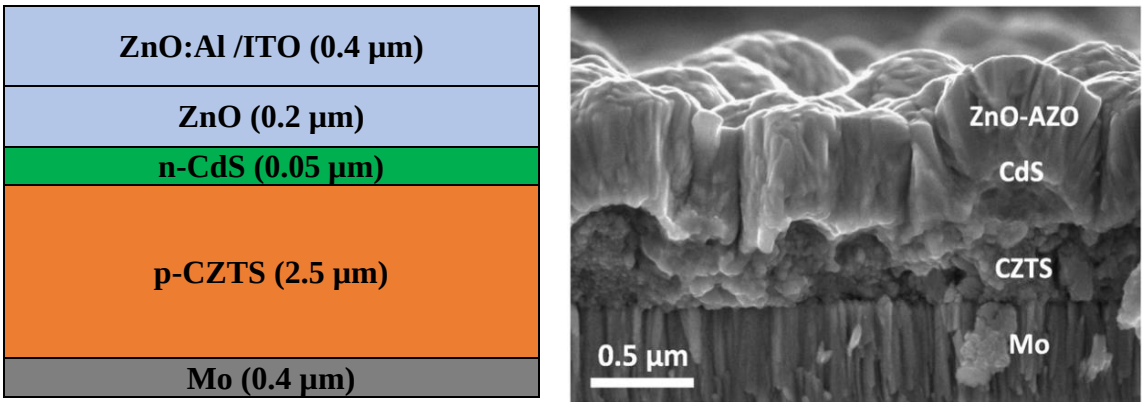

(a) (b)

Fig. II.3: (a) Substrate CZTS solar cell structure, (b) SEM Cross section of CZTS cell[20].

Table II.1: Material parameters used in the simulation.

Layer properties	**CZTS [19, 21]**	**CdS [19, 21]**	**ZnO [19 ,21]**
Thinkness (µm)	2.5	0.05	0.2
Bandgap E_g (eV)	1.5	2.4	3.3
Electron affinity χ_e (eV)	4.5	4.2	4.4
Dielectric permittivity	7	10	9
Electron mobility μ_n (cm^2/Vs)	60	100	100
Hole mobility μ_p (cm^2/Vs)	20	25	25
CB density of states N_c ($1/cm^3$)	2.2×10^{18}	2.2×10^{18}	2.2×10^{18}
VB density of states N_v ($1/cm^3$)	1.8×10^{19}	1.8×10^{19}	1.8×10^{19}
Donor density N_D ($1/cm^3$)	0	10^{17}	10^{18}
Acceptor density N_A ($1/cm^3$)	2×10^{14}-7×10^{18}	0	0
Extinction and refractive index (k,n)	[22]	[23]	[23]

Sravani *et al.* (2021) [24] conducted a comprehensive study on defects in CZTS/CZTSe, proposing that the total density of states comprises four bands. These include two tail bands, characterized as a donor-like valence band and an acceptor-like conduction band, along with two deep level bands, one acceptor-like and the other donor-like. The band-tails demonstrate an exponential decay, whereas the other deep defects are characterized by a Gaussian shape.

$$g(E) = g_{TA}(E) + g_{GA}(E) + g_{TD}(E) + g_{GD}(E) \quad \text{(II.2)}$$

Here, E represents the defect energy, with the subscripts (G, T, A, D) denoting Gaussian and Tail acceptor and donor defect states, respectively. The donor and acceptor defect distributions are provided by ATLAS [24,16]:

$$g_{TA}(E) = N_{TA} \exp\left(-\left(\frac{E - E_C}{W_{TA}}\right)^2\right) \quad \text{(II.3)}$$

$$g_{GA}(E) = N_{GA} \exp\left(-\left(\frac{E_{GA} - E}{W_{GA}}\right)^2\right) \quad \text{(II.4)}$$

$$g_{TD}(E) = N_{TD} \exp\left(-\left(\frac{E_{TD} - E}{W_{TD}}\right)^2\right) \quad \text{(II.5)}$$

$$g_{GD}(E) = N_{GD} \exp\left(-\left(\frac{E - E_{GD}}{W_{GD}}\right)^2\right) \quad \text{(II.6)}$$

The effective density of states (N_{GA}, N_{GD}, N_{TA}, N_{TD}), standard energy deviation (W_{GA}, W_{GD}, W_{TA}, W_{TD}), and the peak energy position, which collectively characterize the density of states (E_{GA} and E_{GD}), are consolidated and presented in Table II.2.

Table II.2: Defect states parameters in CZTS, CdS and ZnO layers.

Parameters	**CZTS [24]**		**CdS [16]**		**ZnO [16]**	
	Tail	**Gaussian**	**Tail**	**Gaussian**	**Tail**	**Gaussian**
WTA/WGA (eV)	1	1	1	0.1	1	1
WTD/WGD (eV)	0.1	0.1	1	1	1	0.1
Defect density NTA/NGA ($cm^{-3}\,eV^{-1}$)	0	0	10^{12}	2.3×10^{17}	10^{12}	0
Defect density NTD/NGD ($cm^{-3}\,eV^{-1}$)	10^{15}	10^{12}	10^{12}	0	10^{12}	10^{17}
Peak energy position EGA/EGD (eV)	-	0.725	-	1.2	-	1.65
Electron capture cross section SIGTAE/SIGGAE (cm^2)	5×10^{-15}	5×10^{-15}	10^{-17}	10^{-17}	10^{-17}	2×10^{-16}
Hole capture cross section SIGTAH/SIGGAH (cm^2)	10^{-14}	10^{-14}	10^{-15}	10^{-12}	10^{-15}	2×10^{-15}
Electron capture cross section SIGTDE/SIGGDE (cm^2)	10^{-14}	10^{-14}	10^{-15}	5×10^{-17}	10^{-15}	10^{-12}
Hole capture cross section SIGTDH/SIGGDH (cm^2)	5×10^{-15}	5×10^{-15}	10^{-17}	10^{-12}	10^{-17}	10^{-15}

Solar cells are subjected to various recombination mechanisms, typically involving three primary processes concurrently within a semiconductor material. These mechanisms include Shockley–Read–Hall (SRH), Auger, and radiative recombination. Radiative recombination is particularly dominant in direct bandgap semiconductors, where an electron from the conduction band directly combines with a hole in the valence band, emitting a photon. SRH recombination occurs through defects with energy levels within the band gap. Auger Recombination involves three carriers, where an electron and a hole recombine, transferring the energy to a third carrier, an electron in the conduction band. This third electron then thermalizes back down to the conduction band edge. The total recombination rate is the sum of these three mechanisms.

In Atlas, these mechanisms are implemented by specifying SRH, AUGER, and OPTR parameters on a MODEL statement. Table II.3 provides a summary of the parameters associated with these models.

Table II.3: Recombination parameters for CZTS, CdS and ZnO.

Mechanisms	**Parameters**
Auger (cm^6/s)	AUGN=10^{-24} for electrons, AUGP=10^{-29} for holes [24]
Radiative (cm^3/s)	COPT=1.5×10^{-10} (between 10^{-11} -10^{-9}) [24]
SRH (cm^3/s)	TAUN =10^{-7}, TAUP=10^{-7} [24]

II.4.1.1 Effect of CZTS absorber layer thickness

In this section, we will examine the performance of the CZTS/CdS/ZnO/ZnO:Al solar cell using the material parameters outlined in Table II.1. Fig. II.4 illustrates the merit patterns of V_{oc}, J_{SC}, *FF*, and η for the CZTS/CdS/ZnO/ZnO:Al solar cell concerning the p-CZTS absorber layer thickness.

As the thickness (t_{CZTS}) of the CZTS layer varies from 0.2 to 15 μm, J_{SC} exhibits a significant increase from 9.42 mA/cm^2 to 15.42 mA/cm^2, while η rapidly rises from 6.33% to approximately 15.42%. V_{oc} reaches 0.97 V, and fill factor FF reaches 83%. All photovoltaic properties remain nearly constant for a thick p-CZTS absorber layer, particularly when exceeding 3 μm. This observed behavior is a consequence of enhanced photon absorption and increased electron-hole generation within the CZTS absorber layer. Consequently, an optimal thickness of 3 μm is identified for the p-CIGS absorber layer to

achieve efficient performance in the CZTS/CdS/ZnO/ZnO:Al solar cell. It is noteworthy that reducing the absorber layer thickness below 2 µm brings the back contact dangerously close to the depletion region, leading to a dramatic decrease in efficiency (η).

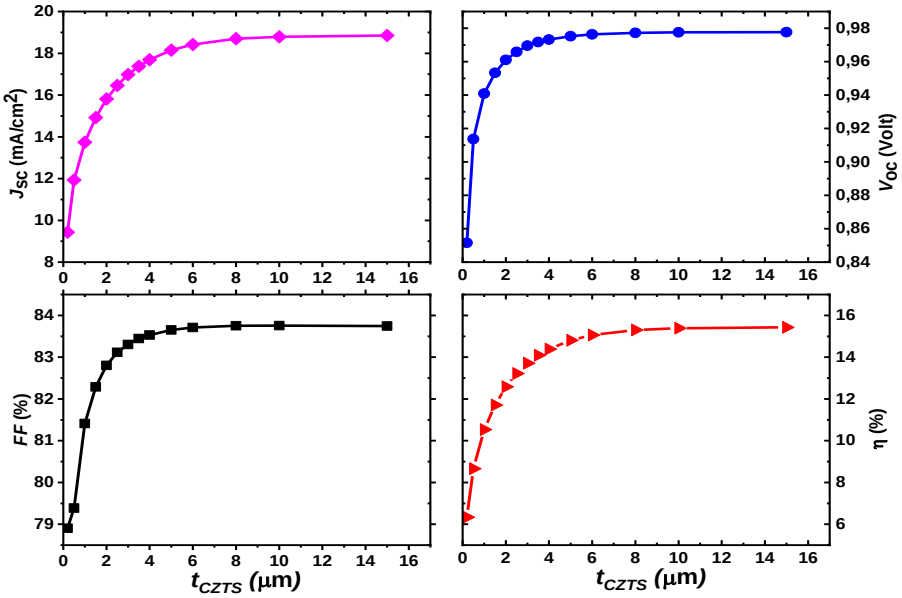

Fig. II.4: Substrate CZTS/CdS/ZnO/ZnO:Al cell performances with various CZTS thickness.

The Quantum Efficiency (QE) measurement of a solar cell serves as an indicator of its effectiveness in converting sunlight into electricity. It is calculated by comparing the number of carriers collected by the solar cell structure to the number of photons at a specific wavelength on the solar cell structure. Fig. II.5 illustrates how the quantum efficiency (QE) varies with the thickness of CZTS. The QE shows a proportional increase with CZTS thickness, suggesting an overall enhancement in performance. This improvement is likely attributed to the increased absorber thickness, leading to the generation of more electron-hole pairs and subsequently enhancing the conversion efficiency of the structure. For a low CZTS thickness (1 µm), the effective absorption zone is confined between 400 nm and 650 nm. With a CZTS thickness, the QE cutoff of the CZTS cell is at 850 nm corresponds to the CZTS band gap [18]. Beyond 800 nm, the QE data decreases rapidly, primarily due to the intrinsic properties of the CZTS material. The quantum efficiency below 400 nm is constrained by the cut-off of the ZnO window layer [25]. this effect has a limited impact on solar cell performance because the power from the AM1.5 spectrum at such low wavelengths is minimal.

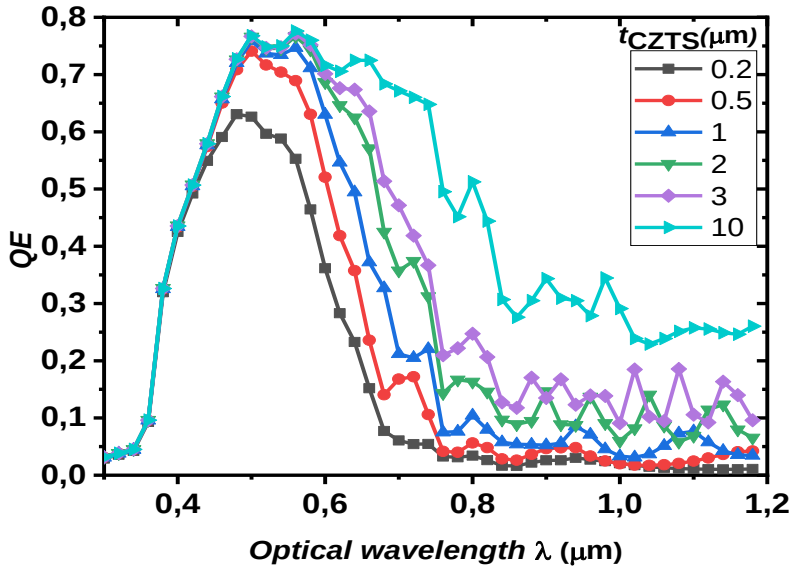

Fig. II.5: External quantum efficiency of CZTS solar cell for different CZTS thickness.

II.4.1.2 Effect of CZTS absorber layer's carrier concentration

The absorber layer's acceptor concentration, N_A(CZTS), was varied from 5×10^{14} cm^{-3} to 5×10^{17} cm^{-3}, and the simulated photovoltaic characteristics are presented in Fig. II.6.

The short-circuit current density (J_{SC}) shows a marginal decrease from 15.75 mA/cm^2 at a concentration of 5×10^{14} cm^{-3} to a satisfactory level of 17.5 mA/cm^2 at a concentration of 10^{17} cm^{-3}. This decrease is attributed to an increase in free carrier charge recombination within the bulk. Notably, J_{SC} decreases significantly to approximately 4.5 mA/cm^2 at a concentration of 5×10^{14} cm^{-3}. Conversely, the open-circuit voltage (V_{oc}) increases from 0.06 volts to 1.1 Volts for a concentration of 5×10^{14} cm^{-3}. The fill factor (*FF*) and efficiency (η) reach their maximum values at concentrations of 2×10^{16} cm^{-3} and 3×10^{16} cm^{-3}, respectively.

The optimum efficiency of 13.86% is achieved at an acceptor concentration of approximately 3×10^{16} cm^{-3}, with $J_{SC} \approx 17.13$ mA/cm^2, $V_{oc} \approx 0.98$ V, and $FF \approx 82.4\%$. Beyond this concentration, a notable decline is observed in V_{oc}, *FF*, and efficiency. The current density (*J*) depicted in Fig. II.7 indicates that for N_A(CZTS) exceeding 5×10^{16} cm^{-3}, the overall performance of the cell decreases. while, a concentration lower than 5×10^{16} cm^{-3} results in a decrease in open-circuit voltage (V_{oc}). Overall, the findings indicate that the optimal range for N_A(CZTS) is between 10^{16} cm^{-3} and 5×10^{16} cm^{-3} to achieve optimal performance.

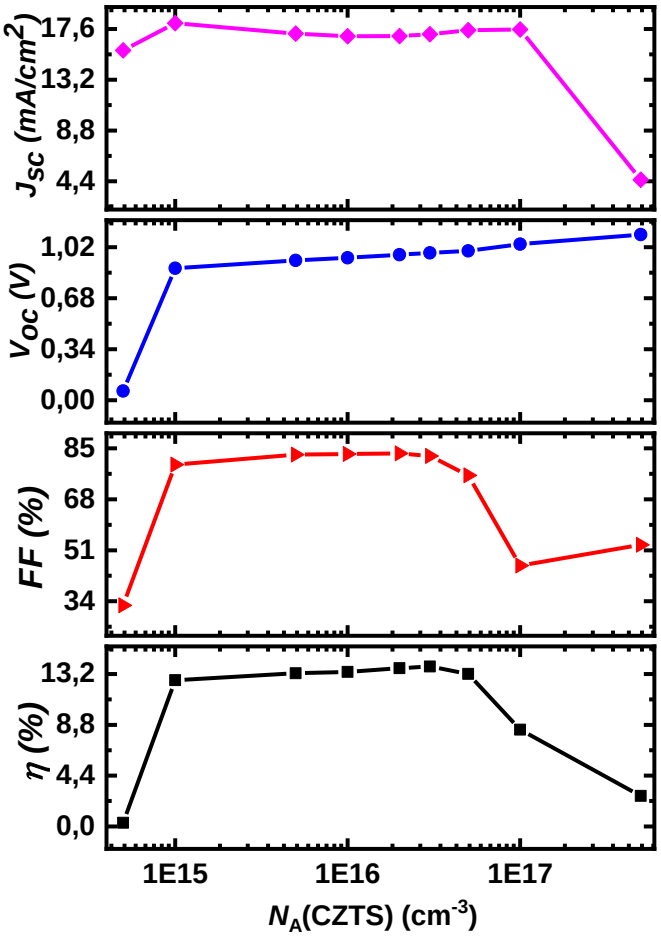

Fig. II.6: Effect of absorber layer's carrier concentration of CZTS substrate solar cell performances.

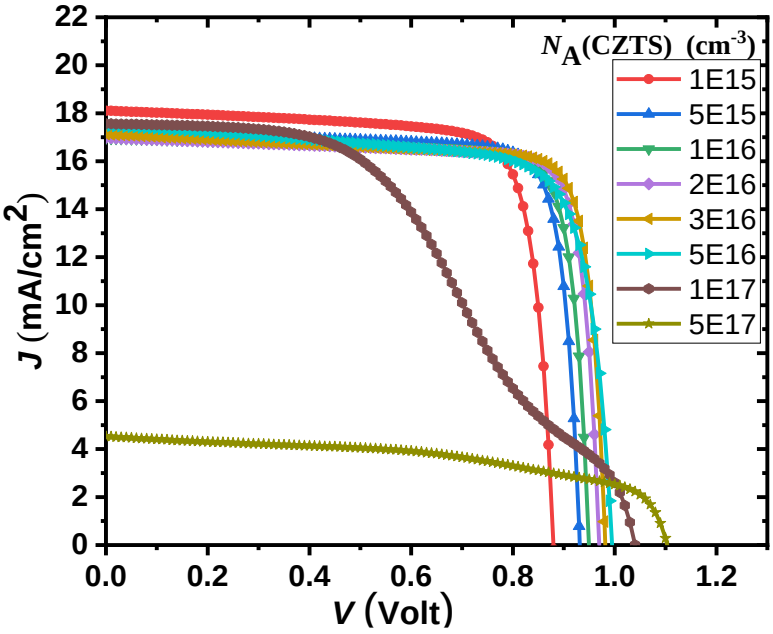

Fig. II.7: J-V characteristic of CZTS/CdS/ZnO/ZnO:Al substrate solar cell for different absorber carrier concentration.

II.4.1.3 Effect of buffer layer thickness

The impact of varying the CdS buffer layer in substrate CZTS/CdS/ZnO:Al cell structure has been fine-tuned. In this simulation, the buffer layer thickness was systematically adjusted from 0.01 µm to 0.2 µm, with the absorber layer thickness held constant at 3 µm. Fig. II.8 illustrates the alterations in photovoltaic parameters corresponding to the buffer thickness.

It's clear from Fig. II.8, that the short-circuit current density (J_{SC}), fill factor (*FF*), and efficiency (η) exhibit a pronounced dependency on the buffer thickness. Their optimal values align with the smallest thickness, whereas the open-circuit voltage (V_{oc}) remains relatively constant at approximately 0.96 Volts. The suggestion is that an improved solar performance necessitates a very thin layer of CdS. This expectation arises from the understanding that reducing the buffer layer thickness minimizes optical absorption losses [26]. However, the selection of the optimal CdS thickness should be made judiciously, taking into account technological constraints, particularly the challenges associated with attaining a uniform and high-quality thin CdS layer [27].

II.4.1.4 Effect of buffer layer's carrier concentration

For a constant CdS buffer thickness of 0.05 µm, the dopant concentration N_D(CdS) was incrementally raised from 10^{15} cm^{-3} to 5×10^{17} cm^{-3}. Fig. II.9 illustrates the figures of merit.

The short-circuit current density (J_{SC}) remains nearly constant until the dopant concentration N_D(CdS) exceeds 10^{17} cm^{-3}, where a slight decrease is observed. The open-circuit voltage (V_{oc}) gradually decreases with the increasing dopant concentration N_D(CdS). The fill factor (*FF*) experiences a significant increase, ranging from 54% to 84% for a dopant concentration of 5×10^{17} cm^{-3}. The efficiency (η) reaches its peak value at a concentration of 5×10^{16} cm^{-3}, while the dopant concentration has a marginal impact on J_{SC} and V_{oc}, a higher dopant concentration N_D(CdS) between 5×10^{16} and 10^{17} cm^{-3} is chosen to achieve the highest electrical efficiency.

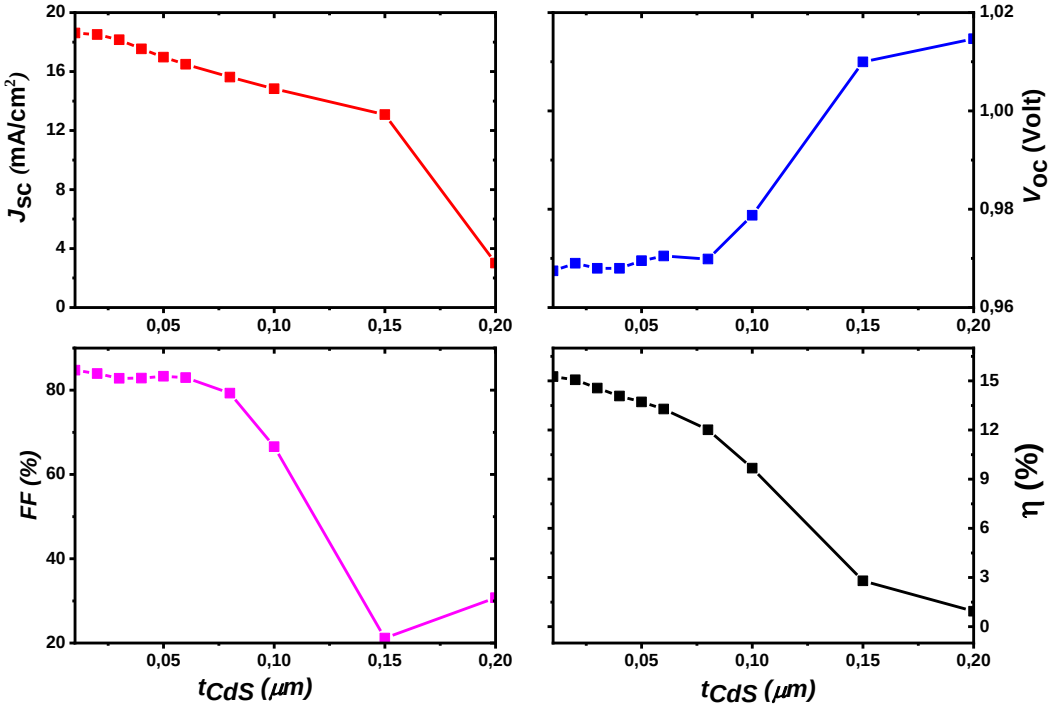

Fig. II.8: Substrate CZTS/CdS/ZnO/ZnO:Al cell performance with various buffer thickness.

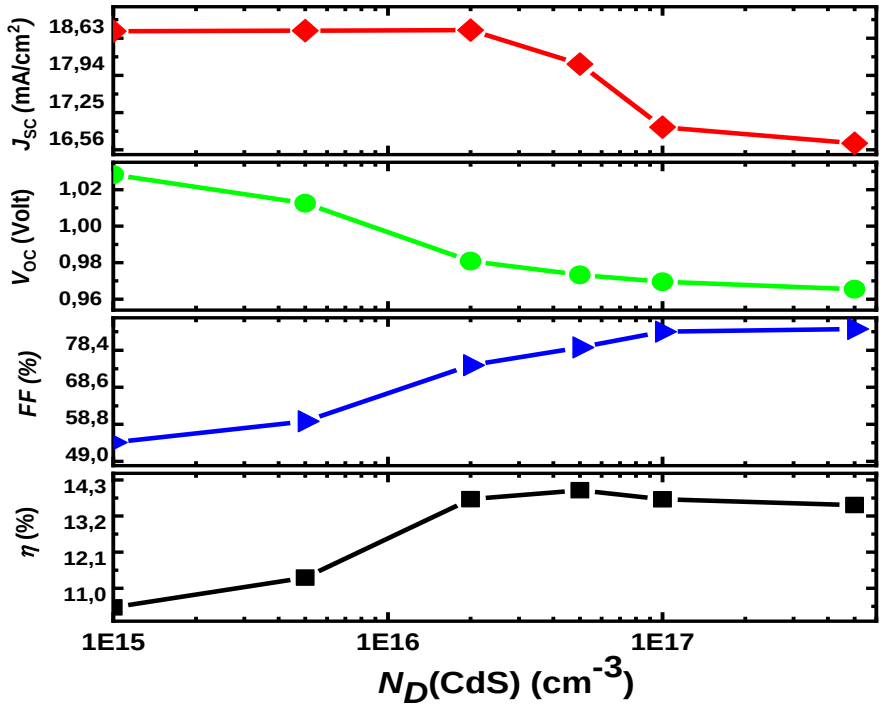

Fig. II.9: CZTS cell performances according to carrier concentration of CdS buffer layer.

II.4.1.5 Cd-free buffer for CZTS solar cell

The fabrication processes for CZTS in photovoltaic applications have incorporated both the Mo back contact and the high-toxic heavy-metal Cd buffer from CIGS. Despite CdS showing good band alignment with the CIGS absorber, the CZTS/CdS cell's band alignment may not be fully optimized. Amongst other affordable and non-toxic alternatives, Zn(O,Sn) and Zn(O,S) exhibit significant promise, demonstrating power conversion efficiencies comparable to those of CZTS/CdS junctions.

Fig. II.10(a) illustrates similar CZTS solar cell performances with environmentally friendly materials, and the parameters of the used materials are detailed in Table II.4.

(a)

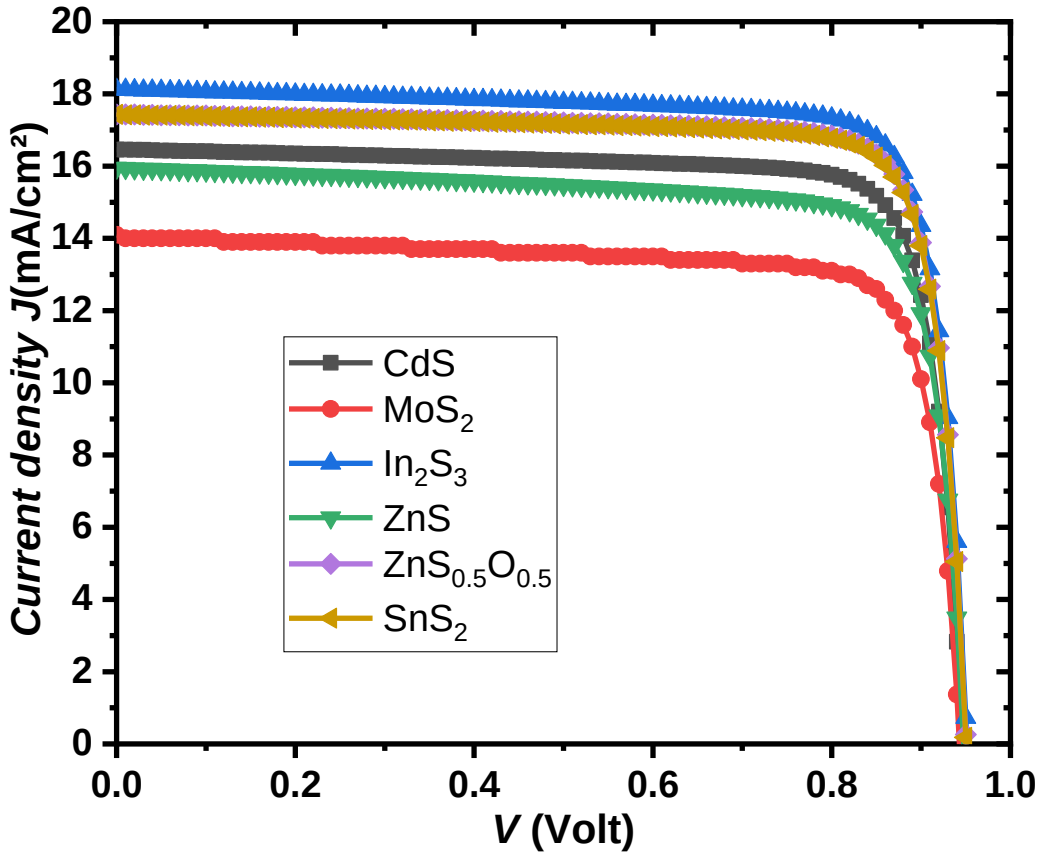

(b)

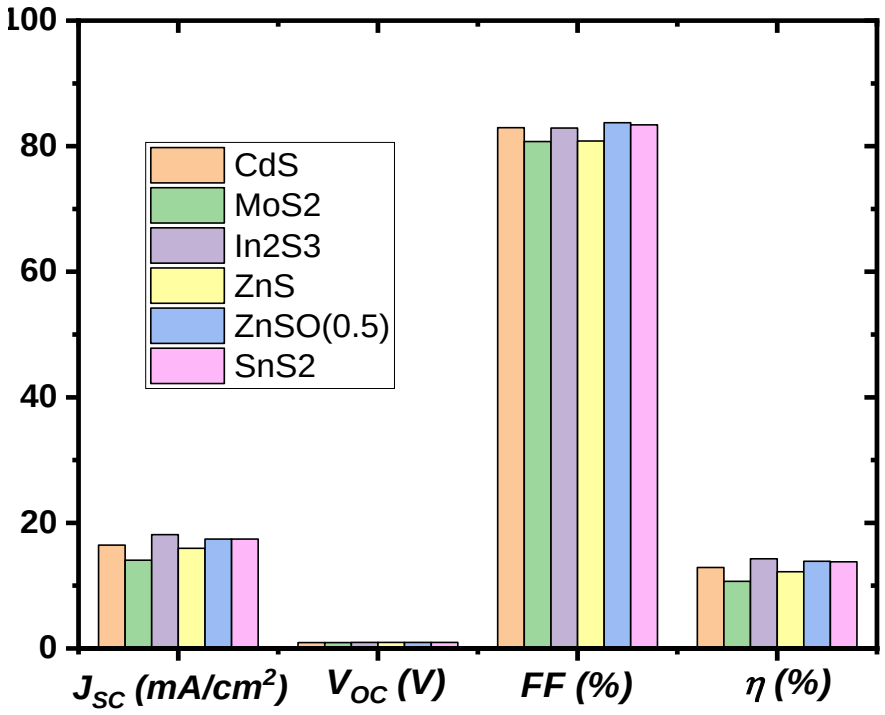

Fig. II.10: (a) *J-V* characteristic of CZTS cell for different buffer layer materials and (b) CZTS cell performance with different buffer layers.

Table II.4: Material parameters used in the simulation

Material properties	**CdS [19,21,28]**	**In_2S_3 [19]**	**ZnS [19]**	**$ZnS_{0.5}O_{0.5}$ [29]**	**SnS_2 [30]**	**MoS_2 [34]**
Thinkness (μm)	0.05	0.05	0.05	0.05	0.05	0.05
Bandgap E_g (eV)	2.4	2.8	3.5	2.6	2.24	1.7
Electron affinity χ_e (eV)	4.2	4.7	4.5	3.8	4.24	4.2
Dielectric permittivity	10	13.5	10	10	10	13.6
Electron mobility μ_n (cm^2/Vs)	100	400	50	100	50	100
Hole mobility μ_p (cm^2/Vs)	25	210	20	25	50	25
CB density of states N_c ($1/cm^3$)	2.2×10^{18}	1.8×10^{19}	4×10^{18}	2.2×10^{18}	2.2×1018	2.2×10^{18}
VB density of states N_v ($1/cm^3$)	1.8×10^{19}	4×10^{13}	9×10^{18}	1.8×10^{19}	1.8×1019	1.8×10^{19}
Donor density N_D ($1/cm^3$)	10^{17}	10^{17}	10^{17}	10^{17}	10^{17}	10^{17}
Extinction and refractive index (k,n)	[14]	[32]	[31]	Calculated using Wien2K	[33]	[35]

II.4.1.6 Effect of MoS_2 layer on CZTS/CdS/ZnO/ZnO:Al cell performance

The initial development of CZTS solar cells aimed to replace CIGS solar cells, utilizing cost-effective and abundant materials while avoiding the use of Indium. The proposed CZTS cells initially adopted the same configuration as the conventional CIGS cells. However, subsequent studies revealed that the CZTS/Mo interface lacks the chemical stability observed in the CIGS/Mo interface. During thermal processing, Mo reacts with CZTS, leading to the formation of a MoS_2 interfacial layer [18,36]. This section considers this critical aspect. In Fig. II.11(a), a schematic representation depicts the Mo/MoS_2/CZTS/CdS/ZnO/ZnO:Al device scheduled for simulation. Fig. II.11(b) presents a SEM cross-section of an experimental CZTS/CdS/ZnO/ZnO:Al solar cell realized by Yuan T. *et al.* (2015) [37]. The material parameters utilized for numerical analysis are mentioned before in Table II.1, and Table II.4. We derived the refractive index n(λ) and extinction coefficient k(λ) for MoS_2 layers from Islam *et al.* (2021) [35].

Fig. II.12 illustrates the density current $J(V)$ and the Quantum Efficiency (QE) measurement of a solar cell with a MoS_2 interfacial layer of 0.1 µm. The result indicates a notable improvement in all cell performance aspects, with the (J_{SC}) increasing from 12.9 mA/cm² to 15.11 mA/cm².

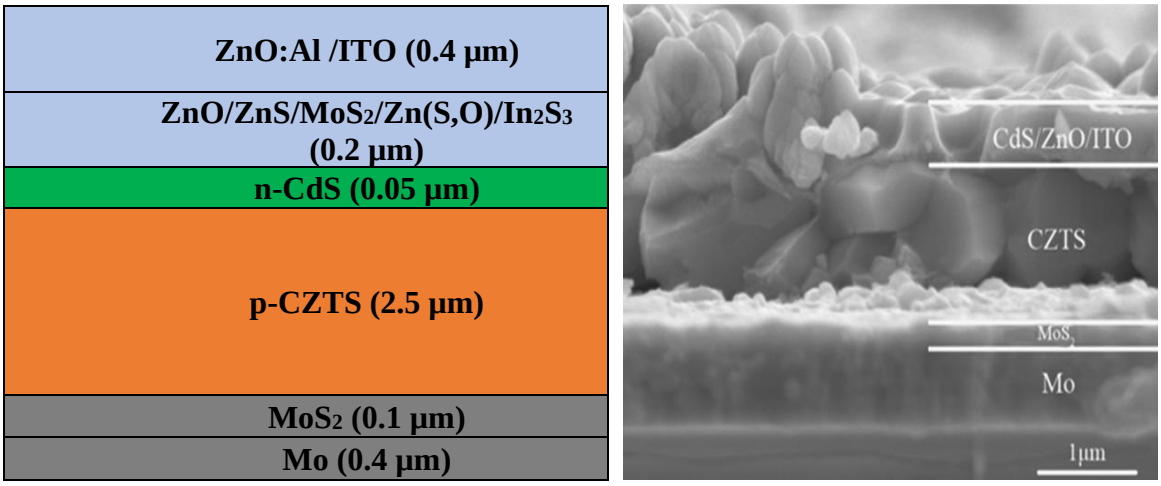

(a) (b)

Fig. II.11: (a) Substrate CZTS solar cell structure, (b) SEM Cross section for CZTS solar cell [37].

Experimental observations [18,38] indicate that the formation of thick MoS_2 often occurs, leading to an increase in the device's series resistance (R_s). This, in turn, adversely affects the fill factor (FF) and overall device efficiency. This paradox can be elucidated by

recognizing that MoS_2 formation introduces CZTS decomposition into secondary phases, such as $Cu_{2-x}S$, ZnS, and SnS, thereby compromising the quality of the absorber.

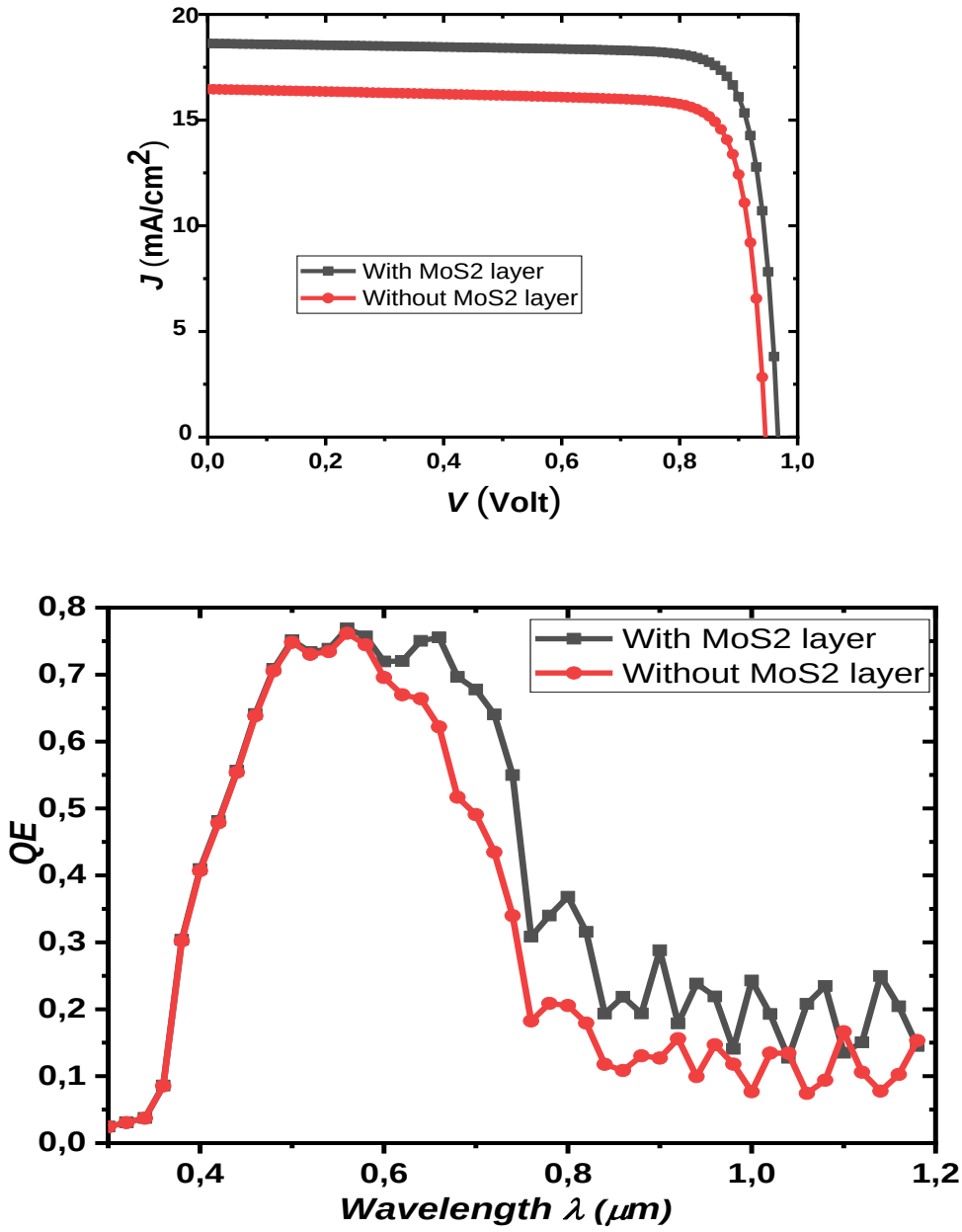

Fig. II.12: Effect of MoS_2 back contact layer on CZTS solar cell performances.

To address this issue, the adoption of a new back contact material or the incorporation of an intermediate layer between the CZTS absorber and the back contact proves effective in enhancing the overall cell efficiency.

II.4.2 Bifacial CZTS solar cells

In the upcoming sections, the analysis will commence with an examination of the CdS/CZTS/Transparent Conductive Oxide (TCO) structure. Initially, the focus will be on

optimizing the thickness of the CZTS layer. Subsequently, the investigation will extend to assess the influence of the barrier height at the CZTS/TCO interface in bifacial CZTS solar cells, considering both front and backside illuminations. Finally, variations in power conversion and quantum efficiencies will be explored.

The simulated bifacial solar cell structure depicted in Fig. II.13 is characterized by its simplicity. This structure involves up to four regions, each delineated by distinct material parameters, doping profiles, and electronic and optical properties. Specifically, the cell structure comprises ZnO:Al/CdS/CZTS/Transparent Conductive Oxide (TCO), allowing light ingress through both the ZnO:Al and TCO layers. This model solar cell is utilized for simulation purposes.

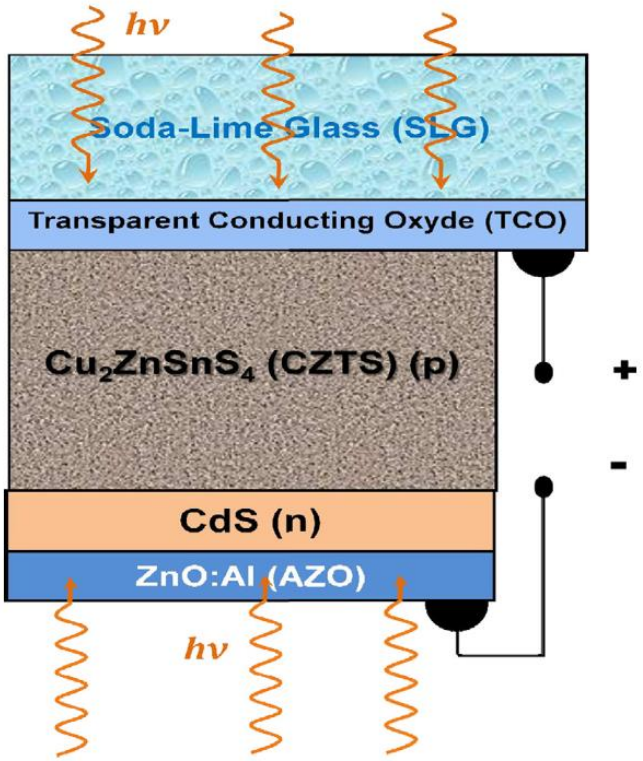

Fig. II.13: Bifacial CZTS thin films solar cell structure.

In this study, the one-dimensional device simulation software, AMPS, was employed. This software is designed to compute the steady-state band diagram, recombination profile, and carrier transport in one dimension. It achieves this by solving the Poisson equation along with the hole and electron continuity equations, expressed as follows [17]:

$$\frac{d}{dx}\left(-\varepsilon(x)\frac{d\psi}{dx}\right)=q\left[p(x)-n(x)+N_d^+(x)+N_A^-(x)+p_t(x)-n_t(x)\right] \qquad \text{(II.7)}$$

$$\frac{dp_n}{dt} = G_p - \frac{P_n - p_{no}}{\tau_p} - p_n \mu_p \frac{d\xi}{dx} - \mu_p \xi \frac{dp_n}{dx} + D_p \frac{d^2 p_n}{dx^2} \quad \text{(II.8)}$$

$$\frac{dn_p}{dt} = G_n - \frac{n_p - n_{po}}{\tau_n} - n_p \mu_n \frac{d\xi}{dx} - \mu_n \xi \frac{dn_p}{dx} + D_n \frac{d^2 n_p}{dx^2} \quad \text{(II.9)}$$

where Ψ is the electrostatic potential and n the free electron, p free hole, n_t trapped electron, p_t trapped hole, N_D^+ the ionized donor-like doping and N_A^- the ionized acceptor-like doping concentrations and ξ the electric field. All these parameters are a function of the coordinate position x. G is the generation rate, D the diffusion coefficient, ε the permittivity and q the charge of electron. Recombination currents are calculated with the Shockley–Read–Hall (SRH) model for bulk defects.

Table II.5: Material parameters used in the simulation.

Layer properties	CZTS	CdS	ZnO:Al
Thinkness (μm)	Calculated	0.1	0.3
Bandgap E_g (eV)	1.52	2.4	3.3
Electron affinity χ_e (eV)	4.1	3.8	4
Dielectric permittivity	10	10	9
Electron mobility μ_n (cm^2/Vs)	100	100	100
Hole mobility μ_p (cm^2/Vs)	25	25	25
CB density of states N_c ($1/cm^3$)	2.2×10^{19}	2.2×10^{19}	2.2×10^{18}
VB density of states N_v ($1/cm^3$)	1.8×10^{18}	1.8×10^{18}	1.8×10^{19}
Donor density N_D ($1/cm^3$)	10	10^{17}	10^{18}
Acceptor density N_A ($1/cm^3$)	2×10^{16}	10	10
Electron Thermal velocity (cm/s)	10^7	10^7	10^7
Hole Thermal velocity (cm/s)	10^7	10^7	10^7

The electrical, optical, and structural parameters utilized for simulating the device performance have been sourced from the literature [39]. Additional critical electrical parameters for the simulation are outlined in Table II.5. The radiation AM1.5G with incident power density of 100 mW/cm^2 is used as illuminating source in present simulations. The absorption coefficient of CZTS absorber layer was taken into Ref. [3]. In our structure a highly doped layer of the TCO serve as a back contact layer. The CdS buffer layer is a n-type with a thickness of 200 nm which is a sufficient value to make a good PN junction. The surface recombination velocities of electrons and holes were both set as 10^7 cm/s.

II.4.2.1 *Why (n+)-type TCO back contact?*

Transparent conducting oxides (TCOs) are n-type degenerate semiconductors, specifically metallic oxides. They encompass binary compounds like SnO_2, In_2O_3, ZnO, as well as ternary compounds such as Cd_2SnO_4, $ZnSnO_3$, $Zn_2In_2O_5$, among others [40]. The

utilization of TCO layers as back contact layers in thin film solar cells prompts the question: Why are TCO layers often chosen for this role? To address this inquiry, examining the properties of TCO layers reveals their suitability as a back contact layer, enabling light transmission into the bottom cell. TCO back contacts facilitate dual-sided characterization (through current-voltage and quantum efficiency measurements) on both the glass and contact sides, enhancing the understanding of device behavior [41]. It is noteworthy that certain CZTS layer preparation techniques necessitate the prior use of thoroughly cleaned TCO-covered glass substrates (TCO substrates) to deposit high-quality CZTS layers, including cost-effective methods like electrodeposition and solvothermal processes [42,43].

Investigating the impact of material properties such as carrier lifetime, mobility, and work function is crucial. Regrettably, much of the existing research on TCO work function is empirical [35], and there is a dearth of studies exploring the influence of these properties on superstrate and/or bifacial CZTS solar cells.

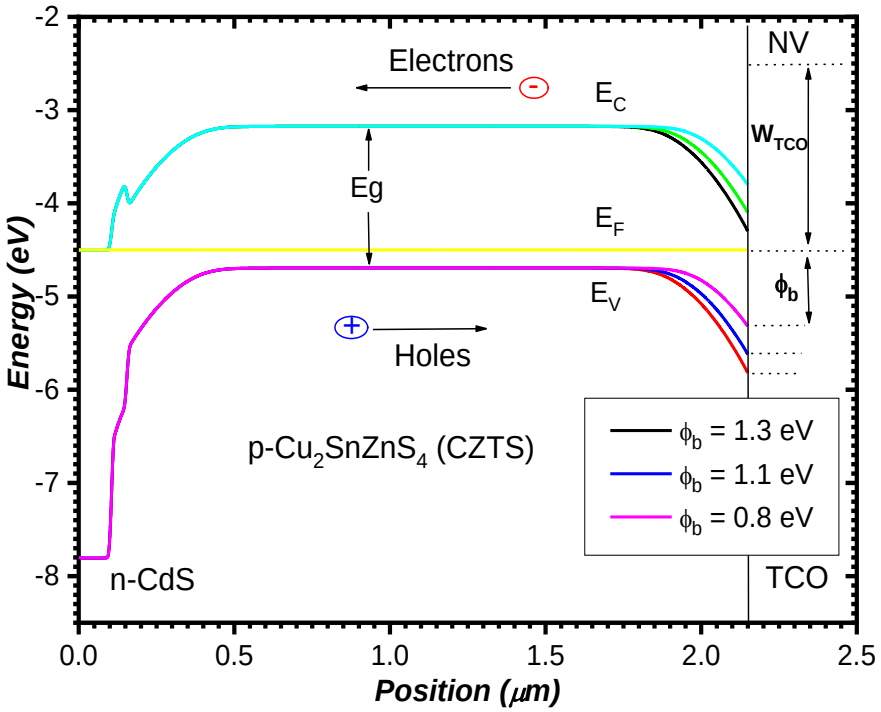

Fig. II.14: ZnO:Al/n-CdS/p-CZTS/TCO solar cell energy band diagram.

The band diagram of our proposed heterostructure has been computed and depicted in Fig. II.14. The formation of an opposing diode, contingent on the work function mismatch (barrier height), between the TCO contact layer and the p-type CZTS absorber layer, can exert a profound influence on the device performance. The characteristics and impact of this opposing diode at the CZTS thin film/TCO junction are predominantly influenced by the

barrier height (Φ_b), as well as the doping and thickness of the CZTS thin film layer connected to the TCO back contact layer. It is important to note that, in these simulations, the exact band line-up for the heterojunction between the CZTS absorber layer and the TCO back contact layer is not explicitly represented, as the TCO is treated as a "conductive" layer characterized by its interface work function.

II.4.2.2 Optimum thickness of CZTS layer

To achieve cost reduction, it is desirable to minimize the thickness of the CZTS absorber layer while maintaining acceptable performance. The optimal thickness determined in our study will be used in subsequent simulation work.

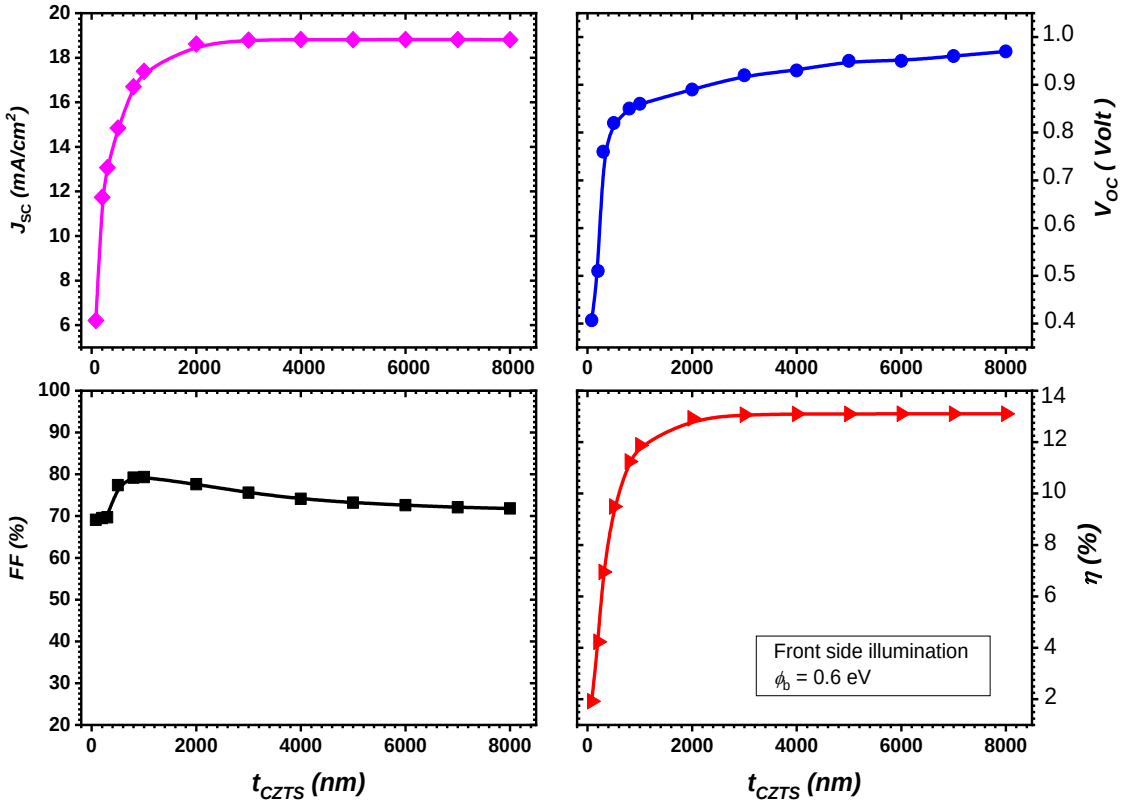

Fig. II.15: Photovoltaic properties depending on the CZTS layer thickness.

Fig. II.15 illustrates the trends of short-circuit current density (J_{SC}), open-circuit voltage (*Voc*), fill factor (*FF*), and power conversion efficiency (η), all of which are significantly influenced by the absorber thickness. For devices with absorber thicknesses up to 2 µm, J_{SC} remains around 18.4 mA/cm², and *Voc* stays above 0.9 Volt. The fill factor slightly decreases but remains above 75% for all absorber thicknesses. The small reduction in *Voc* for the thinnest CZTS absorber may be attributed to increased recombination at the TCO back contact layer, resulting in a smaller effective minority carrier lifetime. The strong dependency of short-circuit current density on absorber thickness is evident, with J_{SC}

decreasing from 18.8 mA/cm² to 14.8 mA/cm² for a 500 nm-thick absorber. For devices thinner than 1 µm, current loss may stem from optical losses, electrical losses, or a combination of both. Conversion efficiency losses are primarily attributed to the decrease in J_{SC}. The optimum thickness for a CZTS absorber layer would typically be higher than 2 µm. We achieve a maximum conversion efficiency of 12.9% when t_{CIGS} exceeds 2 µm, with FF at 77.6%, *Voc* at 0.89 Volt, and J_{SC} at 18.6 mA/cm².

II.4.2.3 Effect of barrier height in cases of back and front side illuminations

- **Case of the front side illumination**

The J–V characteristics of the bifacial CZTS solar cell under front-side illumination are depicted in Fig. II.16. Various notable features can be observed across the different configurations: Absence of a roll-over curvature at forward bias, indicating the absence of a blocking contact. Despite substantial variations in barrier height, there is no cross-over between the illuminated curves, and there is a significant variation in open-circuit voltage.

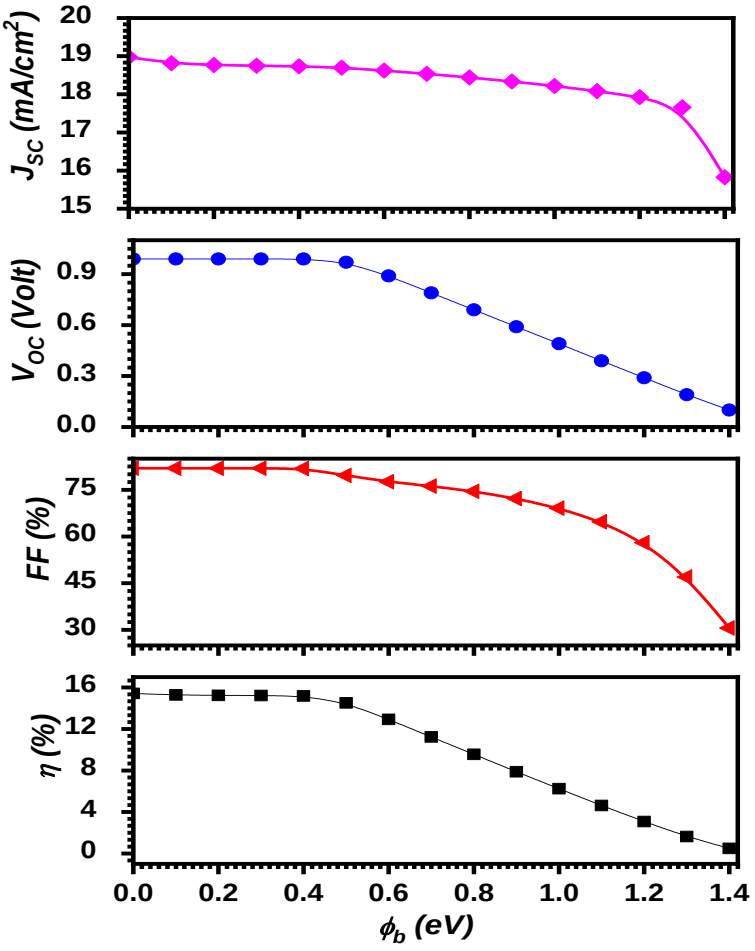

Fig. II. 16: barrier height Impact at the p-CIGS/TCO interface on solar cell performance.

The photovoltaic parameters corresponding to the J–V characteristics are illustrated in Fig. II.16. Notably, barrier heights up to 0.5 eV lead to a reduction in efficiency for this type of solar cell. The maximum efficiency of approximately 15.8% is achieved at barrier height Φ_b =0.1eV. A poor performance is evident at Φ_b = 1.4 eV, with η=0.68%, FF=30%, *Voc* =0.12 Volt, η=0.68%, FF=30%, *Voc* =0.12 V, and J_{SC} =15.8 mA/cm². Conversely, a good performance is observed at Φ_b=0.5 eV, with η=13.2%, FF=71.2%, *Voc* =0.92, η=13.2%, FF=71.2%, *Voc* =0.92 V, and J_{SC} =18.8 mA/cm². Configurations with a barrier height exceeding 1.4 eV exhibit poor or no performance at all.

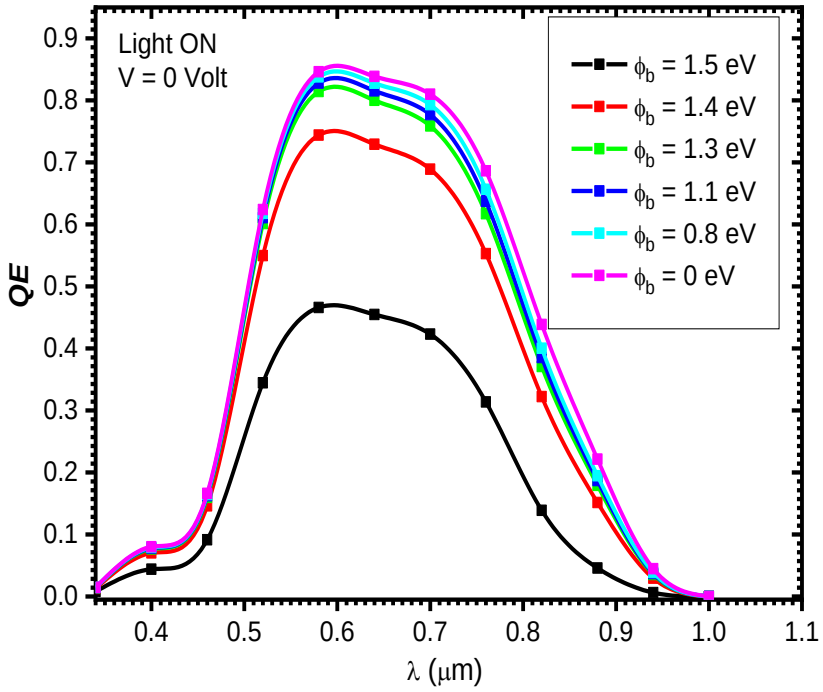

Fig. II.17: Barrier height impact on calculated quantum efficiencies QE (Light ON, Front side illumination).

For a better understanding of current losses with increasing the barrier height, the quantum efficiency QE was calculated and the results are given in Fig. II.17. For wavelength below 450 nm and above 950 nm all samples show nearly the same behavior. In the region between 500 nm and 900 nm significant losses are observable. When the barrier height increases from 0 eV to 1.5 eV the maximum of quantum efficiency increases from 40% to 83%, respectively, corresponding to the wavelength about 580 nm.

- **Case of the back side illumination**

To elucidate the impact of the barrier height (Φ_b) on cell performance under back side illumination, a comprehensive analysis of the energy band diagrams is crucial.

The CdS/CZTS/TCO hetero-junction is examined as varies from 0.1 to 1.4 eV. With back side illumination, where light penetration is limited, only a small fraction of photons reaches the CdS buffer, and few photons reach the PN junction or the space-charge region. Consequently, the opposing diode at the CZTS thin film/TCO junction assumes significance, and the recombination mechanism at the CZTS/TCO interface becomes a dominant factor.

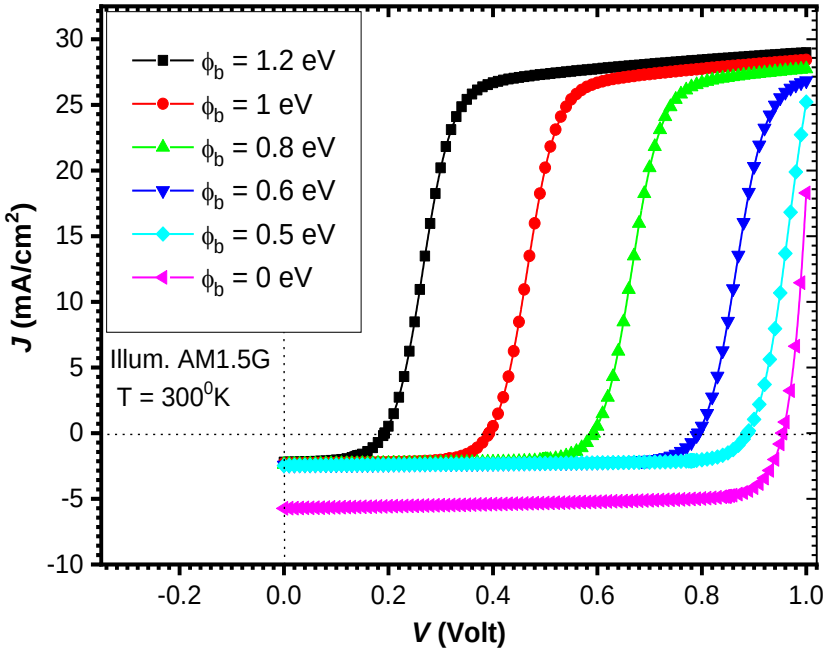

Fig. II.18: *J-V* characteristics of the structure with back side illumination.

The simulated J–V characteristics for the solar cell with back side illumination are presented in Fig. II.18. Notably, a roll-over curvature is observed at forward bias, signifying that the current attains a saturation value determined by the barrier height.

The photovoltaic parameters, as shown in Fig. II.19, reveal that the bifacial CZTS solar cells exhibit a very low conversion efficiency ($\eta \leq 2\%$) for barrier heights (Φ_b) lower than 0.2 eV.

The rise in W_{TCO} reduces the Schottky barrier height between TCO and p-CZTS layers, facilitating the collection of more hole carriers at the back contact. The maximum efficiency is 4% for barrier heights (Φ_b) lower than 0.1 eV.

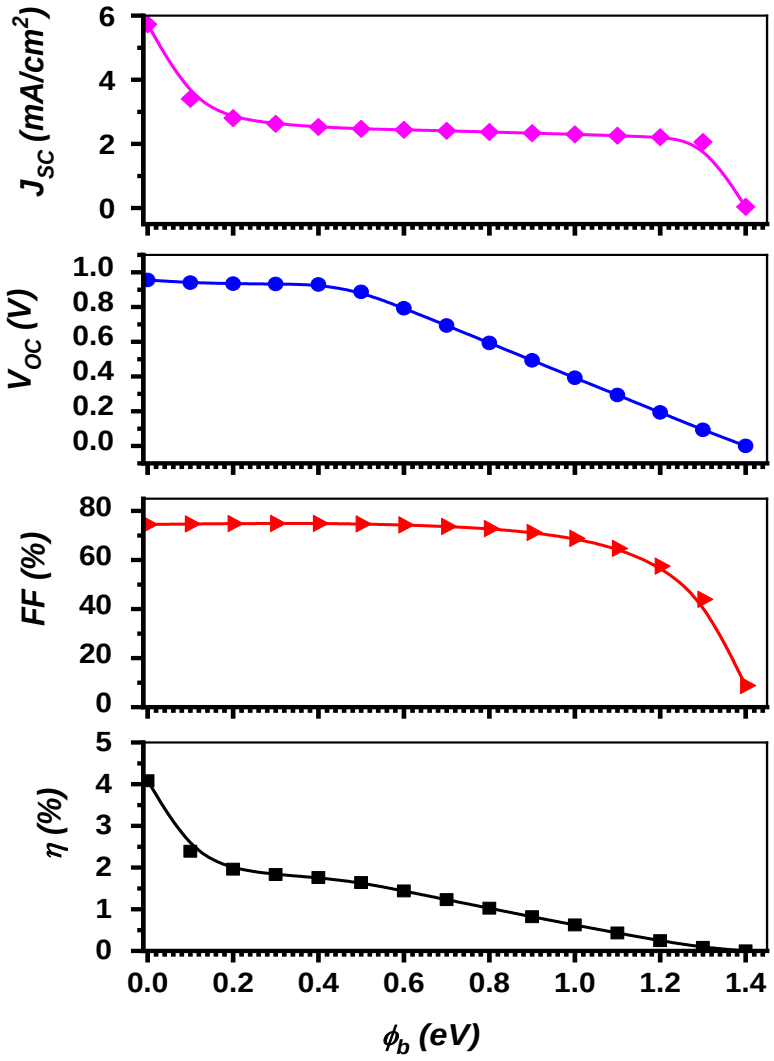

Fig. II.19: Photovoltaic parameters of bifacial solar cells with back side illumination.

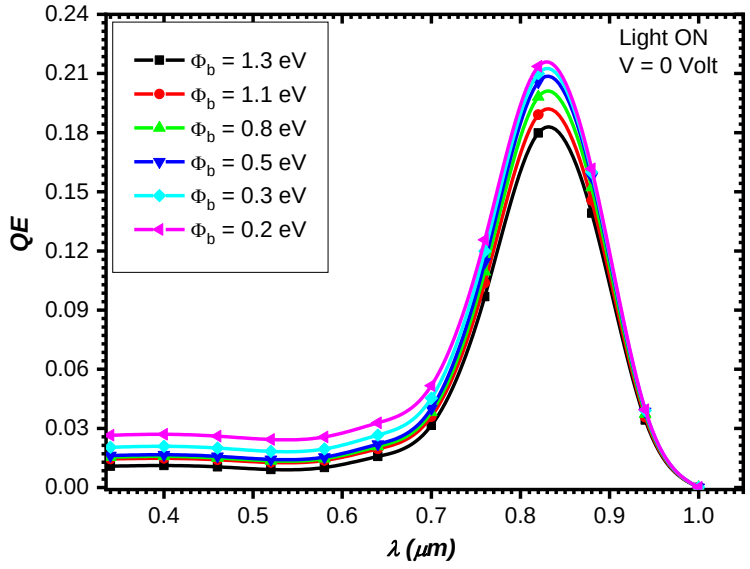

Fig. II. 20: Obtained quantum efficiencies for bifacial solar cells vs CZTS/TCO barrier height (Light ON, Back side illumination).

The spectral responses for different barrier heights were investigated and depicted in Fig. II.20. As (Φ_b) increases, the spectral response diminishes in the long-wavelength region. The quantum efficiency reaches a peak value of approximately 21% under 100 mW/cm^2 for a wavelength around 820 nm.

II.4.3 Tandem CZTS/CZTSe solar cell

In recent studies, efforts have been directed towards enhancing the efficiency of solar cells utilizing a $Cu_2ZnSn(S,Se)_4$ (CZTSSe) absorber layer. The most noteworthy achievements in kesterite solar cell efficiency have been reported, reaching 11.4% for Cu_2ZnSnS_4 (CZTS) and 14.9% for $Cu_2ZnSnSe_4$ (CZTSe) [44]. This performance limitation is attributed to the absorber layer bandgap (*E*g), wherein photons with energies lower than (*E*g) remain unabsorbed, and those with energies exceeding *E*g result in thermalization losses, rendering them unproductive for device output. Addressing this challenge, multijunction and tandem solar cells have emerged as effective solutions. Multijunction solar cells, with layers possessing distinct bandgap energies that exploit various regions of the solar spectrum, hold the promise of significantly increasing efficiency.

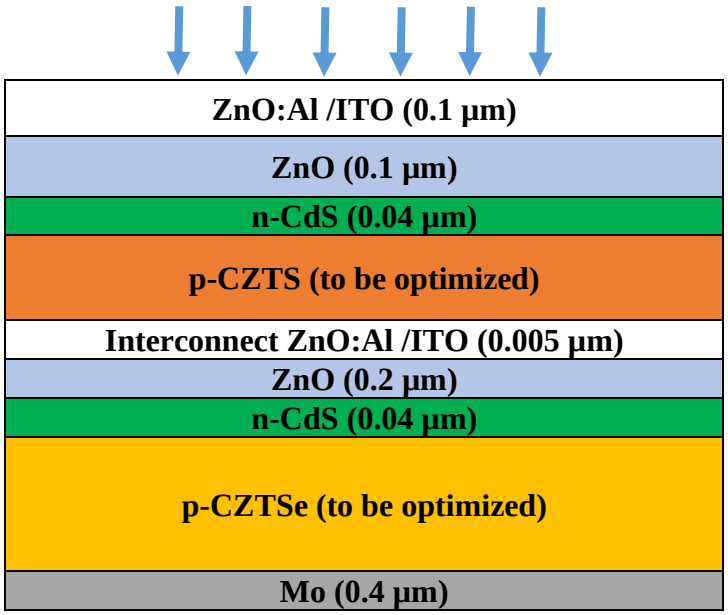

Fig. II.21: Tandem CZTS/CZTSe solar cell structure.

Fig II.21 present a tandem cell where, CZTS (*E*g = 1.52 eV) and CZTSe (Eg = 1.0 eV) are integrated in tandem, collectively capturing the incident light spectrum. The upper layer, characterized by a higher band gap, selectively absorbs high-energy photons, corresponding to the lower-wavelength portion of the incident spectrum. Conversely, the lower-energy photons in the high-wavelength segment of the spectrum are transmitted through the top cell,

which features a larger band-gap absorber layer. The parameters of the CZTSe layer are detailed in Table II.6. We derived the refractive index n(λ) and extinction coefficient k(λ) for CZTSe layers from Hirate *et al.* (2021) [45].

Table II.6: CZTSe layer parameters used in the simulation.

Layer properties	**CZTSe [46]**
Thickness (µm)	4 (*optimized value*)
Bandgap E_g (eV)	1.04
Electron affinity χ_e (eV)	4.05
Dielectric permittivity	7
Electron mobility μ_n (cm^2/Vs)	145
Hole mobility μ_p (cm^2/Vs)	35
CB density of states N_c ($1/cm^3$)	2.2×10^{18}
VB density of states N_v ($1/cm^3$)	1.8×10^{19}
Donor density N_D ($1/cm^3$)	0
Acceptor density N_A ($1/cm^3$)	4×10^{16} (*optimized value*)
Real refractive index coefficients and extinction coefficients	[45]

II.4.3.1 CZTSe solar cell optimization (absorber thickness and carrier concentration)

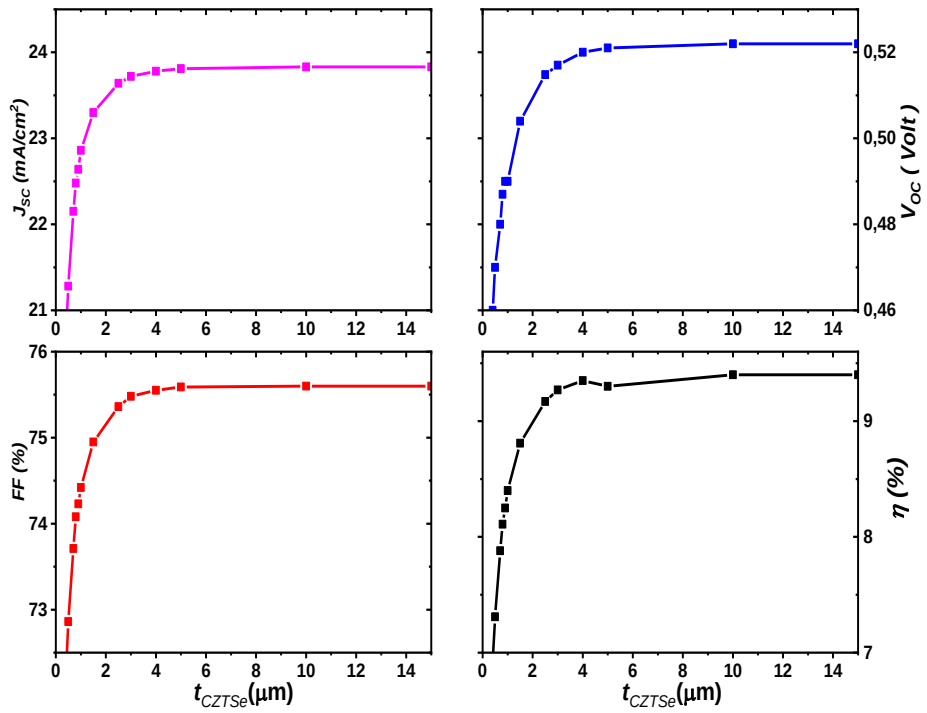

Fig. II.22: Effect of Absorber thickness on CZTSe solar cell performance.

Fig. II.22 illustrates the merit patterns of *V*oc, J_{SC}, *FF*, and η for the CZTSe/CdS/ZnO/ZnO:Al solar cell in function of the CZTSe absorber layer thickness. As

the thickness (t_{CZTS}) of the CZTS layer varies from 0.4 to 15 µm, J_{SC} increase from 20.68 mA/cm² to 23.83 mA/cm^2, while η rapidly rises from 6.92% to approximately 9.4%. *V*oc reaches 0.52 V, and fill factor FF reaches 75.6%. All photovoltaic properties remain nearly constant for a thick CZTSe absorber layer exceeding 4 µm. This observed behavior is a consequence of enhanced photon absorption and increased electron-hole generation within the CZTS absorber layer.

Fig. II.23 show that the optimum *FF* of 75.27% is achieved at an acceptor concentration of approximately 4×10^{16} cm^{-3}, with $J_{SC} \approx 23.54$ mA/cm², $V_{oc} = 0.51$ V, and η = 82.4%. Beyond this concentration.

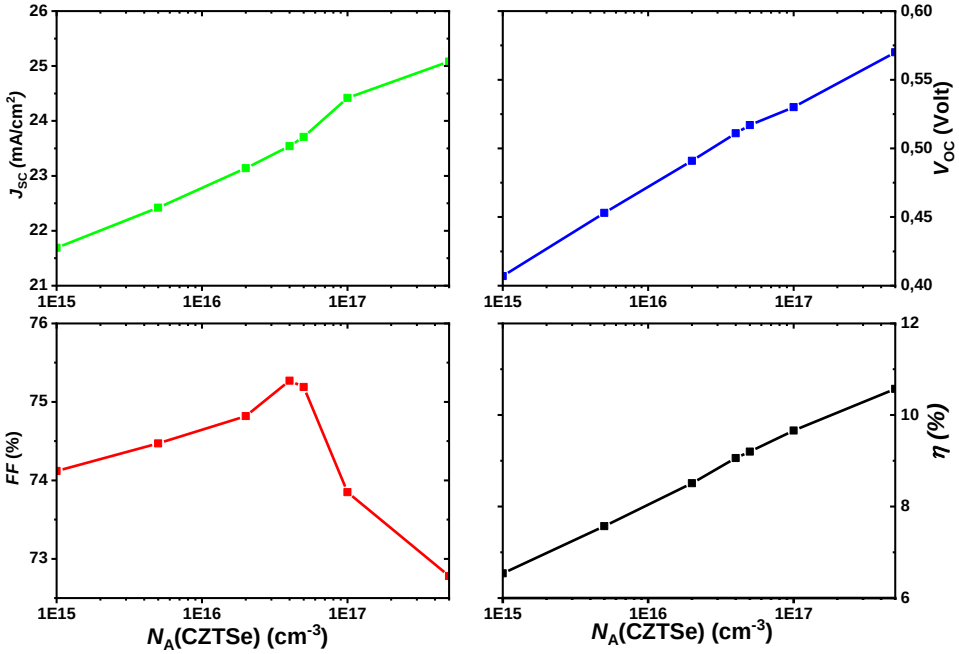

Fig. II.23: Effect of Absorber carrier concentration on CZTSe solar cell performance.

II.4.3.2 CZTS/CZTSe tandem cell performance optimization

Each cell should be adjusted to their maximum performances and then operated at a common current and individual voltages. The CZTS (1.52 eV) and CZTSe (1.0 eV) are attached in tandem sharing the same incident light spectrum. The higher band gap at the top will absorb the high energy photons (i.e. wavelength part low than 0.8 µm). The high wavelength part of spectrum (i.e. wavelength part high than 0.8 µm) will be transmitted from the top cell.

(a)

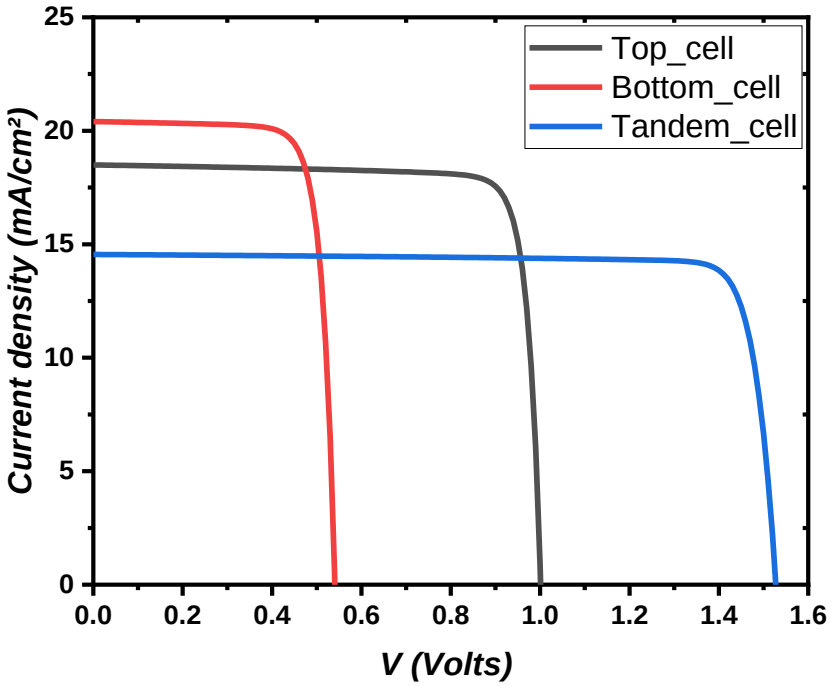

(b)

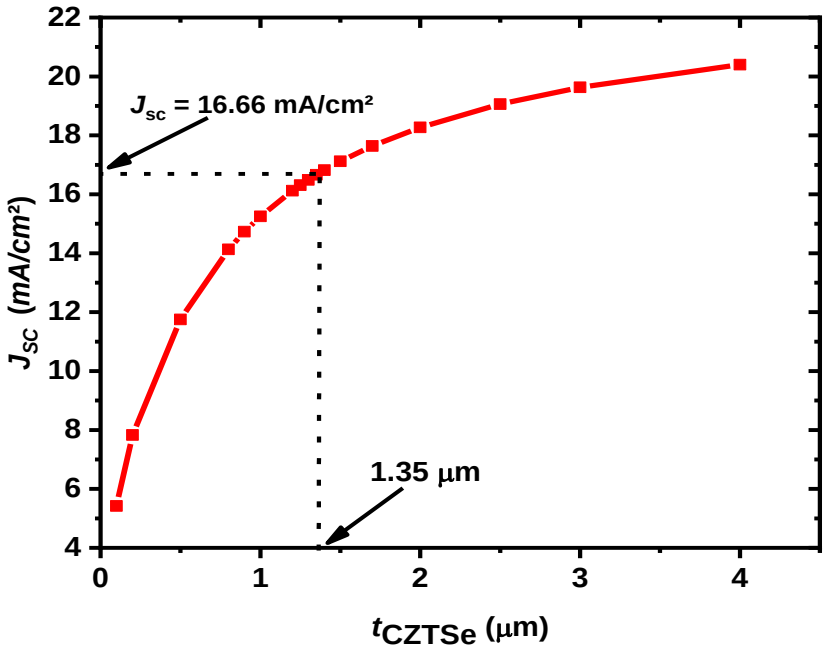

Fig. II.24: (a) J-V characteristic of CZTS/CZTSe tandem cell, CZTS single top-cell and CZTSe bottom-cell. (b) variation of J_{sc} of CZTSe bottom-cell in function of its absorber thickness t_{CZTSe}.

This transmitted part is the illumination for the bottom cell. The current densities in the optimized tandem cell must obey to [47]:

$$J_{\tan dom} = q \int_{0}^{1239.8/E_g(CZTS)} \Phi_{AM1.5}(\lambda)d\lambda = q \int_{1239.8/E_g(CZTSe)}^{1239.8/E_g(CZTS)} \Phi_{AM1.5}(\lambda)d\lambda \qquad \text{(II.10)}$$

In Fig. II.24(a) we can observe the current densities of the three solar cells (single top cell, single bottom cell and the full tandem cell). The court circuit currents are mismatched; the full tandem optimization consist in matching this the values.

From J(V) of the single CZTS solar cell, we get J_{CZTS} = 16.63 mA/cm² for t_{CZTS} = 3 µm, this must correspond to J_{sc} of the tandem cell, we observe that the J_{sc} of the bottom cell is the highest J_{sc} and must be reduced by reducing its thickness. From Fig. II.24(b) we can see the approximatively a bottom absorber thickness of 1.65 µm is sufficient to obtain 16.65 mA/cm². More accurate optimization in the thickness of top and bottom absorber must be done simultaneously to match the J_{sc} of the three cells.

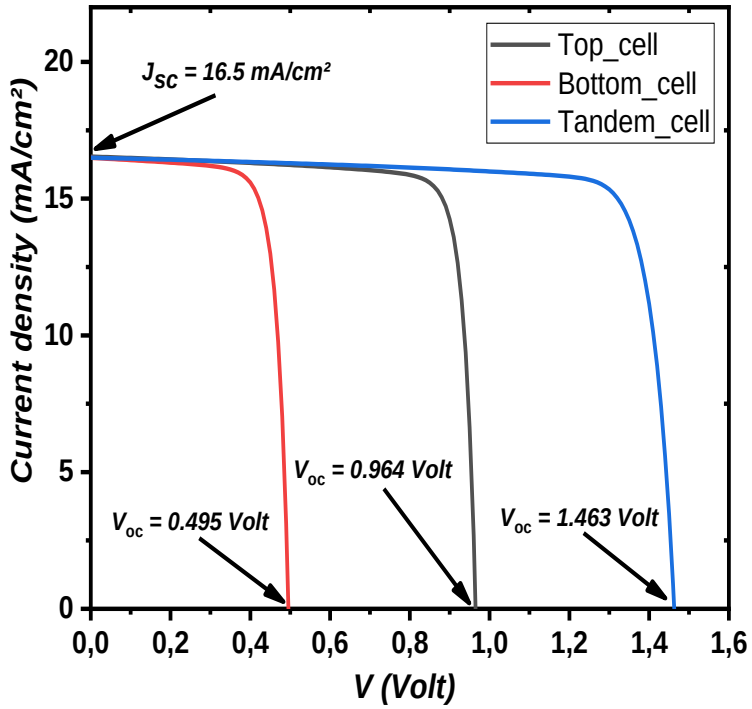

Fig. II.25: J-V characteristics of optimized CZTS/CZTSe tandem cell, CSTS single top-cell and CZTSe bottom cell at current matching point.

Fig. II.25 show the J-V of the current densities of the three solar cells (single top cell, single bottom cell and the full tandem cell) at the current matched condition (t_{CZTS} = 1.25 µm, t_{CZTSe} = 1.3 µm). A good performance is evident at the current matched condition (t_{CZTS}

= 1.25 µm, t_{CZTSe} = 1.3 µm), with η=19.94%, *FF*=82.62%, J_{SC}=16.5 mA/cm² and V_{oc} = 1.463 Volt for CZTS/CZTSe tandem cell, while V_{oc} = 0.964 Volt for the top cell and V_{oc} = 0.495 Volt for the bottom cell.

II.4.4 Bifacial CZTS/CZTSe tandem solar cell

The tandem CZTS/CZTSe ameliorate the conversion efficiency of the solar cell, while the development of interfacial MoS_2 layer as disputed in section II.4.1.5 degrade the efficiency. The idea is to replace the Mo back contact by a TCO materials like AZO (ZnO:Al) and ITO (In_2O_3:Sn) which give us two advantages: TCO are a good charge collectors and they guaranteed more than 80% of transparency.

Fig. II.26(a) presents bifacial configuration of CZTS/CZTSe tandem solar cell. The Molybdenum (Mo) back contact is replaced by AZO thin layer. We can observe in Fig. II.26(b) a proportional amelioration to the albedo factor in the current density. Under AM1.5G illumination spectrum (one sun) in front side, and 0.2 sun as a back illumination. The Bifacial-Tandem CZTS/CZTSe solar cell reaches a good photovoltaic parameter: J_{SC} = 18.09 mA/cm² with an efficiency η = 21.53%, while the V_{OC} remains unchanged.

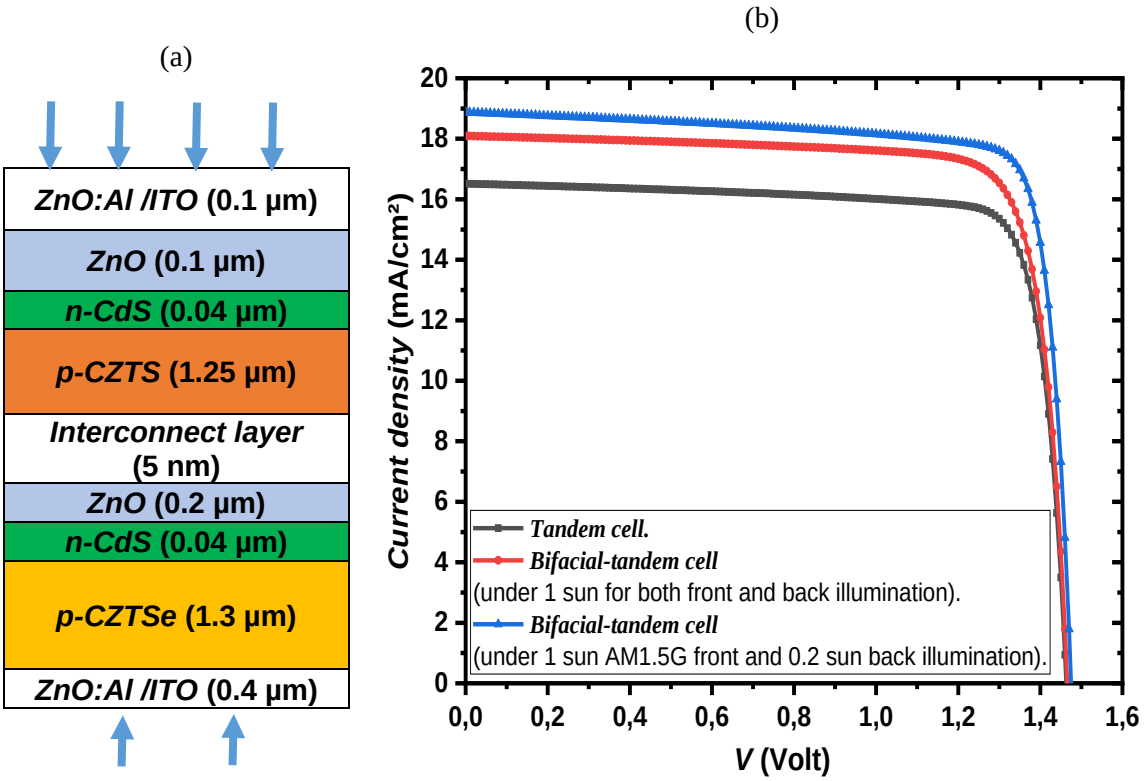

Fig. II.26: (a) Structure of Bifacial-Tandem CZTS/CZTSe solar cell, (b) *J-V* characteristics of Tandem and Bifacial-Tandem CZTS/CZTSe solar cells.

II.5 Conclusion

The efficacy of simulation tools such as AMPS-1D and Silvaco/Atlas TCAD was explored to analyze diverse CZTS solar cell structures. The optimization process revealed an ideal CZTS absorber thickness of 2-3 µm, coupled with a carrier concentration of 2×10^{16} cm^{-3} in the basic substrate structure. Additionally, the introduction of a Cd-free buffer material, such as Zn(O,S), demonstrated the potential to enhance the cell performance. The investigation further examined the impact of the barrier height in the p-CZTS/TCO interface within ZnO:Al/CdS/CZTS/TCO/SLG solar cells, considering both front and backside AM1.5G illuminations.

Finally, we will explore the real-world applications of Transparent Conductive Oxides (TCOs) as an intermediate layer in tandem CZTS/CZTSe solar cells. The optimal photovoltaic parameters derived from this study include η = 19.94%, FF = 82.62%, V_{OC} = 1.46 V, and J_{SC} = 16.5 mA/cm² for CZTS and CZTSe layers with thicknesses of 1.25 µm and 1.3 µm, respectively. These results not only hold significant promise for various optoelectronic applications but also suggest the potential for further enhancements in the performance of these solar cells.

References

[1] Paier, Joachim et al. "Cu_2ZnSnS_4as a Potential Photovoltaic Material: A Hybrid Hartree-Fock Density Functional Theory Study." Physical Review B, vol. 79, no. 11, 2009, doi:10.1103/PhysRevB.79.115126.

[2] Redinger, Alex et al. " $Cu_2ZnSnSe_4$ Thin Film Solar Cells Produced Via Co-Evaporation and Annealing Including a $SnSe_2$ Capping Layer." Progress in Photovoltaics: Research and Applications, vol. 22, no. 1, 2013, pp. 51-57, doi:10.1002/pip.2324.

[3] Dhakal, Tara P. et al. "Characterization of a CZTS Thin Film Solar Cell Grown by Sputtering Method." Solar Energy, vol. 100, 2014, pp. 23-30, doi:10.1016/j.solener.2013.11.035.–30.

[4] Wang, Wei et al. "Characterization and Photocatalytic Activity of Mesoporous TiO_2 Prepared from an Ethanol–Diethyl Ether Binary Solvent System." Chemical Physics Letters, vol. 616-617, 2014, pp. 1-5, doi:10.1016/j.cplett.2014.10.006.

[5] Jackson, Philip et al. "Properties of Cu(in,Ga)Se_2 Solar Cells with New Record Efficiencies up to 21.7%." physica status solidi (RRL) - Rapid Research Letters, vol. 9, no. 1, 2015, pp. 28-31, doi:10.1002/pssr.201409520.

[6] Mazzer, M. et al. "Bifacial CIGS Solar Cells Grown by Low Temperature Pulsed Electron Deposition." Solar Energy Materials and Solar Cells, vol. 166, 2017, pp. 247-253, doi:10.1016/j.solmat.2016.10.048.2003) 2880.

[7] Minami, Tadatsugu et al. "Work Function of Transparent Conducting Multicomponent Oxide Thin Films Prepared by Magnetron Sputtering." Surface and Coatings Technology, vol. 108-109, 1998, pp. 583-587, doi:10.1016/s0257-8972(98)00592-1.

[8] Ritzau, Kurt-Ulrich et al. "TCO Work Function Related Transport Losses at the a-Si:H/TCO-Contact in SHJ Solar Cells." Solar Energy Materials and Solar Cells, vol. 131, 2014, pp. 9-13, doi:10.1016/j.solmat.2014.06.026.

[9] Belfar, Abbas. "Simulation Study of the a-Si:H/Nc-Si:H Solar Cells Performance Sensitivity to the TCO Work Function, the Band Gap and the Thickness of I-a-Si:H Absorber Layer." Solar Energy, vol. 114, 2015, pp. 408-417, doi:10.1016/j.solener.2015.02.010.

[10] Calnan, S., & Tiwari, A. N. (2010). High mobility transparent conducting oxides for thin film solar cells. In Thin Solid Films, Vol. 518(7), pp. 1839–1849. https://doi.org/10.1016/j.tsf.2009.09.044

[11] Clugston, D. A., & Basore, P. A. (1997). Modelling Free-carrier Absorption in Solar Cells. Progress In Photovoltaics: Research and Applications, Vol. 5, pp. 229-236. 10.1002/(sici)1099-159x(199707/08)5:4%3C229::aid-pip164%3E3.0.co;2-6

[12] Larsson, F. Window Layer Structures for Chalcopyrite Thin-Film Solar Cells. 2020. Uppsala: Acta Universitatis Upsaliensis, PhD thesis. ISBN 978-91-513-0984-2.

[13] Keller, J., Lindahl, J., Edoff, M., Stolt, L., & Törndahl, T. (2016). Potential gain in photocurrent generation for $Cu(In,Ga)Se_2$ solar cells by using In_2O_3 as a transparent conductive oxide layer. Progress in Photovoltaics: Research and Applications, Vol. 24(1). pp.102–107. https://doi.org/10.1002/pip.2655

[14] Chavan, G. T. et al. "A Brief Review of Transparent Conducting Oxides (TCO): The Influence of Different Deposition Techniques on the Efficiency of Solar Cells." Nanomaterials (Basel), vol. 13, no. 7, 2023, doi:10.3390/nano13071226.

[15] Mursal et al. "Structural and Optical Properties of Zinc Oxide (ZnO) Based Thin Films Deposited by Sol-Gel Spin Coating Method." Journal of Physics: Conference Series, vol. 1116, 2018, doi:10.1088/1742-6596/1116/3/032020.

[16] Silvaco, Inc. (2020). ATLAS User's Manual, Device Simulation Software.

[17 Fonash, S. J. A manual for one-dimensional device simulation program (AMPS). Electron. Mater. Process. Res. Lab. Peensylvania State University.

[18] Zhang, Kezhi and Huafei Guo. "Effects of Annealing on Cu_2ZnSnS_4 Thin Films Prepared on Mo Substrate and the Fabrication of Solar Cells." Journal of Materials Science: Materials in Electronics, vol. 28, no. 22, 2017, pp. 17044-17048, doi:10.1007/s10854-017-7629-4.

[19] Tripathi, Swati et al. "Contribution to Sustainable and Environmental Friendly Non-Toxic CZTS Solar Cell with an Innovative Hybrid Buffer Layer." Solar Energy, vol. 204, 2020, pp. 748-760, doi:10.1016/j.solener.2020.05.033.

[20] Wangperawong, A. et al. "Aqueous Bath Process for Deposition of Cu_2ZnSnS_4 Photovoltaic Absorbers." Thin Solid Films, vol. 519, no. 8, 2011, pp. 2488-2492, doi:10.1016/j.tsf.2010.11.040.

[21] Mohammadnejad, Shahram and Ali Baghban Parashkouh. "CZTSSe Solar Cell Efficiency Improvement Using a New Band-Gap Grading Model in Absorber Layer." Applied Physics A, vol. 123, no. 12, 2017, doi:10.1007/s00339-017-1371-x.

[22] Mirzaei, Mina et al. "Significant Efficiency Enhancement in Ultrathin CZTS Solar Cells by Combining Al Plasmonic Nanostructures Array and Antireflective Coatings." Plasmonics, vol. 16, no. 4, 2021, pp. 1375-1390, doi:10.1007/s11468-021-01379-9.

[23] Gorji, Nima E. "Quantitative Analysis of the Optical Losses in CZTS Thin-Film Semiconductors." IEEE Transactions on Nanotechnology, vol. 13, no. 4, 2014, pp. 743-748, doi:10.1109/tnano.2014.2318057.

[24] Sravani, L. et al. "Loss Mechanisms in CZTS and CZTSe Kesterite Thin-Film Solar Cells: Understanding the Complexity of Defect Density." Solar Energy, vol. 227, 2021, pp. 56-66, doi:10.1016/j.solener.2021.08.052.

[25] Chen, Hao et al. "Electrodeposited CZTS Solar Cells from Reline Electrolyte." Green Chem., vol. 16, no. 8, 2014, pp. 3841-3845, doi:10.1039/c4gc00142g.

[26] Heriche, H. et al. "High-Efficiency CIGS Solar Cells with Optimization of Layers Thickness and Doping." Optik, vol. 127, no. 24, 2016, pp. 11751-11757, doi:10.1016/j.ijleo.2016.09.071.

[27] Severino, N. et al. "Buffer Layer Optimization for High Efficiency CIGS Solar Cells." Journal of Physics: Conference Series, vol. 758, 2016, doi:10.1088/1742-6596/758/1/012016.

[28] Enayati Maklavani, Shahin and Shahram Mohammadnejad. "The Impact of the Carrier Concentration and Recombination Current on the P+Pn CZTS Thin Film Solar Cells." Optical and Quantum Electronics, vol. 52, no. 6, 2020, doi:10.1007/s11082-020-02407-4.

[29] Sharbati, Samaneh et al. "Improvement of CIGS Thin-Film Solar Cell Performance by Optimization of Zn(O,S) Buffer Layer Parameters." Applied Physics A, vol. 118, no. 4, 2014, pp. 1259-1265, doi:10.1007/s00339-014-8825-1.

[30] Belarbi, F. et al. "A Comparative Study of Different Buffer Layers for CZTS Solar Cell Using Scaps-1d Simulation Program." Optik, vol. 216, 2020, doi:10.1016/j.ijleo.2020.164743.

[31] Shunji Ozaki, Shunji Ozaki and Sadao Adachi Sadao Adachi. "Optical Constants of Cubic ZnS." Japanese Journal of Applied Physics, vol. 32, no. 11R, 1993, doi:10.1143/jjap.32.5008.

[32] Zheng, Zhongming et al. "Investigation of Structural, Optical and Electrical Properties of Cu Doped B-In_2S_3 Thin Films." Journal of Materials Science: Materials in Electronics, vol. 27, no. 6, 2016, pp. 5810-5817, doi:10.1007/s10854-016-4496-3.

[33] Ermolaev, G. A. et al. "Broadband Optical Constants and Nonlinear Properties of SnS(2) and SnSe(2)." Nanomaterials (Basel), vol. 12, no. 1, 2021, doi:10.3390/nano12010141.

[34] Çetinkaya, Samed. "Study of Electrical Effect of Transition-Metal Dichalcogenide-Mos2 Layer on the Performance Characteristic of Cu2znsns4 Based Solar Cells Using Wxamps." Optik, vol. 181, 2019, pp. 627-638, doi:10.1016/j.ijleo.2018.12.122.

[35] Islam, Kazi M. et al. "In-Plane and out-of-Plane Optical Properties of Monolayer, Few-Layer, and Thin-Film Mos2 from 190 to 1700 Nm and Their Application in Photonic Device Design." Advanced Photonics Research, vol. 2, no. 5, 2021, doi:10.1002/adpr.202000180.

[36] Lu, X. et al. "Modification of Back Contact in Cu(2)ZnSnS(4) Solar Cell by Inserting Al-Doped ZnO Intermediate Layer." ACS Appl Mater Interfaces, vol. 12, no. 52, 2020, pp. 58060-58071, doi:10.1021/acsami.0c18799.

[37] Yuan, Tengfei et al. "Fabrication of Cu2ZnSnS4 Thin Film Solar Cells by Sulfurization of Electrodeposited Stacked Binary Cu–Zn and Cu–Sn Alloy Layers." Materials Letters, vol. 155, 2015, pp. 44-47, doi:10.1016/j.matlet.2015.04.101.

[38] Liu, Fangyang et al. "Enhancing the Cu_2ZnSnS_4 Solar Cell Efficiency by Back Contact Modification: Inserting a Thin Tib2 Intermediate Layer at Cu_2ZnSnS_4/Mo Interface." Applied Physics Letters, vol. 104, no. 5, 2014, doi:10.1063/1.4863736.

[39] Patel, Malkeshkumar and Abhijit Ray. "Enhancement of Output Performance of Cu_2ZnSnS_4 Thin Film Solar Cells—a Numerical Simulation Approach and Comparison to Experiments." Physica B: Condensed Matter, vol. 407, no. 21, 2012, pp. 4391-4397, doi:10.1016/j.physb.2012.07.042.

[40] Minami, Tadatsugu et al. "Work Function of Transparent Conducting Multicomponent Oxide Thin Films Prepared by Magnetron Sputtering." Surface and Coatings Technology, vol. 108-109, 1998, pp. 583-587, doi:10.1016/s0257-8972(98)00592-1.

[41] Marsillac, S. et al. "Ultra-Thin Bifacial Cdte Solar Cell." Solar Energy Materials and Solar Cells, vol. 91, no. 15-16, 2007, pp. 1398-1402, doi:10.1016/j.solmat.2007.04.025.

[42] Yan, Zhiqiang et al. "Growth of Cu2znsns4 Thin Films on Transparent Conducting Glass Substrates by the Solvothermal Method." Materials Letters, vol. 111, 2013, pp. 120-122, doi:10.1016/j.matlet.2013.08.067.

[43] Wei, Aixiang et al. "Solvothermal Synthesis of Cu2znsns4 Nanocrystalline Thin Films for Application of Solar Cells." International Journal of Hydrogen Energy, vol. 40, no. 1, 2015, pp. 797-805, doi:10.1016/j.ijhydene.2014.09.047.

[44] Green, Martin A. et al. "Solar Cell Efficiency Tables (Version 63)." Progress in Photovoltaics: Research and Applications, vol. 32, no. 1, 2023, pp. 3-13, doi:10.1002/pip.3750.

[45] Hirate, Yoshiki et al. "Dielectric Functions of $Cu_2ZnSnSe_4$ and Cu_2SnSe_3 Semiconductors." Journal of Applied Physics, vol. 117, no. 1, 2015, doi:10.1063/1.4905285.

[46] Amiri, Samaneh and Sajjad Dehghani. "Design of Highly Efficient CZTS/ CZTSe Tandem Solar Cells." Journal of Electronic Materials, vol. 49, no. 3, 2020, pp. 2164-2172, doi:10.1007/s11664-019-07898-w.

[47] Kumar, Atul. "Theoretical Analysis of CZTS/ CZTSSe Tandem Solar Cell." Optical and Quantum Electronics, vol. 53, no. 9, 2021, doi:10.1007/s11082-021-03183-5.

Chapter III: Study of $ZnS_{1-x}O_x$ material using Wien2k package

Chapter III

Study of $ZnS_{1-x}O_x$ material using WIEN2k package

III.1 Introduction

Group II-VI semiconductors possess an expansive direct band gap, making them attractive materials with specific attributes that elude Group III-V compounds. The recent reduction in manufacturing costs for II-VI semiconductors has heightened the significance of their optoelectronic properties for certain applications. Ternary alloys, comprising elements from subgroup IIb and group VI, stand out as excellent infrared window materials [1]. The binary compounds ZnS and ZnO confine the $ZnS_{1-x}O_x$ alloy, capable of adopting zinc blend and wurtzite phases. The variable *x* represents the concentration of Oxygen in the alloy, ranging from 0 to 1. This alloy, investigated for applications such as light emission in photovoltaics solar cells [2]. Undergoes a theoretical analysis of elastic and optical properties in the zinc blend structure using the full potential linearized augmented plane wave method [3].

The ternary alloy $ZnS_{1-x}O_x$ demonstrates advantageous optical and electronic characteristics, encompassing band gap and the absorption coefficient. This positions it as a promising absorber material for solar cells within the photovoltaic domain. However, Zinc Oxide (ZnO) can undergo substantial doping to attain a high carrier concentration [4]. Paired with its sizable band gap, this property facilitates the transmission of visible light, establishing ZnO as a promising material for transparent conducting oxides (TCO).

Over the past few decades, computational science has made significant strides. On one front, computer hardware is advancing in both capability and affordability. Simultaneously, the advent of parallel programming allows the utilization of multiple computer nodes for extensive calculations. These advancements in hardware and software collectively enhance the capacity for precise calculations [5]. In the realm of materials science research, computational studies are assuming increasing importance. Computational materials science offers an avenue to predict material properties with both high precision and cost-effectiveness. Through simulations at the atomic scale, it not only facilitates an understanding of the physics underpinning experimental phenomena but also plays a crucial role in the discovery of new materials and fundamental insights into material behavior.

A phenomenally successful method in this domain is density functional theory (DFT), employed to find solutions to the fundamental equation governing the quantum behavior of atoms and molecules—the Schrödinger equation—in practical settings. This approach has experienced rapid growth and is regularly employed by numerous researchers across various scientific disciplines. By introducing several approximations to Schrödinger's Equation, DFT enables the extraction of electronic and optical properties for a given system.

In this chapter, we explore the impact of varying oxygen concentrations on the structural, electronic, and optical characteristics of the $ZnS_{1-x}O_x$ alloy within the wurtzite crystal structure. Employing the full-potential linearized augmented plane wave (FP-LAPW) method within the density functional theory (DFT) framework, as implemented in the Wien2k computer package, we conduct computational analyses. The chapter commences with a concise overview of the theory behind first principles calculations, followed by a detailed explanation of the primary steps and subprograms utilized in the Wien2k package. Finally, we delve into an investigation of the structural, electronic, and optical properties of the $ZnS_{1-x}O_x$ alloy.

III.2 Theory for first principles calculations

III.2.1 The Schrodinger equation

Deciphering the electronic configuration of a substance involves addressing the intricate interplay among numerous electrons as they interact with each other and with the atomic nuclei. Unfortunately, finding precise solutions to this predicament becomes impractical for systems more intricate than the basic hydrogen atom. The foundational principle of quantum mechanics asserts that the state and all measurable characteristics of a quantum system are fundamentally dictated by its wave function Ψ. This function can be derived by solving the generalized Schrödinger equation (III.1):

$$\hat{H}\Psi = E\Psi \tag{III.1}$$

Where $\hat{H}$ is the total Hamiltonian of the system. ψ is the wavefunction to be determined, and E is the energy eigenvalue of the eigenstate. M and m are the nucleus and electron mass, respectively. Z is the nuclear charge. $\vec{R}$ and $\vec{r}$ are the nucleus and electron position vectors, respectively, the full many-bodied Hamiltonian can be written as (in Hartree atomic units):

$$\hat{H} = -\frac{1}{2}\sum_i \frac{\nabla^2}{M_i} - \frac{1}{2}\sum_i \frac{\nabla^2}{m_i} - \sum_{i,j} \frac{Z_i}{\left|\vec{R}_i - \vec{r}_j\right|} + \frac{1}{2}\sum_{i,j} \frac{Z_i}{\left|\vec{r}_i - \vec{r}_j\right|} - \frac{1}{2}\sum_{i,j} \frac{Z_i Z_j}{\left|\vec{R}_i - \vec{R}_j\right|} \quad \text{(III.2)}$$

where:

$-\frac{1}{2}\sum_i \frac{\nabla^2}{M_i}$ represent the kinetic energies of the nuclei,

$-\frac{1}{2}\sum_i \frac{\nabla^2}{m_i}$ represent the kinetic energies of the electron,

$-\sum_{i,j} \frac{Z_i}{\left|\vec{R}_i - \vec{r}_j\right|}$ represent the nuclei - electron attraction,

$\frac{1}{2}\sum_{i,j} \frac{Z_i}{\left|\vec{r}_i - \vec{r}_j\right|}$ represent the electron - electron repulsion,

$-\frac{1}{2}\sum_{i,j} \frac{Z_i Z_j}{\left|\vec{R}_i - \vec{R}_j\right|}$ represent the nuclei-nuclei repulsion.

In practice, the potential experienced by each electron is influenced by the motion not only of its nearest neighbors but also by the entire assembly of other electrons in the real system. This would require solving a Schrödinger equation with approximately 10^{23} simultaneous differential equations. Generally, it is not feasible to solve this equation directly, and resorting to approximations becomes necessary.

III.2.2 Basic approximations (Born-Oppenheimer, Hartree and Hartree-Fock)

The initial approximation is the Born-Oppenheimer approximation, which involves separating the electron and nuclei terms. This separation is founded on the premise that atoms and molecules comprise heavy nuclei and lightweight electrons. Consequently, the nuclei can be treated as quasi-static charges relative to the electrons, possessing negligible kinetic energy and resulting in a constant potential energy of interaction between the nuclei. This method gives rise to a Hamiltonian, wherein electrons navigate within a field generated by a static arrangement of nuclei. Consequently, the electronic Hamiltonian can be characterized as:

$$\hat{H}_e = T_e + V_e + V_{ext} \quad \text{(III.3)}$$

where T_e is the kinetic energy of electrons. *V*e is the interaction potential between one electron and the other electrons, and V_{ext} is the external potential due to the nuclei [6].

The problem of solving the Schrödinger equation is reduced to the behavior of electrons. However, it still remains highly complex due to electron-electron interactions. For further simplification, Hartree [7] proposes substituting the system of (*N*) interacting electrons with a system of (*N*) independent electrons. As a result, the wave function for (N) electrons is reduced to a product of (*N*) single-electron wave function Ψ_i.

$$\Psi(\vec{r}) = \prod_i \Psi_i(\vec{r_i}) \tag{III.4}$$

The Hamiltonian is then defined as the sum of the Hamiltonians H_i (where each H_i describes the behavior of a single electron):

$$H = \sum_i H_i \tag{III.5}$$

The Pauli exclusion principle (which follows from the Heisenberg uncertainty principle, stating that any wave function for a given system must be antisymmetric with respect to the exchange of two particles) is no longer adhered to by the Hartree method. The extension of Hartree-Fock [8] proposes to incorporate the permutation symmetry of wave functions, leading to exchange interaction. The wave function of a system with (*N*) electrons is expressed in the general form of a Slater determinant:

$$\Psi(\vec{r_1},\vec{r_2},...,\vec{r_N}) = \frac{1}{\sqrt{N!}}\begin{vmatrix} \Psi_1(\vec{r_1}) & \Psi_2(\vec{r_1}) & ... & \Psi_N(\vec{r_1}) \\ \Psi_1(\vec{r_2}) & \Psi_2(\vec{r_2}) & ... & \Psi_N(\vec{r_2}) \\ \vdots & \vdots & & \vdots \\ \Psi_1(\vec{r_N}) & \Psi_1(\vec{r_N}) & ... & \Psi_N(\vec{r_N}) \end{vmatrix} \tag{III.6}$$

where $\frac{1}{\sqrt{N!}}$ is normalization factor.

The exchange term introduced by the Hartree-Fock approximation increases the complexity of calculations required for systems beyond small molecular assemblies.

III.2.3 Density functional theory

Density Functional Theory (DFT) was developed as a computationally efficient alternative to the Hartree-Fock method. The central concept of DFT involves describing a many-electron system using the one-body density ρ(r) as the fundamental variable, replacing the many-body wave function Ψ. This approach is rooted in the postulate introduced by

Tomas [9] and Fermi [10] in 1927, where they endeavored to express the total energy of a system as a function of its electronic density, representing its kinetic energy through a functional of this quantity. In 1930, Dirac [11] expanded the Thomas and Fermi model by incorporating a functional exchange energy of the electronic density. The foundational theorems of DFT were formulated by Hohenberg, Kohn, and Sham in 1964.

III.2.3.1 Hohenberg - Kohn and Kohn - Sham theorems

Theorem I:

In a system of interacting particles subject to an external potential $V_{ext}(r)$, the ground state particle density $\rho(r)$ uniquely establishes the external potential $V_{ext}(r)$, with the exception of a constant offset. Consequently, the ground state particle density completely dictates the entire Hamiltonian, except for a constant energy shift. This implies that both the external potential $V_{ext}(r)$ and the resulting total energy E_{Total} are functionals of the electron density ρ(r).

Theorem II:

If a trial function $\rho(r)$ satisfies the specified boundary conditions ($\rho(r) \geq 0$ and $\int d^3r = N$) linked to an external potential V_{ext}, the energy it yields serves as an upper bound to the actual energy E_0. This implies that only the ground state density corresponds to the minimum energy of the system. In other words, any other energies associated with random densities in the system will be greater than the energy obtained with the ground-state density:

$$E(\rho_0) \geq \min[E(\rho)] \tag{III.8}$$

The total ground-state energy $E(\rho)$ is a functional of the ground-state density $\rho(r)$ and is of the form:

$$E(\rho) = F[\rho] + \int \rho(\vec{r}) V_{ext}(\vec{r}) d\vec{r} \tag{III.9}$$

where $F[\rho]$ is a functional independent of any information about the nuclei and is therefore universal for any many-electron system.

While these two theorems establish particle density as the fundamental variable, the challenge lies in the inability to calculate any system property due to the unknown universal functional. Kohn and Sham successfully addressed this difficulty in 1965.

III.2.3.2 Kohn-Sham equations

According to the Hohenberg–Kohn Theorems, to obtain the total energy, the initial step involves determining the ground state density of the system. However, the relationship between density and energy remains unknown. In 1965, Kohn and Sham [12] proposed a method based on the one-electron Schrödinger equation to ascertain the density ρ, which involves self-consistent equations incorporating exchange and correlation effects. This method maps the original interacting system with a real potential onto an effective external potential, within which the particles are treated as non-interacting.

The universal functional can be decomposed into three terms:

$$F(\rho) = T + V_H + V_{XC} \tag{III.10}$$

where:

- The kinetic energy: $T(\rho) = -\frac{1}{2}\sum_{i=1}^{N} \varphi_i^*(r)\nabla^2\varphi_i(r)dr$

- $V_H = \int \frac{\rho(r')}{|r-r'|}dr'$ is Hartree potential due to the classical Coulombic interaction between the electrons.

- $V_{XC} = \frac{\delta E_{XC}(\rho(r))}{\delta\rho(r)}$ represents the exchange-correlation potential. The exchange-correlation term encompasses the disparity between the precise and non-interacting kinetic energies, as well as the non-classical effects arising from exchange and correlation.

The effective external potential $V_{KS}(r)$ expression can be written as:

$$V_{KS}(r) = V_{ext}(r) + V_H(r) + V_{XC}(r) \tag{III.11}$$

For the auxiliary independent-particle system, the auxiliary Hamiltonian (in Hartree atomic units) is:

$$H_{ks}(\rho) = -\frac{1}{2}\nabla^2 + V_{KS}(r) \tag{III.12}$$

So, once H_{KS} is known the ground state can be obtained by solving the N one-electron Schrodinger equations, as:

$$(-\frac{1}{2}\nabla^2 + V_{KS}(r))\varphi_i(r) = \varepsilon_i\varphi_i(r) \quad \text{(III.13)}$$

here $\varphi_i(r)$ is Kohn-Sham orbital function; and the value ε_i is the eigenvalue of corresponding Kohn–Sham orbital, representing the energy of that orbital, Achieving self-consistency between the orbitals and the density is essential, this is accomplished by utilizing the orbitals to construct the new density to which they correspond, as expressed by the equation:

$$\rho(r) = \sum_{i=1}^{N} |\varphi_i(r)|^2 \quad \text{(III.14)}$$

In principle, the Kohn-Sham theory is exact, and the electronic structure of most materials could be precisely solved if the exchange-correlation term were precisely known. A reliable approximation of this term results in an accurate and efficient method. The local density approximation (LDA) and the generalized-gradient approximation (GGA) are among the most widely used approximations for the exchange-correlation potential.

III.2.3.3 Approximations for the exchange–correlation energy

a) Local Density Approximation (LDA)

The fundamental among all functionals is the local density approximation (LDA), introduced by Hohenberg and Kohn [12]. It has continued to be the preferred approximation for many years following the development of the Kohn-Sham theorem. In LDA, the exchange-correlation (XC) energy density is approximated to be that of a homogeneous electron gas with the same density as the actual nonhomogeneous system. It is expressed as:

$$E_{xc}^{LDA}(\rho(r)) = \int \rho(r)\varepsilon_{xc}(\rho(r))dr \quad \text{(III.15)}$$

where $\varepsilon_{xc}(\rho(r))$ is the exchange-correlation energy of each particle.

The exchange-correlation potential V_{xc}^{LDA} expression can be written as:

$$V_{xc}^{LDA}(\rho(r)) = \varepsilon_{xc}(\rho(r)) + \rho(r)\frac{\delta\varepsilon_{xc}}{\delta\rho} \quad \text{(III.16)}$$

Additionally, to better understand, it can be separated into two parts: exchange term E_x and correlation term E_c, respectively. While the exchange energy, also called “Dirac exchange” is well known and can be expressed as:

$$E_x^{LDA}(\rho(r)) = \frac{3}{4}\left(\frac{3}{\pi}\right)^{\frac{1}{3}} \int \rho(r)^{\frac{4}{3}} dr \qquad \text{(III.17)}$$

However, for the correlation term E_c no explicit equation has been proposed till now. Several different parameterizations have been proposed since the early 1970s [13-17].

b) Generalized Gradient Approximation (GGA)

The exchange-correlation within an infinitesimal volume arises from the local density within that volume and its neighboring volumes. Therefore, in the context of the generalized gradient approximation (GGA), the exchange-correlation energy E_{xc}^{GGA} is expressed as a function of both the electronic density and its gradient:

$$E_{xc}^{GGA}(\rho(r)) = \int \rho(r)\varepsilon_{xc}(\rho(r), \nabla\rho(r))dr \qquad \text{(III.18)}$$

This marks a departure from the traditional local density approximation (LDA). In recent years, further advancements within the realm of GGA have given rise to a new category known as "meta-GGA" functionals. These functionals, extending the principles of GGA, incorporate not only the electronic density and its first gradient but also involve the kinetic energy density of the Kohn–Sham orbitals [18].

Similar to LDA, various parameterizations have been proposed. Among the available functionals, including WC (Wu-Cohen) [19] and EV (Engel Vosko) [20], the PBE functional by Perdew, Burke, and Ernzerhof [21] currently holds prominence in solid-state physics. These non-empirical methods are valued for their simplicity and accuracy, with the utilization of GGA notably enhancing calculation precision compared to LDA [22].

III.3 Software packages based on DFT

Numerous DFT-based packages are widely employed [23], and in this study, we opt for the Wien2k package, developed by Peter Blaha and Karlheinz Schwarz [24] at Vienna University of Technology (Austria). The Wien2k package employs the Full Potential-Linearized Augmented Plane Wave method (FP-LAPW) and comprises various standalone programs interconnected through C-SHELL SCRIPTS.

Under a Linux environment, the Wien2k package can be accessed through either a web user interface (w2web) or a command-line terminal. The utilization of the Wien2k package involves three primary steps:

1- Initialize Wien2k calculation:

The studied case has to be set up (creation of the "case.struct" file) by giving the initial physics parameters:

- The lattice parameters (a,b,c) in Angstroms or in Bohr and angles (α,β,γ) in degrees;
- The space group (P, F, B …) and the atoms and the inequivalent positions.

Once the basic input file is established, initializing the calculation initiates several automated steps:

- x nn: Calculates the nearest neighbors up to a specified distance.
- view TiC.outputnn: Checks for overlapping spheres, coordination numbers, nearest neighbor distances, and angles.
- x sgroup: Computes the space groups for the structure.
- x symmetry: generates space group symmetry operations based on information from a raw "case.struct" file, identifies the point group associated with individual atomic sites, and produces the LM expansion for lattice harmonics along with local rotation matrices.
- x lstart: initiates the generation of atomic densities and dictates the treatment of orbitals in band structure calculations. Users must specify both the desired exchange correlation potential and an energy threshold that distinguishes valence from core states.
- x kgen: produces a k-mesh within the Brillouin zone (BZ). Users are required to indicate the number of k-points across the entire BZ for this process.
- x dstart: creates an initial density for the self-consistent field (SCF) cycle by combining atomic densities generated during the "x lstart" process

Alternatively, w2web offers a "Fast-mode," the recommended default, allowing users to specify the desired precision or key inputs right at the beginning. In this mode, the entire initialization process runs in one go. The initialization of a calculation generates all inputs for the subsequent self-consistent field (SCF) calculation, employing default options and values.

2- Self consistent calculation:

The Self-Consistent Field (SCF) cycle comprises the following stages:

- LAPW0: Generates potential based on density.

- LAPW1: Computes valence bands, including eigenvalues and eigenvectors.
- LAPW2: Calculates valence densities using eigenvectors.
- LCORE: Computes core states and densities.
- MIXER: Blends input and output densities.

3- Properties calculation

Upon achieving convergence in the Self-Consistent Field (SCF) cycle, it becomes possible to compute diverse properties such as Density of States (DOS), band structure, optical properties, or X-ray spectra.

III.4 Effect of Oxygen content on the properties of $ZnS_{1-x}O_x$ alloy using mBJ-GGA approximations

III.4.1 Computational details

The computations were conducted utilizing the full-potential linearized augmented plane wave (FP LAPW) method within the Wien2k computer package. In our structural analysis, we employed the GGA-PBESOL [25] approach. For handling the exchange-correlation effects in electronic properties, we utilized the Tran-Blaha modified Beck-Johnson (TB-mBJ) potential [26]. The TB-mBJ potential has gained significant attention due to its remarkably accurate band gap predictions for many semiconductors and insulators, especially for compounds containing d or f bands [27]. To ensure precision, a K-points test was performed, revealing optimal convergence within 0.1 meV with 1000 K-points spanning the entire Brillouin zone for each concentration (x). This was achieved using a 9 × 9 × 10 grid. The calculations were executed on 2 × 2 × 1 supercells, each containing 16 atoms. The wave function was expanded in the interstitial sites with a k cut-off (k_{max}) set at 7.0/RMT, where RMT represents the smallest atomic sphere radius (muffin-tin radius), and k_{max} denotes the magnitude of the largest k-vector. Valence wave functions were extended within the muffin-tin sphere, and the charge density up to l_{max} = 10, with a Gaussian parameter G_{max} = 14. The muffin-tin radii were assigned values of 1.7, 1.75, and 1.8 for O, S, and Zn atoms.

III.4.2 Results and discussions

III.4.2.1 Structure and lattice parameters

The investigation of the $ZnS_{1-x}O_x$ ternary alloy is conducted within the wurtzite structure, where the parameter x varies in the range of 0 to 1 with an increment of 0.125. The X, Y, Z coordinates for atomic species are detailed in Table III.1.

The graphs in Fig. III.1(a)–(*i*) illustrate the total energy versus volume curves for the zinc-Wurtzite $ZnS_{1-x}O_x$ system, which is under investigation for various compositions (*x* in the range of 0 to 1). A self-consistent calculation of the total energy is conducted using the GGA-PBESOL approximation, considering various lattice parameters for *a* and *c/a* in proximity to the experimental parameter of the primitive cell. The equilibrium lattice parameters (*a*, *c*), zero-pressure bulk modulus (B_0), its pressure derivative ($B_0^{'}$), and the ground state energy (E_0) are determined by fitting the total energy against the reduced and extended volume of the unit cell. This fitting is achieved through the third-order Birch-Murnaghan equation of state (EOS) [28].

In the third-order Birch-Murnaghan EOS, the total energy (E) and pressure (P) as functions of volume are expressed as follows:

$$E(V) = E_0 + \frac{9V_0B_0}{16}\left\{\left[\left(\frac{V_0}{V}\right)^{2/3} - 1\right]^3 B_0^{'} + \left[\left(\frac{V_0}{V}\right)^{2/3} - 1\right]^2 \times \left[6 - 4\left(\frac{V_0}{V}\right)^{2/3} - 1\right]^3\right\} \quad \text{(III.19)}$$

$$P(V) = \frac{3B_0}{2}\left[\left(\frac{V_0}{V}\right)^{7/3} - \left(\frac{V_0}{V}\right)^{5/3}\right]^3 \times \left\{1 + \frac{3}{4}\left(B_0^{'} - 4\right)\left[\left(\frac{V_0}{V}\right)^{2/3} - 1\right]^3\right\} \quad \text{(III.20)}$$

We derive the precise form factor results for the $ZnS_{1-x}O_x$ ternary alloy, examining its relationship with the form factors of the respective binary compounds ZnO and ZnS.

$$W_{ZnS_{1-x}O_x}(x) = xW_{ZnO} + (1-x)W_{ZnS} \quad \text{(III.21)}$$

The bulk modulus of the ternary $ZnS_{1-x}O_x$ alloy can be determined by applying Vegard's law [29], relating it to the bulk modulus of the binary compounds ZnO and ZnS.

$$B_{ZnS_{1-x}O_x}(x) = xB_{ZnO} + (1-x)B_{ZnS} \quad \text{(III.22)}$$

Table III.1: Atomic species X, Y, Z coordinates for *x* values of 0,0.125,0.5 and 1.

X	Atom	X	Y	Z
ZnS	Zn1	0.66666667	0.33333333	0
		0.33333334	0.66666667	0.5
	S	0.66666667	0.33333333	0.375
		0.33333334	0.66666667	0.875
ZnO	Zn1	0.33333333	0.66666667	0
		0.66666666	0.33333333	0.5
	O	0.33333333	0.66666667	0.3821
		0.66666666	0.33333333	0.8821
$ZnS_{0.875}O_{0.125}$	Zn1	0.16666666	0.33333334	0
	Zn2	0.33333333	0.16666666	0.5
		0.83333333	0.16666666	0.5
		0.33333333	0.66666666	0.5
	Zn3	0.66666666	0.33333334	0
		0.16666666	0.83333334	0
		0.66666666	0.83333334	0
	Zn4	0.83333333	0.66666666	0.5
	S5	0.16666666	0.33333334	0.3821
	S6	0.33333333	0.16666666	0.8821
		0.83333333	0.16666666	0.8821
		0.33333333	0.66666666	0.8821
	S7	0.66666666	0.33333334	0.3821
		0.16666666	0.83333334	0.3821
		0.66666666	0.83333334	0.3821
	O8	0.83333333	0.66666666	0.8821
$ZnS_{0.5}O_{0.5}$	Zn1	0.16666666	0.33333334	0
		0.33333333	0.16666666	0.5
	Zn2	0.66666666	0.33333334	0
		0.83333333	0.16666666	0.50
	Zn3	0.16666666	0.83333334	0
		0.33333333	0.66666666	0.5
	Zn4	0.66666666	0.83333334	0
		0.83333333	0.66666666	0.5
	S5	0.16666666	0.33333334	0.3821
		0.33333333	0.16666666	0.8821
	S6	0.66666666	0.33333334	0.3821
		0.83333333	0.16666666	0.8821
	O7	0.16666666	0.83333334	0.3821
		0.33333333	0.66666666	0.8821
	O8	0.66666666	0.83333334	0.3821
		0.83333333	0.66666666	0.8821

Table III.2 and Table III.3 present the lattice parameters (a and c), bulk modulus (B), and its pressure derivative (*B*') for different oxygen content values (*x*). Our findings for the binary compounds ZnS and ZnO are juxtaposed with existing theoretical [30-32] and experimental [33-35] data from the literature, revealing favorable agreement.

Table III.2: The lattice parameters of the $ZnS_{1-x}O_x$ alloy.

x	***a* (Å)**			***c* (Å)**		
	T.W.	Oth	Exp.	T.W.	Oth	Exp.
0	3.2815	3.281 [31]	3.2501 [33]	5.2553	5.256 [31]	5.2071 [33]
0.125	3.3744	-	-	5.4041	-	-
0.25	3.4815	-	-	5.5755	-	-
0.375	3.5463	-	-	5.6793	-	-
0.5	3.6001	-	-	5.7654	-	-
0.625	3.635	-	-	5.8214	-	-
0.75	3.7605	-	-	6.0223	-	-
0.875	3.8005	-	-	6.0863	-	-
1	3.8487	4.05 [30]	3.68 [34]	6.2954	6.14 [32]	6.252 [35]

Table III.3: The bulk modulus and its pressure derivative for the $ZnS_{1-x}O_x$ alloy.

x	**B (GPa)**			**B'**		
	T.W.	Oth	Exp.	T.W.	Oth	Exp.
0	127.51	133.7 [36]	142.7 [37]	4.32	4.05 [30]	3.6 [37]
0.125	115.25	-	-	4.39	-	-
0.25	102.87	-	-	4.55	-	-
0.375	93.1	-	-	4.51	-	-
0.5	85.89	-	-	4.49	-	-
0.625	80.36	-	-	4.47	-	-
0.75	75.5	-	-	4.48	-	-
0.875	73.22	-	-	4.38	-	-
1	69.63	88 [37]	80.1 [36]	4.41	4.4 [32]	4.41 [38]

In Fig. III.1, we illustrate the influence of unit cell volume on energy for $ZnS_{1-x}O_x$. It is noteworthy that the stability of the ternary alloy increases as the oxygen content (*x*) rises.

We show in Fig III.1 the impact of unit cell volume on energy for $ZnS_{1-x}O_x$. It is noted that the ternary alloy becomes more stable with the increase in the oxygen content *x*.

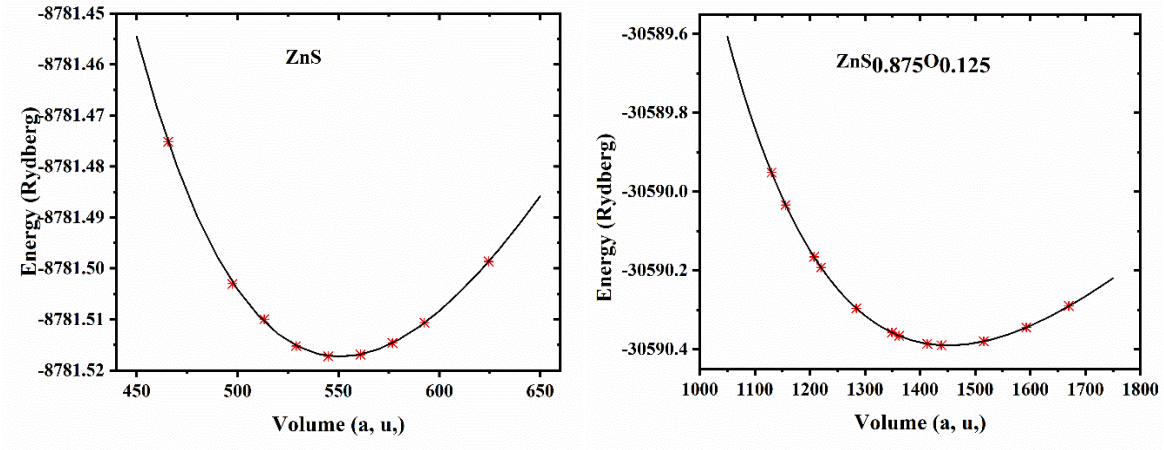

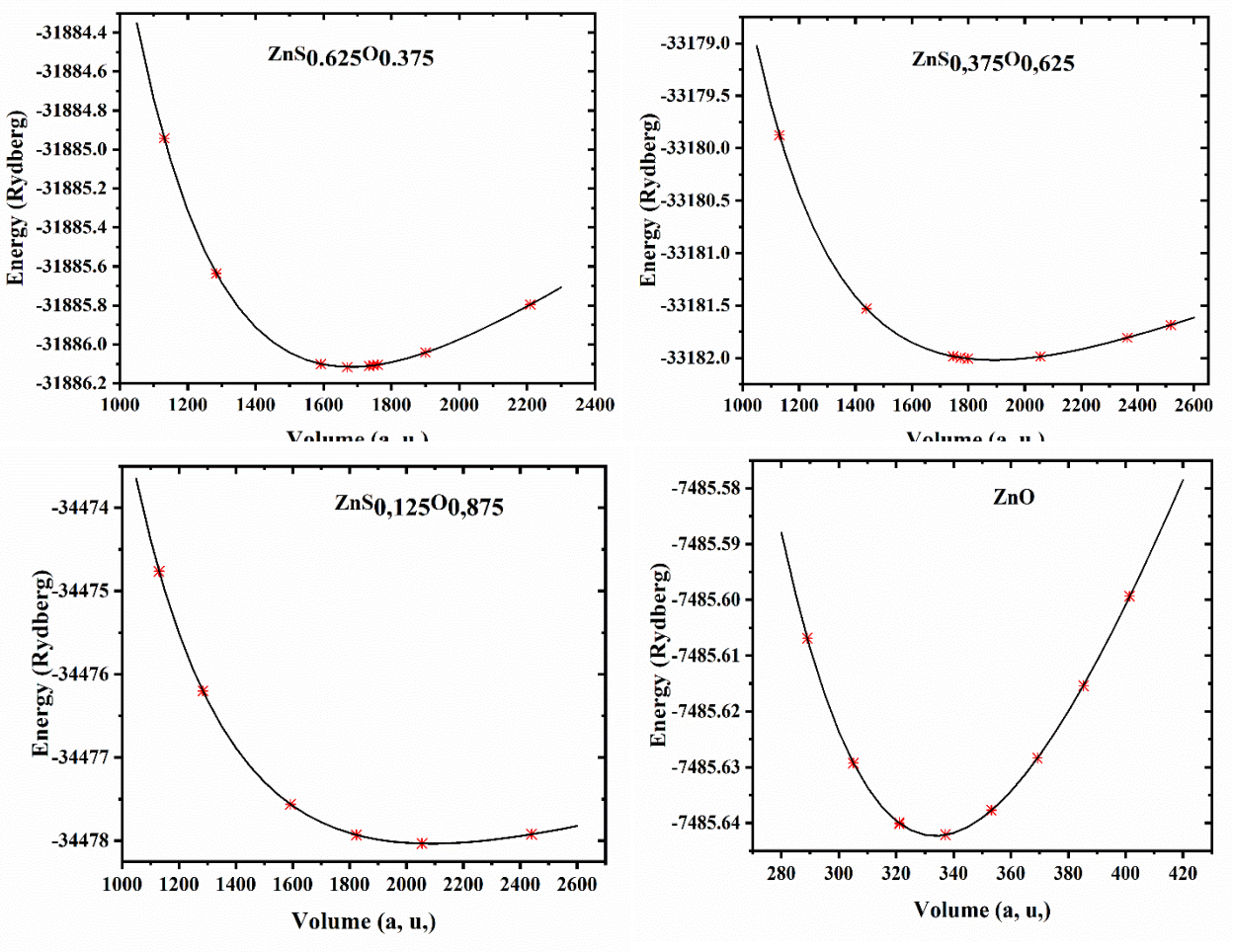

Fig. III.1 energy vs unit cell volume for $ZnS_{1-x}O_x$ using PBE-GGA functional.

In Fig. III.2, we depict the influence of oxygen content on the lattice parameters of the $ZnS_{1-x}O_x$ ternary alloy. Both parameters a and c exhibit a slight increase as the oxygen content (x) increases. The second-order fit of lattice parameters a and c yields the following relationships:

$$a(x) = 3.29683 + 0.6999x - 0.13165x^2 \quad \text{(III.23)}$$

$$c(x) = 5.296619 + 0.934504x + 0.046215x^2 \quad \text{(III.24)}$$

The disparity between the experimentally observed lattice parameters (a, c) and our calculated values is relatively modest, with deviations of (0.96%, 0.92%) for ZnO and (4%, 0.69%) for ZnS. The agreement of our calculated bulk modulus (B_0) with experimental data is also reasonable, falling within 10.64% for ZnO and 13.07% for ZnS. Notably, our calculated lattice constants (a, c) tend to be higher than the experimentally reported values in [34-36] for both ZnS and ZnO. On the other hand, our determined B_0 for ZnS is underestimated compared to the experimental values mentioned in [37,38]. However, it's

worth highlighting that our calculated values exhibit good overall agreement when compared to both experimental results [37-39] and other computational analyses [30-32,37,38].

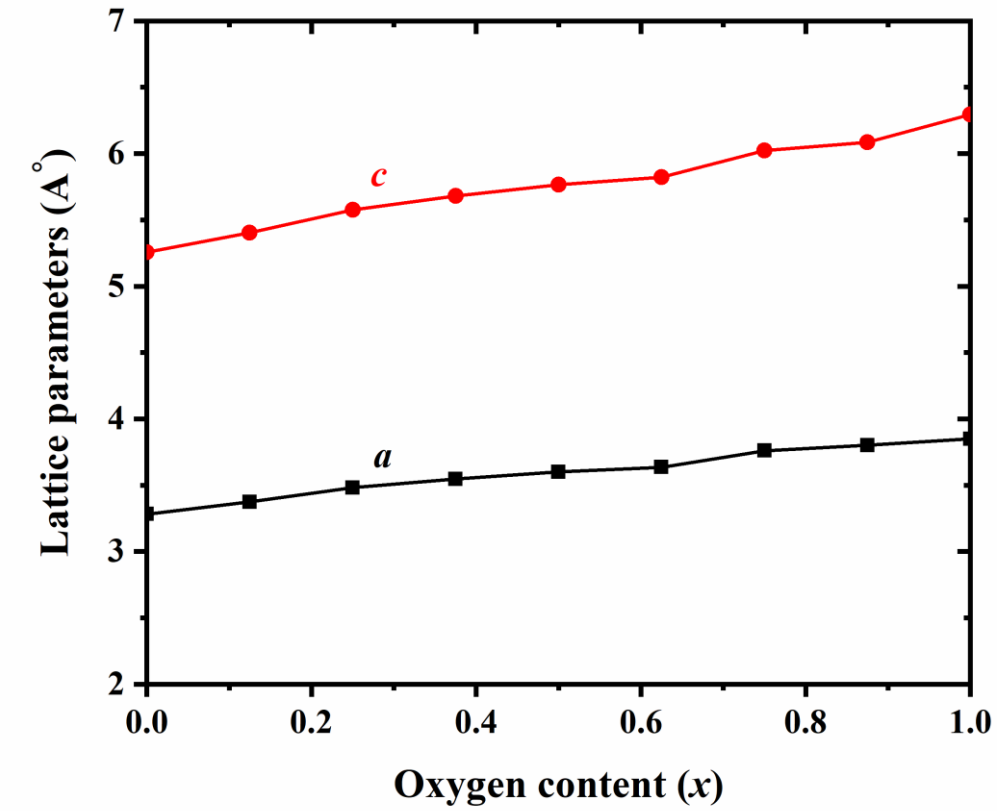

Fig. III.2: The effect of oxygen content (x) on lattice parameters a and c within the GGA approximation.

In Fig. III.3, we illustrate the influence of oxygen content (x) on the bulk modulus, calculated using the GGA approximation and compared with the VCA method. The GGA model demonstrates favorable agreement with the VCA method. The quadratic term in Equations (III.23 and III.24) represents the lattice constant bowing parameter. The existence of this bowing parameter indicates non-linear behavior in the lattice constant of $ZnS_{1-x}O_x$ with respect to the composition (x). This observation confirms a deviation from Vegard's rule.

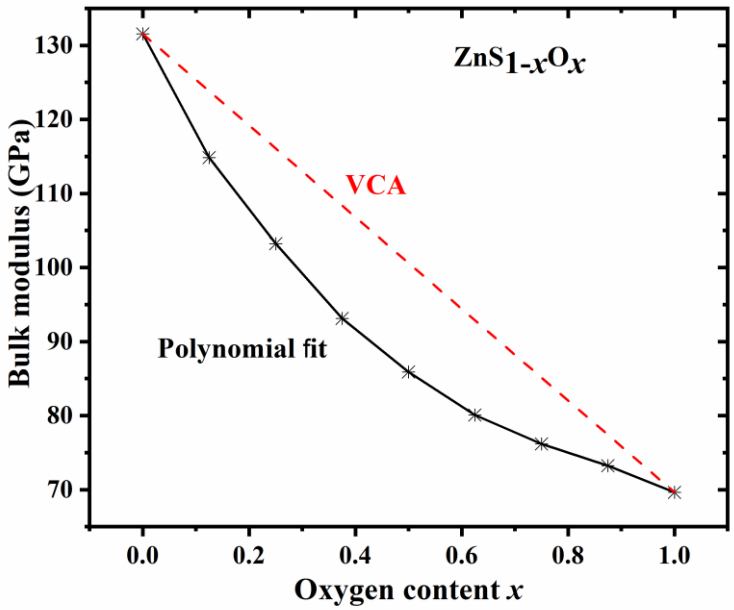

Fig. III.3: Influence of Oxygen content (x) on the bulk modulus of $ZnS_{1-x}O_x$, calculated using the GGA approximation and compared with the VCA method.

The phonon spectra in wurtzite ZnS, $ZnS_{0.5}O_{0.5}$, and ZnO, as illustrated in Fig. III.4, exhibit a negative segment, indicating dynamical instability. In the wurtzite structure, $ZnS_{1-x}O_x$ demonstrates a sufficient band gap and absorption coefficient, making it suitable for use as a buffer in solar cells, despite the observed dynamical instability. It's worth noting that the zinc blende structure is more stable in comparison.

III.4.2.2 Band structure and projected DOS

The dispersion relation of electrons in the momentum space, derived from the electronic band structure of the fully relaxed unit cell, characterizes the energy ranges accessible to electrons within a solid. This information provides valuable insights into the material, including details about its band gap, which influences photon absorption and charge transport capabilities.

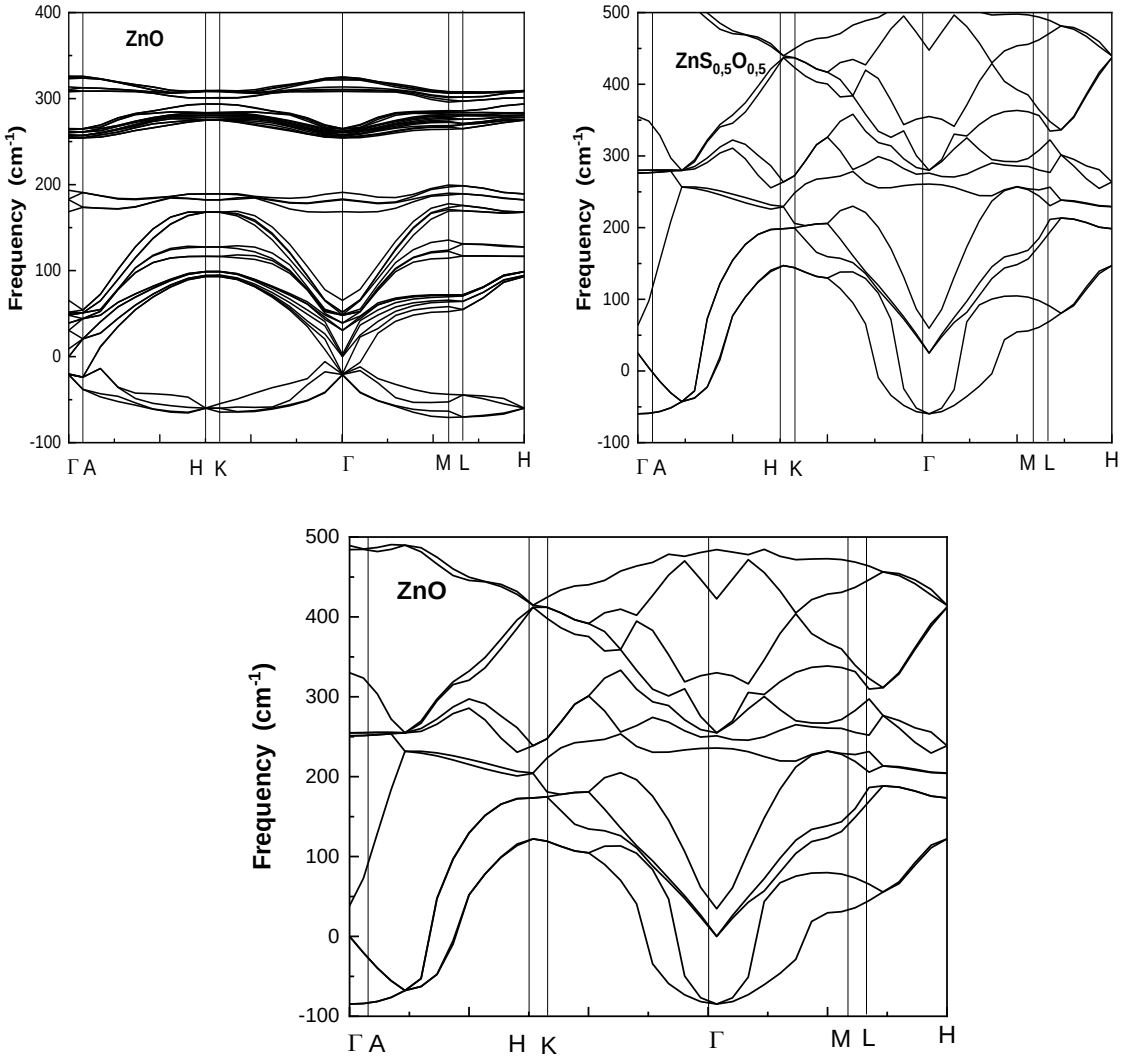

Fig. III.4: Phonon spectra in the wurtzite structures of ZnS, $ZnS_{0.5}O_{0.5}$, and ZnO.

We will delve into the electronic band structures and the projected densities of states (PDOS) of materials. Illustrated in Fig. III.5 are the band structures of the $ZnS_{1-x}O_x$ alloy, with x values ranging from 0 to 1 (0, 0.125, 0.25, 0.375, 0.5, 0.625, 0.75, 0.825, and 1), calculated using both GGA and the modified Becke-Johnson potential (TB-mBJ) approximation. The conduction band's lowest energy is observed at the Γ point, while the valence band's highest energy occurs at the Γ point, indicating a direct Γ-Γ band gap for $ZnS_{1-x}O_x$ with various compositions x in the range of 0 to 1. The upper valence band spans from approximately - 4.85 eV to the Fermi level E_F.

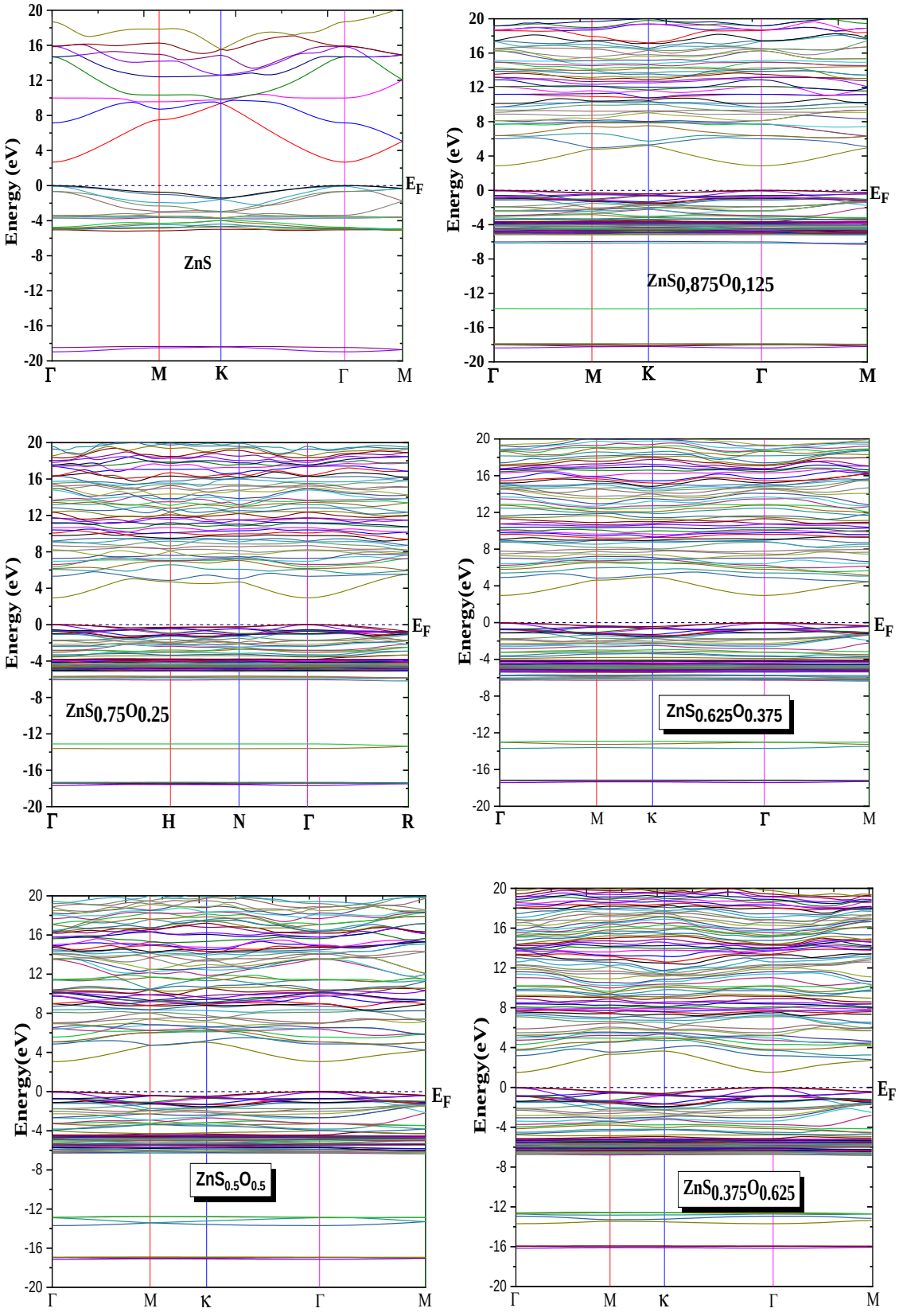
Energy (eV)
E_F
ZnS
Γ M K Γ M
ZnS0,875O0,125
Γ M K Γ M
ZnS0.75O0.25
Γ H N Γ R
Energy(eV)
ZnS0.625O0.375
Γ M κ Γ M
ZnS0.5O0.5
Γ M κ Γ M
ZnS0.375O0.625
Γ M κ Γ M

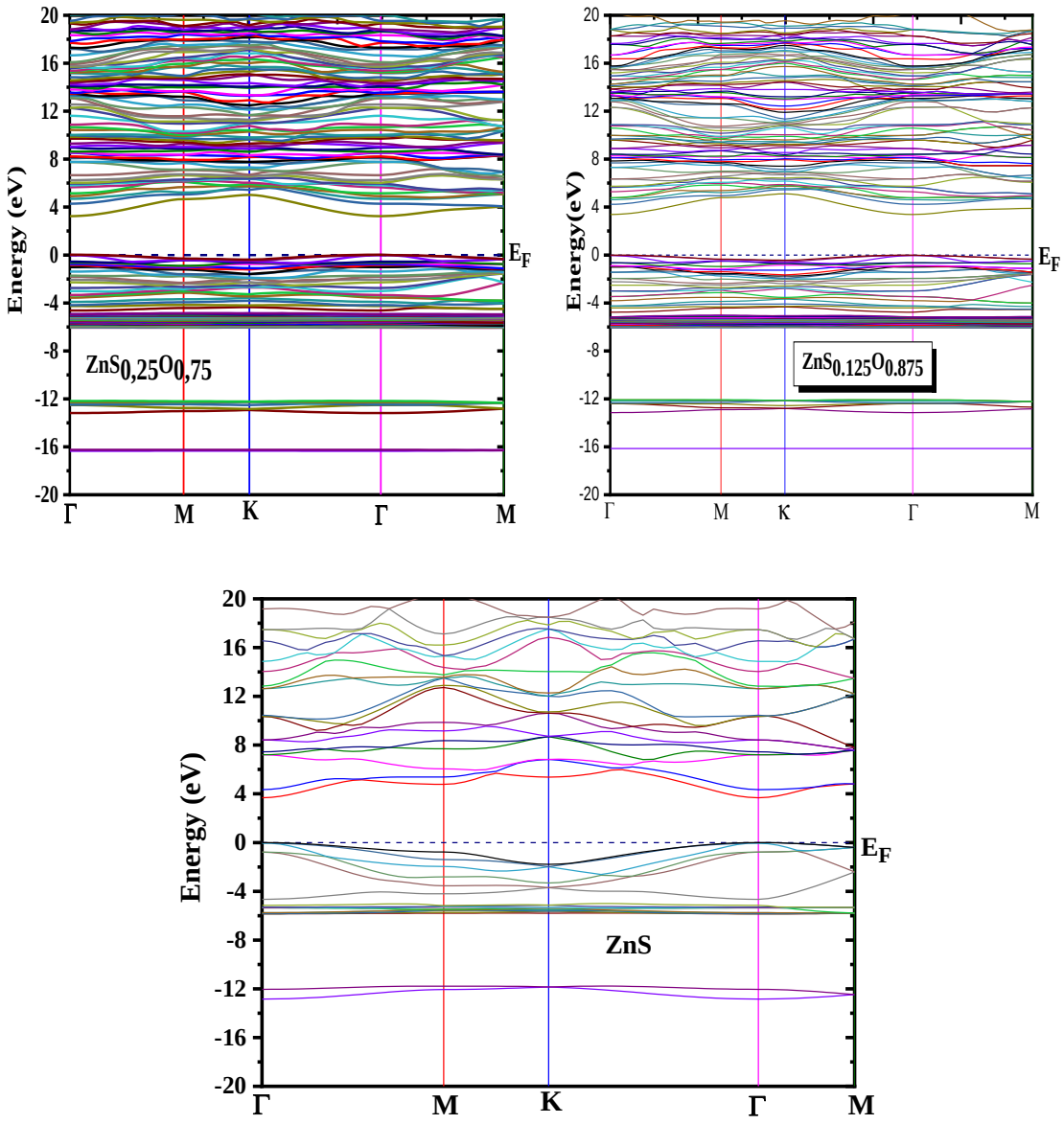

Fig. III.5: Relaxed band structure of $ZnS_{1-x}O_x$ alloys at the equilibrium lattice constant, with (x = 0, 0.125, 0.25, 0.375, 0.5, 0.625, 0.75, 0.875, 1) for mBJ-GGA functional.

Table III.4: The band gap (Γ-Γ) of $ZnS_{1-x}O_x$ alloy.

	x	**0**	**0.125**	**0.250**	**0.375**	**0.5**	**0.625**	**0.750**	**0.875**	**1**
***E_g* (eV)**	T.W.	2.6836	2.8622	2.9551	2.960	3.0602	3.137	3.2384	3.383	3.6809
	Oth	2.68[29]	2.78[36]	3 [35]		2.82[35]		3.05[35]		3.6[35]
	Exp	3.03[36]		2.831[37]		2.77[37]		3.03[37]		3.7 [2]

Table III.4 presents the direct Γ-Γ band gap of the $ZnS_{1-x}O_x$ alloy for various compositions (x) in the range of 0 to 1 reveal a semiconductor character with band gaps of 2.68 eV, 2.86 eV, 2.95 eV, 2.96 eV, 3.06 eV, 3.13 eV, 3.23 eV, and 3.68 eV, respectively. These values align with existing theoretical data [29, 35, 36] and experimental results [2, 36, 37]. The band gap determined through the (TB-mBJ) approximation closely aligns with

experimental values compared to those obtained from GGA+U or LDA+U methods [39]. The Tran-Blaha modified Becke-Johnson exchange potential approximation (TB-mBJ) was employed to enhance electronic properties, specifically targeting the band gap value.

Fig. III.6 illustrates the impact of Oxygen content (x) on the fundamental band gap of the $ZnS_{1-x}O_x$ alloy, revealing an increase as x increases. This trend aligns with observations in the $ZnMg_{1-x}O_x$ alloy, where the band gap increases with increasing Mg concentration [40]. The (TB-mBJ) approach provides a more accurate estimation of the electronic band gap, aligning closely with experimentally calculated values [41].

The quadratic polynomial fit yields the following relation:

$$E_g(x) = 2.76295 + 0.31954x + 0.51989x^2 \quad \text{(III.25)}$$

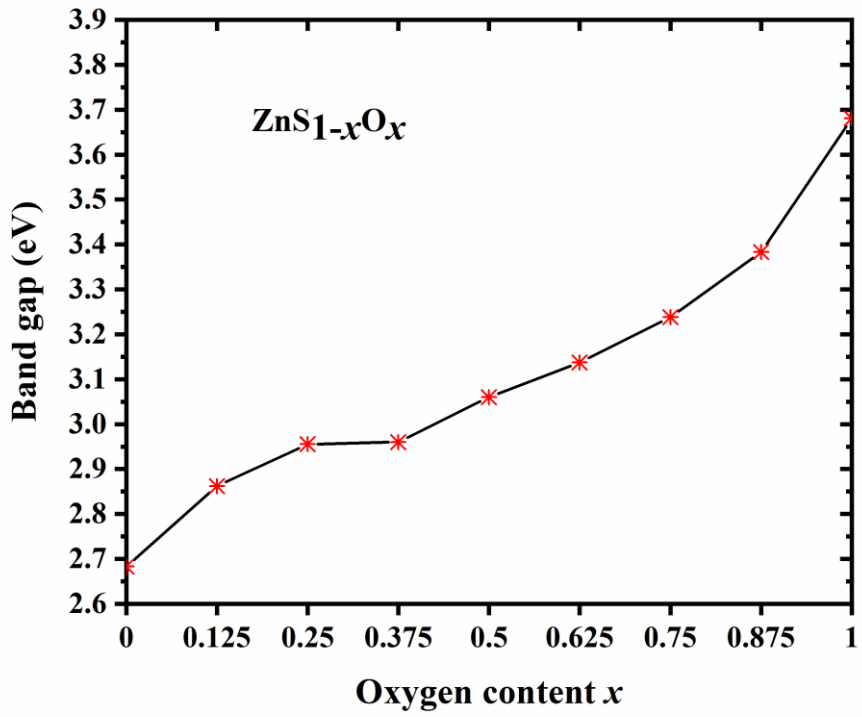

Fig. III.6: Band gap as a function of oxygen content x for relaxed $ZnS_{1-x}O_x$ alloy using the mBJ-GGA approximation.

Fig. III.7 and Fig. III.8 depicts the projected densities of states for the $ZnS_{1-x}O_x$ alloy, with x values of 0, 0.5, and 1. Notably, the PDOS profiles for the studied compounds reveal common features, where the Zn d and O p states exhibit a similar profile across the entire energy region. This similarity suggests the presence of hybridization between Zn d and O p electrons, indicating covalent bonding between them. The primary contribution to the upper valence band comes from the Zn d and O p states. Conversely, the lower conduction band is

unoccupied in all compounds, leading to transitions primarily originating from O p and Zn d states. In practical terms, describing charges in molecules involves partitioning the system into atomic fragments. The charge density at each point is then distributed among atoms proportionally to their free atomic density, creating a distribution that mirrors the molecular density. Atomic charges and multipole moments serve as a summary of the molecular charge reorganization, enabling the computation of the external electrostatic potential and the interaction energy between molecules.

Mulliken population analysis of ZnS and ZnO compounds facilitates the depiction of charge transfer and binding interactions within molecular systems. The lengths and overlap populations of the shortest atomic bonds, along with Hirshfeld populations and charges of ZnS and ZnO, are presented in Table III.5 and Table III.6. We also present the partial atomic charges for different atoms in ZnS and ZnO. The calculated atomic charges align with the expected chemical trends and are comparable to the Hirshfeld atomic charges. Analyzing Table III.5 and Table III.6 reveals a relatively significant charge transfer from the Zn site to the O state in the inner region compared to Zn to S atoms in the outer region. The Mulliken populations obtained provide insights into the charge transfer and bond types post-bonding. A positive atomic population value indicates the degree to which atoms are losing electrons, whereas a negative value signifies the extent of atoms gaining electrons. Moreover, a bond with a larger bond population reflects stronger covalent characteristics. The average population values for Zn and O atoms in ZnO were 0.83 and −0.83, respectively, suggesting that Zn atoms tend to lose electrons, and O atoms tend to gain electrons. In ZnS, the average population of Zn and S atoms was 0.49 and −0.49, indicating a tendency for Zn atoms to lose electrons, and S atoms to gain electrons. The calculated Zn1−O2 and Zn2−O1 (Zn1−S2 and Zn2−S1) populations and bond lengths are 0.20 and 2.00612 Å (1.62 and 2.35721 Å). Similarly, the computed Zn1−S1 and Zn2−S2 (Zn1−O1 and Zn2−O2) populations and bond lengths are 0.18 and 2.36066 Å (0.20 and 2.00612 Å).

Table III.5: Atomic Populations (Mulliken), bond, length and Hirshfeld analysis of ZnS.

Species	Ion	s	p	d	f	Total	Charge (e)	Bond	Population	Length (Å)
S	1	1.82	4.67	0.00	0.00	6.49	-0.49	S2-Zn1	1.62	2.35721
S	2	1.82	4.67	0.00	0.00	6.49	-0.49	S1-Zn2	1.62	2.35721
Zn	1	0.58	0.95	9.98	0.00	11.51	0.49	S1-Zn1	0.18	2.36066
Zn	2	0.58	0.95	9.98	0.00	11.51	0.49	S2-Zn2	0.18	2.36066
All bands spilling parameter for spin component 1 = 2.12 %										
Hirshfeld Analysis										
Species	Ion	Hirshfeld	Charge (e)	Spin (hbar/2)						
S	1	-0.23	0.00							
S	2	-0.23	0.00							
Zn	1	0.23	0.00							
Zn	2	0.23	0.00							

Table III.6. Atomic Populations (Mulliken), bond, length and Hirshfeld analysis of ZnO.

Species	Ion	s	p	d	f	Total	Charge (e)	Bond	Population	Length (Å)
O	1	1.86	4.97	0.00	0.00	6.83	-0.83	O2-Zn1	1.11	1.99777
O	2	1.86	4.97	0.00	0.00	6.83	-0.83	O1-Zn2	1.11	1.99777
Zn	1	0.49	0.71	9.97	0.00	11.17	0.83	O1-Zn1	0.20	2.00612
Zn	2	0.49	0.71	9.97	0.00	11.17	0.83	O2-Zn2	0.20	2.00612
All bands spilling parameter for spin component 1 = 0.85 %										
Hirshfeld Analysis										
Species	Ion	Hirshfeld	Charge (e)	Spin (hbar/2)						
O	1	-0.34	0.00							
O	2	-0.34	0.00							
Zn	1	0.34	0.00							
Zn	2	0.34	0.00							

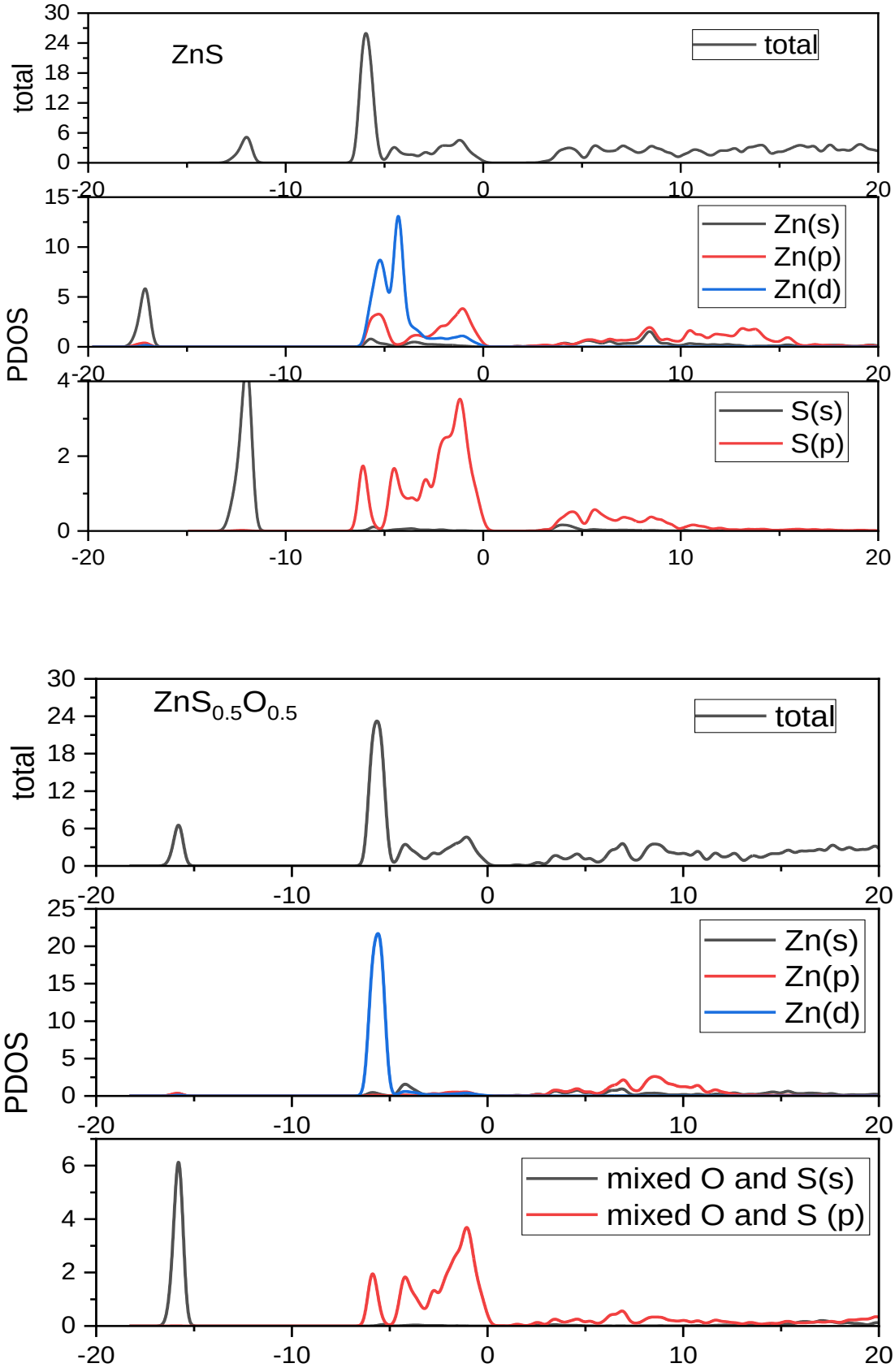

Fig. III.7. Projected partial densities of states of ZnS and $ZnS_{0.5}O_{0.5}$.

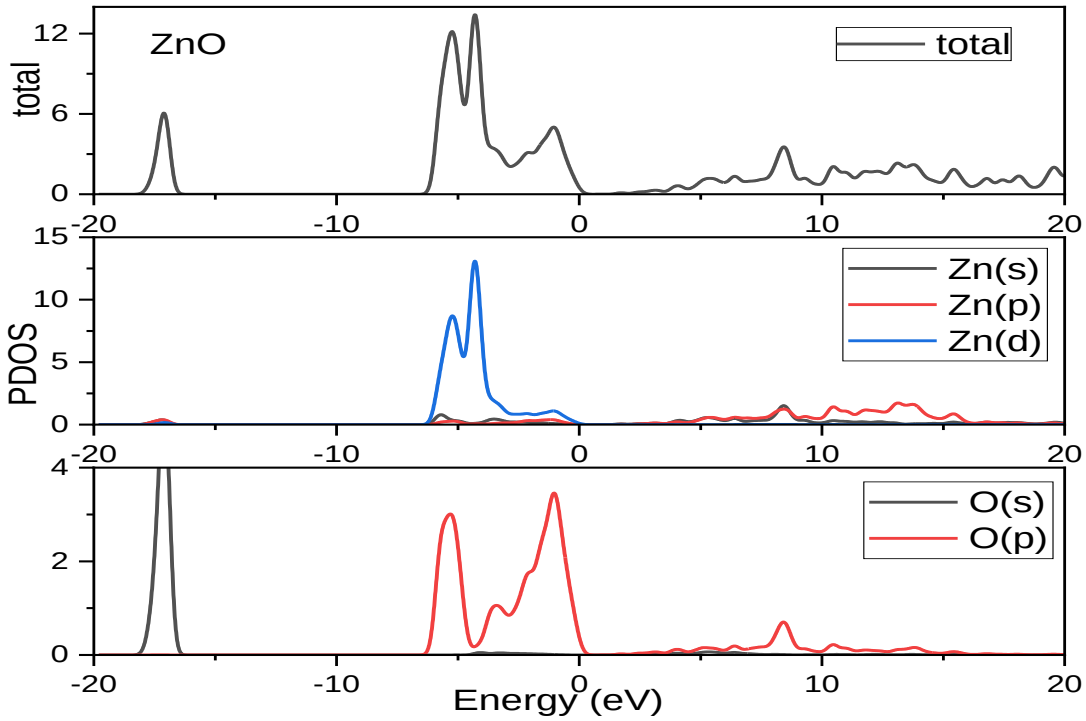

Fig. III.8. Projected partial densities of states of ZnO.

III.4.2.3 Optical properties

The calculations included the determination of the real and imaginary parts of the dielectric function, absorption coefficient, optical conductivity, refractive index, extinction coefficient, reflectivity, and electron energy loss. These parameters exhibit anisotropic behavior for a material in the wurtzite phase, specifically in the in-plane [100] and out-of-plane [001] crystallographic directions of the optimized structure. Fig. III.9 illustrates the impact of photon energy on the real part of the dielectric function for both in-plane [100] and out-of-plane [001] directions. Notably, the static dielectric function values fall within the range of 2.3 to 4.3 as the *x* content varies from 0 to 1. The real dielectric function is instrumental in anticipating the nonlinear optical behavior of the material. Fig. III.10 depicts the influence of photon energy on the imaginary part of the dielectric function for both in-plane [100] and out-of-plane [001] crystallographic directions in the $ZnS_{1-x}O_x$ alloy, considering different oxygen contents (*x*). The imaginary part of the dielectric function characterizes the absorptive capacity of the material. It is notable that both the in-plane and out-of-plane imaginary components of the dielectric function exhibit a non-zero magnitude at the energy corresponding to the direct Γ-Γ band gap value of the $ZnS_{1-x}O_x$ alloy.

The prominent peaks in the in-plane and out-of-plane dielectric functions are situated at 6.5 eV and 7.75 eV, respectively, indicating inter-band transitions. Notably, photon

emission is not feasible in this material. The intensity of these peaks in both the real and imaginary parts of the dielectric function increase as the oxygen content decreases.

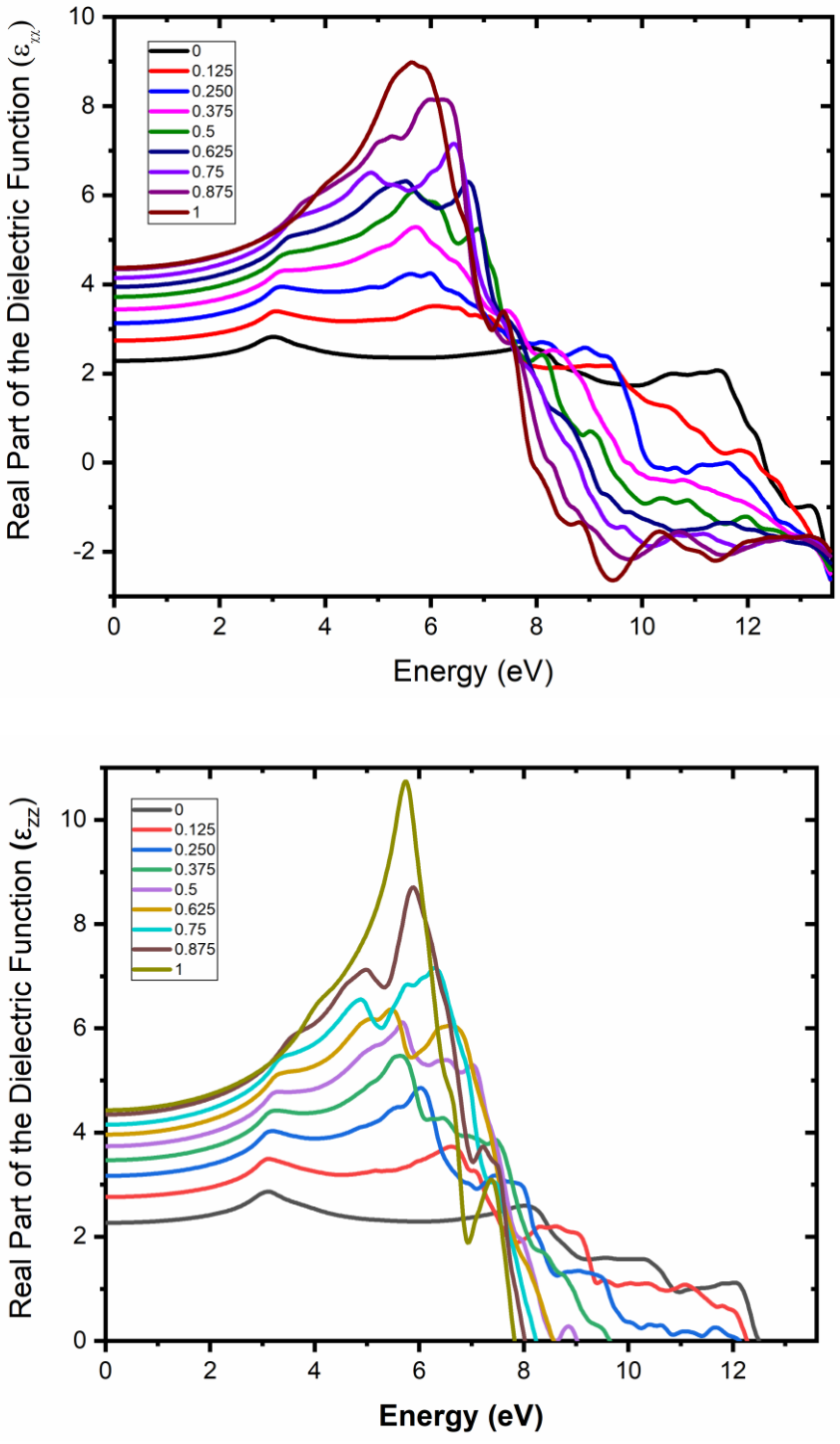

Fig. III.9: Impact of photon energy on (a) in-plane and (b) out-of-plane real part of the dielectric function for $ZnS_{1-x}O_x$ alloy at various oxygen content *x*.

Figure III.11 illustrates the absorption coefficient as a function of photon energy for both in-plane [100] and out-of-plane [001] crystallographic directions in the $ZnS_{1-x}O_x$ alloy

with different oxygen content (x). The absorption coefficient is directly linked to the extinction coefficient through the relation:

$$\alpha(\omega) = \frac{2\omega}{c} k \qquad \text{(III.26)}$$

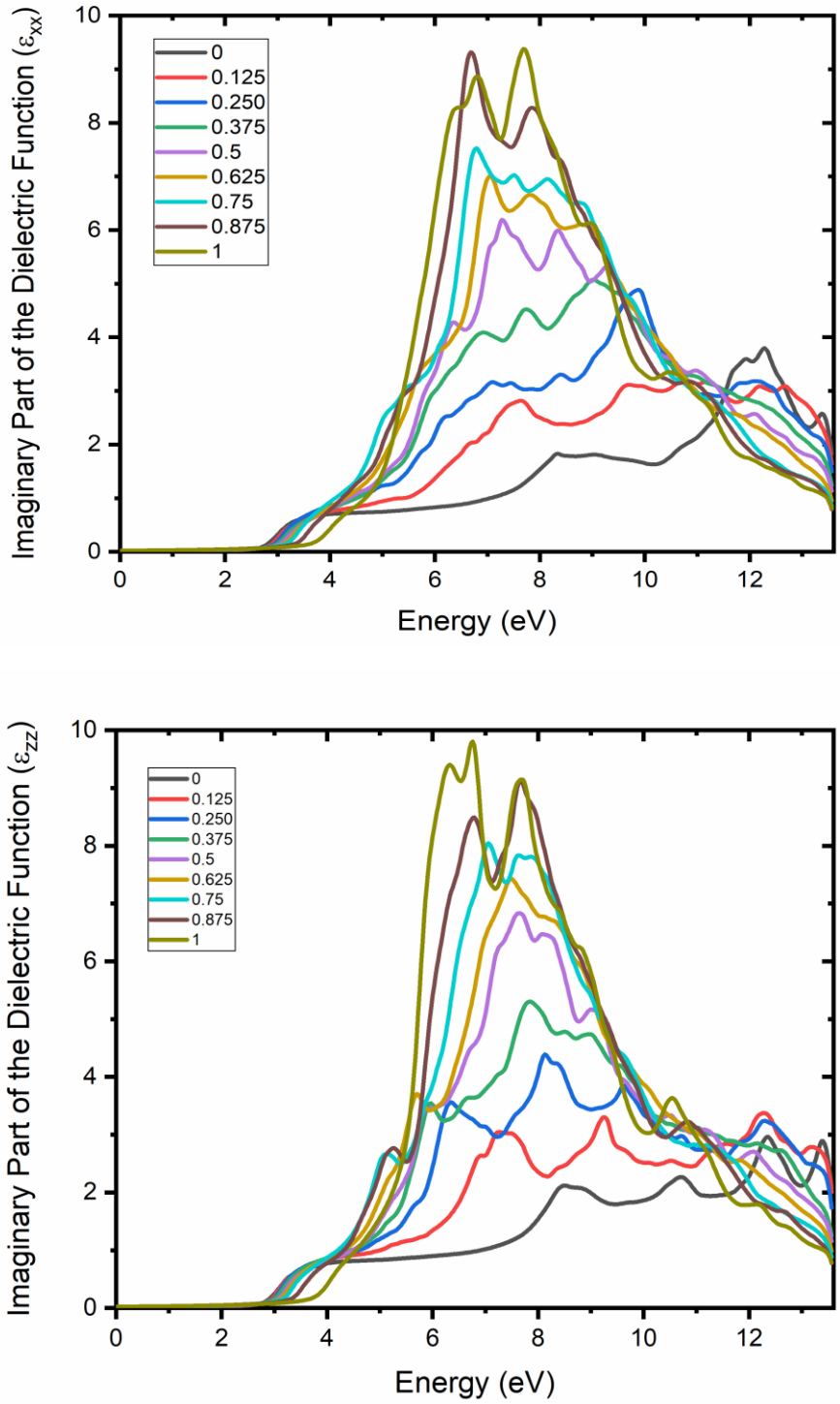

Fig. III.10: Effect of photon energy on (a) in-plane and (b) out-of-plane imaginary Part of the dielectric function for $ZnS_{1-x}O_x$ alloy at various oxygen content x.

This material is documented to absorb ultraviolet light within the 4 eV to 10 eV range. This enhancement solidifies the suitability of $ZnS_{1-x}O_x$ for use in optical and photovoltaic devices. Notably, the absorption coefficient of the $ZnS_{1-x}O_x$ system falls within the range of 10^5 cm^{-1}, indicating a characteristic property of a highly effective absorber material.

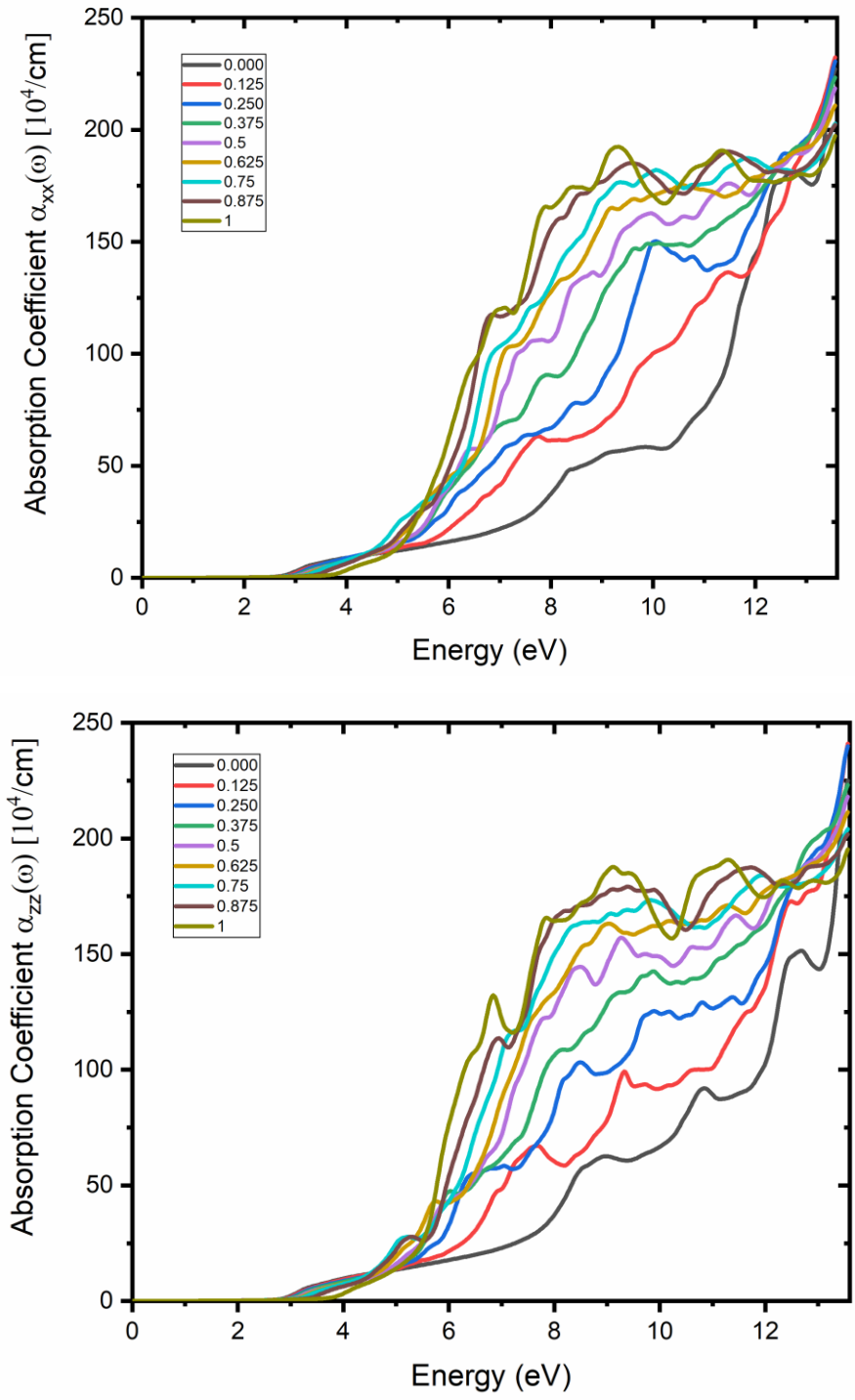

Fig. III.11: Effect of photon energy on (a) in-plane and (b) out-of-plane absorption coefficient of $ZnS_{1-x}O_x$ alloy at various oxygen content *x*.

Fig. III.12 illustrates the impact of photon energy on the optical conductivity for both in-plane [100] and out-of-plane [001] crystallographic directions in the $ZnS_{1-x}O_x$ alloy, considering different oxygen contents (x). The optical conductivity is directly linked to the imaginary part of the dielectric function.

$$\alpha(\omega) = \frac{\omega}{4\pi}\varepsilon_2(\omega) \tag{III.27}$$

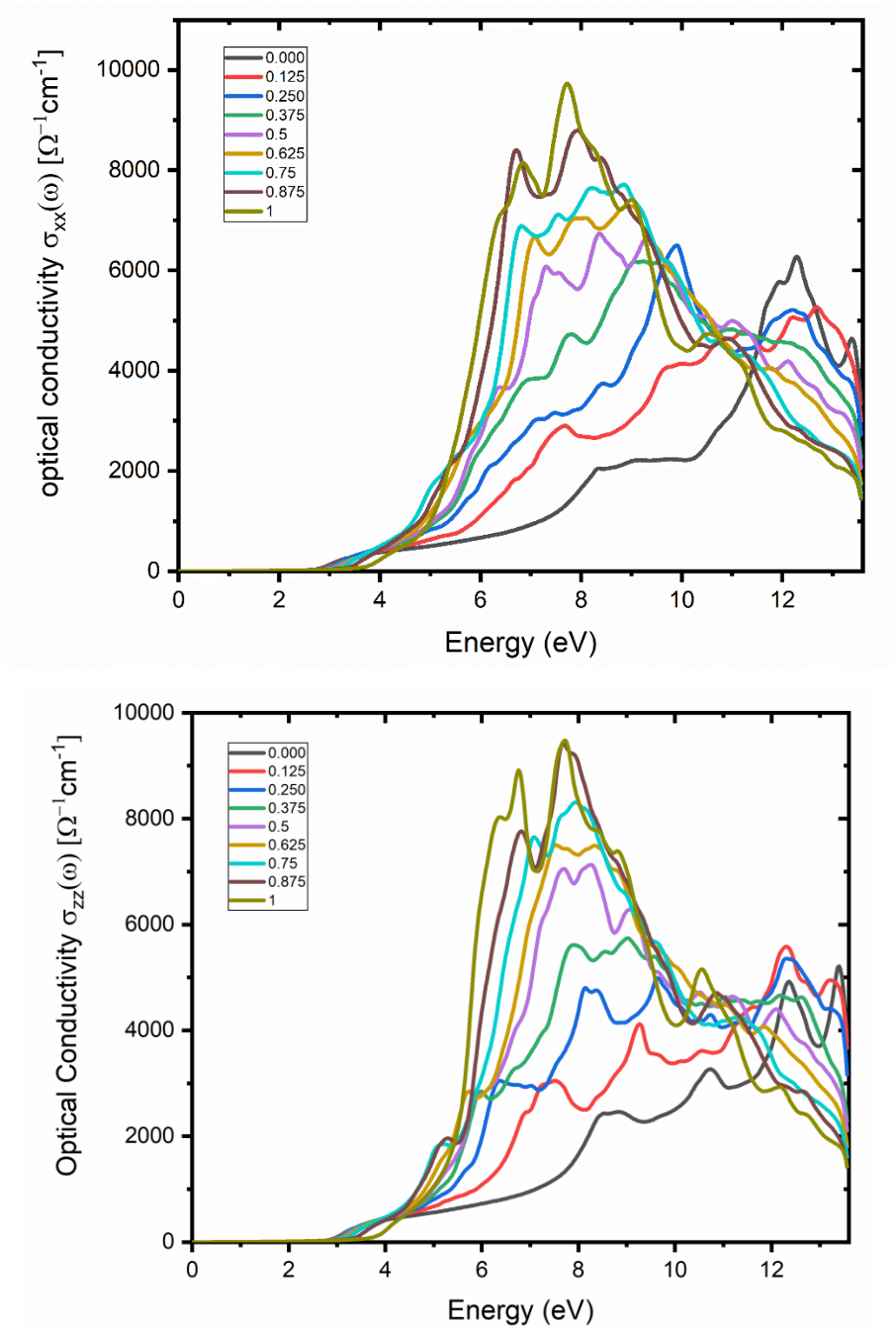

Fig. III.12: Effect of photon energy on (a) in-plane and (b) out-of-plane optical conductivity of $ZnS_{1-x}O_x$ alloy at various oxygen content x.

In the spectral range spanning from 3.5 eV to 12.5 eV, the out-of-plane component of the optical conductivity closely mirrors its in-plane counterpart. Notably, a plateau in the conductivity spectrum is observed at approximately 9000 $\Omega^{-1}cm^{-1}$, situated between 6 eV and 8 eV. Furthermore, the optical conductivity demonstrates an increase with the rise in oxygen content (*x*).

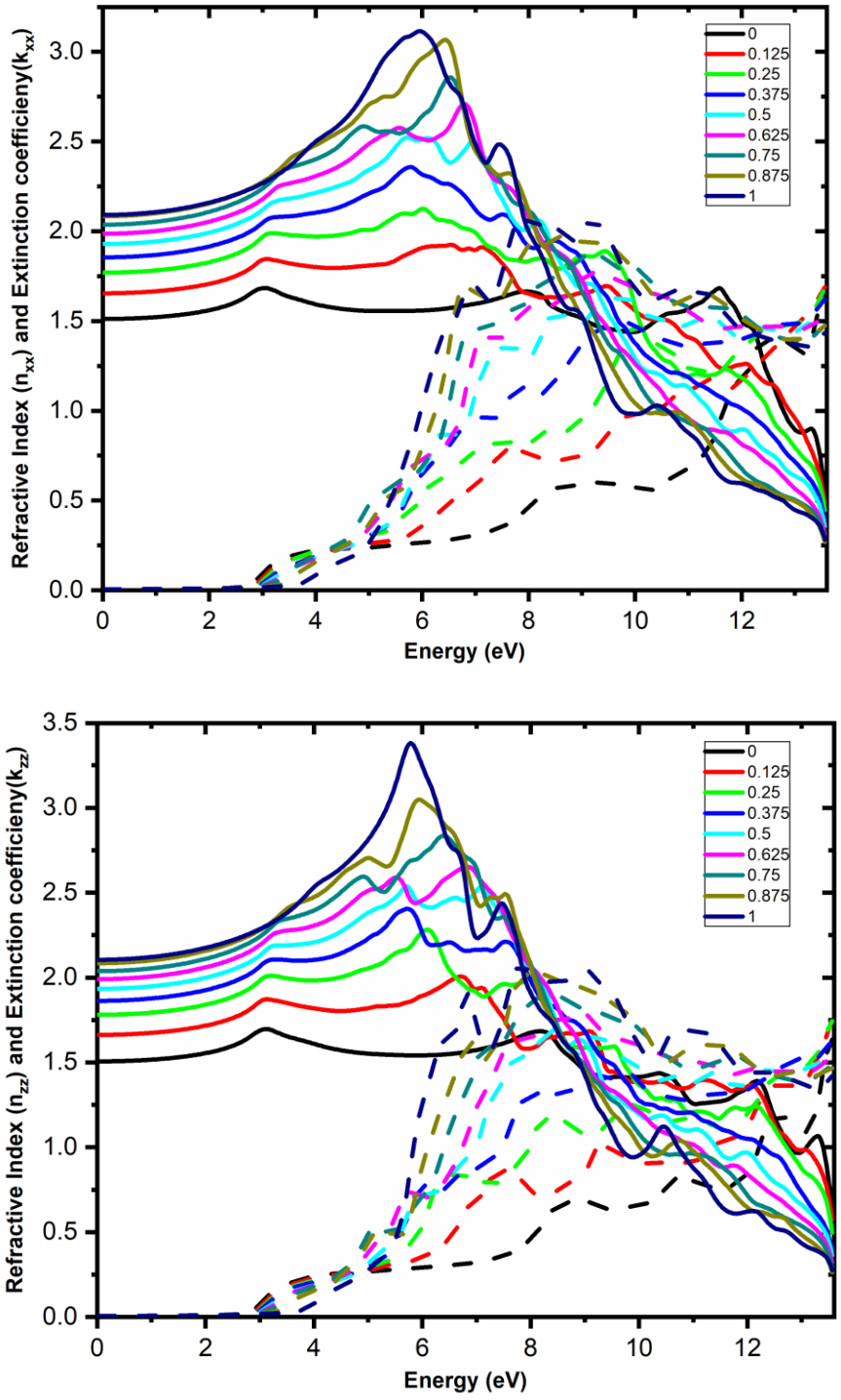

Fig. III.13: Effect of photon energy on (a) in-plane and (b) out-of-plane reflectivity of $ZnS_{1-x}O_x$ alloy at various oxygen content *x*.

The complex refractive index N is expressed as $N = n + ik$, where $n(\omega)$ represents the refractive index and $k(\omega)$ represents the extinction coefficient. The complex refractive index N is intricately linked to the dielectric constant through the relationship:

$$N = \sqrt{\varepsilon} \tag{III.28}$$

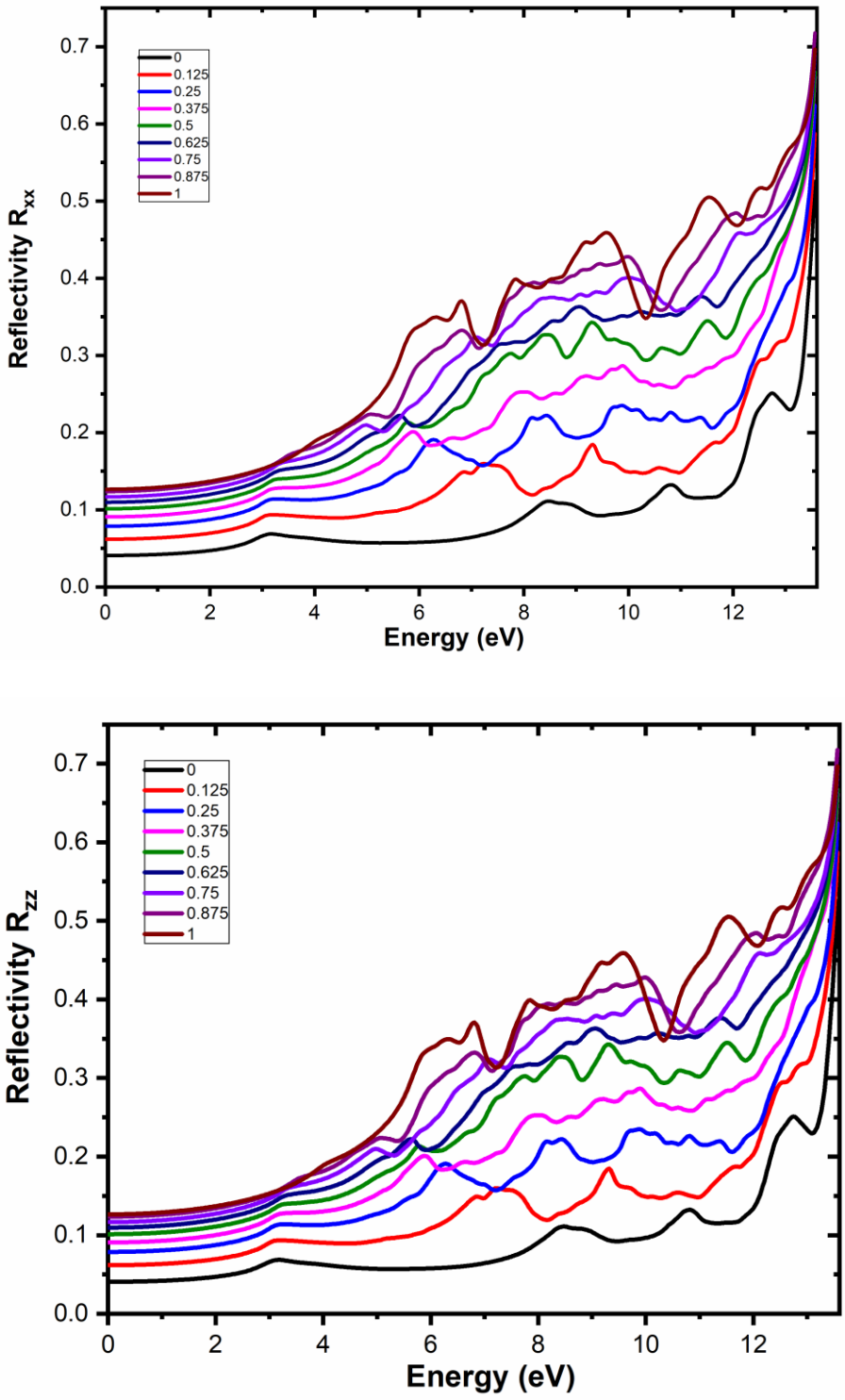

Fig. III.14: Effect of photon energy on (a) in-plane and (b) out-of-plane reflectivity of $ZnS_{1-x}O_x$ alloy at various oxygen content x.

The refractive index and extinction coefficient are directly connected through the following expressions:

$$n(\omega) = \frac{\sqrt{\varepsilon_1^2(\omega) + \varepsilon_2^2(\omega)} + \sqrt{\varepsilon_1^2(\omega)}}{\sqrt{2}} \quad \text{(III.29)}$$

$$k(\omega) = \frac{\sqrt{\varepsilon_1^2(\omega) + \varepsilon_2^2(\omega)} - \sqrt{\varepsilon_1^2(\omega)}}{\sqrt{2}} \quad \text{(III.30)}$$

Fig. III.13 illustrates the influence of photon energy on the refractive index and the extinction coefficient for both in-plane [100] and out-of-plane [001] crystallographic directions in the $ZnS_{1-x}O_x$ alloy.

The refractive index of the material serves as an indicator of its transparency to incident spectral radiation. Notably, the static refractive index experiences a decrease from 2.1 to 1.5 as the oxygen content (x) varies from 0 to 1. Additionally, both in-plane and out-of-plane extinction coefficients initiate at an energy corresponding to the direct band gap value of the $ZnS_{1-x}O_x$ alloy. The refractive index is more important when photons move through the material and when bonds between atoms are covalent.

Reflectivity shown in Fig. III.14 serves as an indicator of a material's capacity to reflect radiation. It is expressed as a function of the refractive index and extinction coefficient through the following relationship:

$$R(\omega) = \frac{(n-1)^2 + k^2}{(n+1)^2 + k^2} \quad \text{(III.31)}$$

The reflectivity of the $ZnS_{1-x}O_x$ alloy initiates around a photon energy of 3 eV and exhibits multiple peaks, both maxima and minima, particularly in the realm of extreme ultraviolet light. However, practical considerations such as surface roughness, thickness uniformity, interdiffusion, oxidation, and thermal stability impose limitations on reflectivity. The anisotropic optical characteristics, coupled with a band gap range of 2.5 to 3.6 eV and absorption capability in the extreme ultraviolet spectrum, position the $ZnS_{1-x}O_x$ alloy as a suitable material for applications such as lenses, absorbers and windows in solar cells.

Fig. III.15 illustrates the impact of photon energy on in-plane and out-of-plane electron energy loss in the $ZnS_{1-x}O_x$ alloy, considering various oxygen contents (x). The

electron energy loss is directly associated with both the real and imaginary parts of the dielectric function.

$$L(\omega) = \frac{\varepsilon_2(\omega)}{\varepsilon_1^2(\omega) + \varepsilon_2^2(\omega)} \tag{III.32}$$

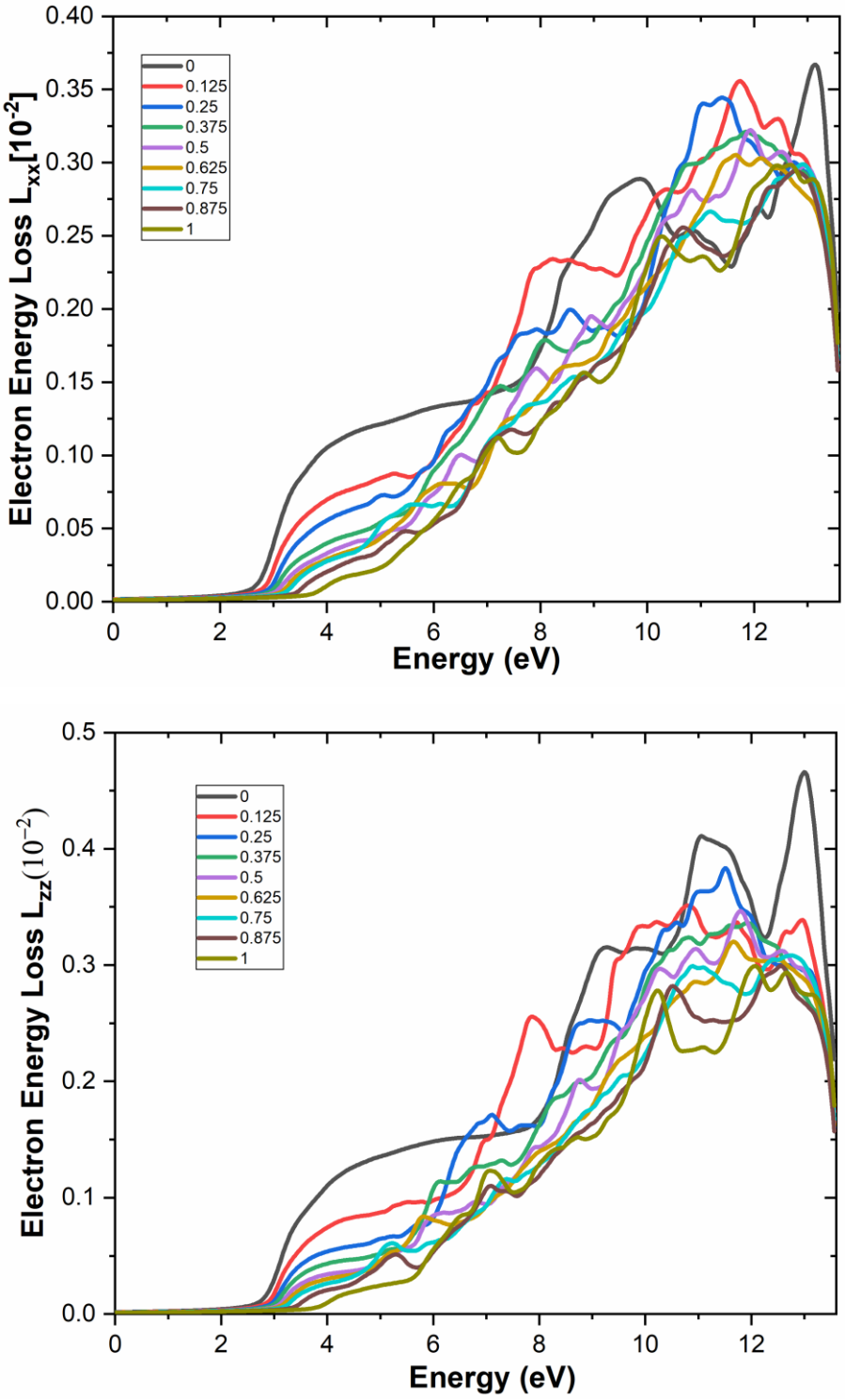

Fig. III.15: Effect of photon energy on (a) in-plane and (b) out-of-plane electron energy loss of $ZnS_{1-x}O_x$ alloy at various oxygen content *x*.

The characteristics of the energy-loss spectra are linked to the photonic band structure of the crystal. The interaction between electrons and the crystal significantly contributes to energy loss. In the case of the $ZnS_{1-x}O_x$ alloy, electron energy loss is concentrated in the region of extreme ultraviolet light.

III.5 Conclusion

In this chapter, the DFT method was employed to scrutinize the structure, electronic, and optoelectronic properties of the $ZnS_{1-x}O_x$ system which exhibits anisotropic optical parameters, with a band gap ranging from 2.5 eV to 3.6 eV, making it suitable for photovoltaic applications such as windows or buffer materials. The refractive index becomes particularly crucial when photons traverse the material, especially in cases of covalent atomic bonds. Notably, the static refractive index experiences a decrease from 2.1 to 1.5 as the oxygen content (x) increases from 0 to 1. Both in-plane and out-of-plane extinction coefficients initiate at an energy corresponding to the direct band gap value of the $ZnS_{1-x}O_x$ alloy. $ZnS_{1-x}O_x$ demonstrates UV light absorption within the 4 eV to 10 eV range, validating its potential for use in optical and photovoltaic devices due to its band gap properties. The similar profile of Zn d and O p throughout the entire energy region suggests the presence of hybridization between their electrons and covalent bonding between them.

In the following chapter, we will discuss the fabrication and characterization of S-doped ZnO (ZnO:S) thin films, we will provide the experimental conditions, and process steps required to producing and analyzing thin-films of ZnS, ZnO with and without sulfur doping (2%, 4%, 8%) using the Sol-Gel spin-coating method.

References

[1] Junfu QiXi'an, Yuefeng YinMonash, Xiangdong Ding, Jun Sun, Junkai Deng, Materials today communications, vol. 5 (2020) 101259. doi:10.1016/J.MTCOMM.2020.101259

[2] Jesse Huso, Leah Bergman, Matthew D. McCluskey, Journal of Applied Physics, vol. 125, (2019) 075704; doi:10.1063/1.5064371

[3] A. Bellouche, Ahmed Gueddim, S. Zerroug, Nadir Bouarissa, Optik - International Journal for Light and Electron Optics vol. 127, issue 23 (2016) 11374-11378. doi:10.1016/j.ijleo.2016.09.034

[4] Gueddim, A. et al. "Composition Dependence of the Optical Properties and Band Structure of the Zinc-Blende $ZnS_{1-x}O_x$: A First Principles Study." Philosophical Magazine, vol. 95, no. 24, 2015, pp. 2627-2638, doi:10.1080/14786435.2015.1073401.

[5] de Borst, René. "Challenges in Computational Materials Science: Multiple Scales, Multi-Physics and Evolving Discontinuities." Computational Materials Science, vol. 43, no. 1, 2008, pp. 1-15, doi:10.1016/j.commatsci.2007.07.022.

[6] Born, M. and R. Oppenheimer. "Zur Quantentheorie Der Molekeln." Annalen der Physik, vol. 389, no. 20, 1927, pp. 457-484, doi: 10.1002/andp.19273892002.

[7] Hartree, D. R. "The Wave Mechanics of an Atom with a Non-Coulomb Central Field. Part I. Theory and Methods." Mathematical Proceedings of the Cambridge Philosophical Society, vol. 24, no. 1, 1928, pp. 89–110., doi:10.1017/S0305004100011919.

[8] Fock, V. "Näherungsmethode Zur Lösung Des Quantenmechanischen Mehrkörperproblems." Zeitschrift für Physik, vol. 61, no. 1, 1930, pp. 126-148, doi:10.1007/BF01340294.

[9] Thomas, L. H. "The Calculation of Atomic Fields." Mathematical Proceedings of the Cambridge Philosophical Society, vol. 23, no. 5, 2008, pp. 542-548, doi:10.1017/s0305004100011683.

[10] Fermi, E. "Eine Statistische Methode Zur Bestimmung Einiger Eigenschaften Des Atoms Und Ihre Anwendung Auf Die Theorie Des Periodischen Systems Der Elemente." Zeitschrift fr Physik, vol. 48, no. 1-2, 1928, pp. 73-79, doi:10.1007/bf01351576.

[11] Dirac, P. A. M. "Note on Exchange Phenomena in the Thomas Atom." Mathematical Proceedings of the Cambridge Philosophical Society, vol. 26, no. 3, 2008, pp. 376-385, doi:10.1017/s0305004100016108.

[12] Kohn, W. and L. J. Sham. "Self-Consistent Equations Including Exchange and Correlation Effects." Physical Review, vol. 140, no. 4A, 1965, pp. A1133-A1138, doi:10.1103/PhysRev.140.A1133.

[13] Barth, U. von and L. Hedin. "A Local Exchange-Correlation Potential for the Spin Polarized Case. I." Journal of Physics C: Solid State Physics, vol. 5, no. 13, 1972, pp. 1629-1642, doi:10.1088/0022-3719/5/13/012.

[14] Vosko, S. H. et al. "Accurate Spin-Dependent Electron Liquid Correlation Energies for Local Spin Density Calculations: A Critical Analysis." Canadian Journal of Physics, vol. 58, no. 8, 1980, pp. 1200-1211, doi:10.1139/p80-159.

[15] Perdew, J. P. and Alex Zunger. "Self-Interaction Correction to Density-Functional Approximations for Many-Electron Systems." Physical Review B, vol. 23, no. 10, 1981, pp. 5048-5079, doi:10.1103/PhysRevB.23.5048.

[16] Wigner, E. "On the Interaction of Electrons in Metals." Physical Review, vol. 46, no. 11, 1934, pp. 1002-1011, doi:10.1103/PhysRev.46.1002.

[17] Ceperley, D. M. and B. J. Alder. "Ground State of the Electron Gas by a Stochastic Method." Physical Review Letters, vol. 45, no. 7, 1980, pp. 566-569, doi:10.1103/PhysRevLett.45.566.

[18] Tao, J. et al. "Climbing the Density Functional Ladder: Nonempirical Meta-Generalized Gradient Approximation Designed for Molecules and Solids." Phys Rev Lett, vol. 91, no. 14, 2003, p. 146401, doi:10.1103/PhysRevLett.91.146401.

[19] Wu, Zhigang and R. E. Cohen. "More Accurate Generalized Gradient Approximation for Solids." Physical Review B, vol. 73, no. 23, 2006, doi:10.1103/PhysRevB.73.235116.

[20] Perdew, J. P. and Y. Wang. "Accurate and Simple Analytic Representation of the Electron-Gas Correlation Energy." Phys Rev B Condens Matter, vol. 45, no. 23, 1992, pp. 13244-13249, doi:10.1103/physrevb.45.13244.

[21] Perdew, J. P. et al. "Generalized Gradient Approximation Made Simple." Phys Rev Lett, vol. 77, no. 18, 1996, pp. 3865-3868, doi :10.1103/PhysRevLett.77.3865.

[22] Rivero, P. et al. "Performance of Plane-Wave-Based Lda+U and Gga+U Approaches to Describe Magnetic Coupling in Molecular Systems." J Comput Chem, vol. 30, no. 14, 2009, pp. 2316-2326, doi:10.1002/jcc.21221.

[23] Lejaeghere, K. et al. "Reproducibility in Density Functional Theory Calculations of Solids." Science, vol. 351, no. 6280, 2016, p. aad3000, doi:10.1126/science.aad3000.

[24] P. Blaha, K. Schwarz, G. K. H. Madsen, D. Kvasnicka, J. Luitz, R. Laskowski, F. Tran and L. D. Marks, WIEN2k, An Augmented Plane Wave + Local Orbitals Program for Calculating Crystal Properties (Karlheinz Schwarz, Vienna University of Technology, Austria), 2018. ISBN 3-9501031-1-2

[25] Perdew, J. P. et al. "Restoring the Density-Gradient Expansion for Exchange in Solids and Surfaces." Phys Rev Lett, vol. 100, no. 13, 2008, p. 136406, doi:10.1103/PhysRevLett.100.136406.

[26] Tran, F. and P. Blaha. "Accurate Band Gaps of Semiconductors and Insulators with a Semilocal Exchange-Correlation Potential." Phys Rev Lett, vol. 102, no. 22, 2009, p. 226401, doi:10.1103/PhysRevLett.102.226401.

[27] Zaari, H. et al. "Comparative Study between Tb-Mbj and Gga+U on Magnetic and Optical Properties of Cdfe2o4." Journal of Magnetism and Magnetic Materials, vol. 393, 2015, pp. 183-187, doi:10.1016/j.jmmm.2015.05.032.

[28] John, R. and Padmavathi, S. "Ab Initio Calculations on Structural, Electronic and Optical Properties of ZnO in Wurtzite Phase" . *Crystal Structure Theory and Applications*, vol. 5, 2016, pp. 24-41. doi: 10.4236/csta.2016.52003.

[29] L. Vegard, "Die Konstitution der Mischkristalle und die Raumfüllung der Atome, " Zeitschrift für Physik a Hadrons and Nuclei, Vol. 5, 1921, pp. 17-26.

[30] Jaffe, John E. et al. "Lda and Gga Calculations for High-Pressure Phase Transitions in ZnO and MgO." Physical Review B, vol. 62, no. 3, 2000, pp. 1660-1665, doi:10.1103/PhysRevB.62.1660.

[31] A. S. Mohammadi, S. M. Baizaee and H. Salehi, "Density Functional Approach to Study Electronic Structure of ZnO Single Crystal," World Applied Sciences Journal, Vol. 14, No. 10, 2011, pp. 1530-1536.

[32] Rozale, H. et al. "A Theoretical Investigation of ZnO_xS_{1-X} Alloy Band Structure." physica status solidi (b), vol. 244, no. 5, 2007, pp. 1560-1566, doi:10.1002/pssb.200675147.

[33] Kisi, E. H. and M. M. Elcombe. "U Parameters for the Wurtzite Structure of ZnS and ZnO Using Powder Neutron Diffraction." Acta Crystallographica Section C Crystal Structure Communications, vol. 45, no. 12, 1989, pp. 1867-1870, doi:10.1107/s0108270189004269.

[34] Chowdhury, R. et al. "Optical Properties of Silicon Doped ZnO." Physica B: Condensed Matter, vol. 405, no. 23, 2010, pp. 4763-4767, doi:10.1016/j.physb.2010.08.072.

[35] Desgreniers, Serge et al. "Pressure-Induced Structural Changes in ZnS." Physical Review B, vol. 61, no. 13, 2000, pp. 8726-8733, doi:10.1103/PhysRevB.61.8726.

[36] K. Kihara, G. Donnay, " Anharmonic Thermal Vibrations in ZnO*." Canadian Mineralogist, vol. 23, 1985, pp. 647–654.

[37] Desgreniers, Serge. "High-Density Phases of ZnO: Structural and Compressive Parameters." Physical Review B, vol. 58, no. 21, 1998, pp. 14102-14105, doi:10.1103/PhysRevB.58.14102.

[38] Chang, E. and G. R. Barsch. "Pressure Dependence of Single Crystal Elastic Constants and Anharmonic Properties of Wurtzite." Journal of Physics and Chemistry of Solids, vol. 34, no. 9, 1973, pp. 1543-1563, doi:10.1016/s0022-3697(73)80226-4.

[39] Adil Es-Smairi, Nejma Fazouan, El Houssine Atmani, E. Maskar, Tuan V. Vu, D. P. Rai, International Journal of Quantum Chemistry, (2021). doi :10.22541/au.161907539.90276790/v1

[40] Hussain, Fayyaz et al. "An Insight of Mg Doped ZnO Thin Films: A Comparative Experimental and First-Principle Investigations." Physica E: Low-dimensional Systems and Nanostructures, vol. 115, 2020, doi:10.1016/j.physe.2019.113658.

[41] Khera, Ejaz Ahmad et al. "Structural, Electronic and Optical Properties of Transition Metal Doped $Hf_{1-x}TM_xO_2$ (Tm = Co, Ni and Zn) Using Modified TB-mBJ Potential for Optoelectronic Memristors Devices." Optik, vol. 212 (2020) 1. doi:10.1016/j.ijleo.2020.164677.

Chapter IV: Fabrication and characterization of ZnO:S thin films

Chapter IV

Fabrication and characterization of ZnO:S thin films

IV.1 Introduction

Zinc oxide (ZnO) is a binary compound material falling under the II-VI category, has gained recent prominence as a transparent conducting oxide (TCO) across diverse applications. Its noteworthy characteristics in this context include a broad energy band gap of approximately 3.37 eV, high visibility transparency at 85%, robust photoconductivity in the ultraviolet spectrum, efficient electron transportation facilitated by good electrical conductivity, and chemical stability that renders it suitable for prolonged use in varying environmental conditions. Additionally, the abundance of zinc as an element and the relatively low production cost of ZnO compared to alternative TCO materials contribute to its economic feasibility for large-scale applications.

Zinc sulfide (ZnS) stands out as a crucial semiconductor compound boasting impressive physical attributes, including a substantial band-gap energy of 3.7 eV at 300 K and a notable refractive index of 2.35 at 632 nm. Its versatility has led to exploration in diverse applications, with particular attention to its potential role in thin-film solar cells. In this context, ZnS is considered for deployment as a cadmium-free buffer layer, aiming to enhance the interface between the absorber layer and the transparent conductive layer, thereby contributing to improved performance in solar cell technology.

Zinc oxide (ZnO) and zinc sulfide (ZnS) films can be fabricated using various techniques, including molecular beam epitaxy [1,2], chemical vapor deposition [3,4], sputtering, thermal evaporation [5,6], spray pyrolysis [7,8], and chemical bath deposition (CBD) [9,10]. Notably, sol-gel spin coating [11, 12, 13, 14] has emerged as one of the most suitable methods for producing ZnO and ZnS thin films in the context of photovoltaic applications. This technique is preferred due to its efficiency, cost-effectiveness, and scalability for large-scale production.

The sol-gel (Solution-Gelation) deposition method is a widely recognized chemical pathway for crafting glass and ceramic materials. Researchers have long mastered this technique for synthesizing metal oxide thin films. The sol-gel process, a wet chemical

method, involves transforming molecular precursors into a nano-structured solid network through hydrolysis and condensation reactions. The progression of oxide networks includes the formation of a colloidal liquid known as sol, followed by the gelation of the sol to create a three-dimensional network within a continuous liquid phase, facilitating the production of fibers, powders, ceramics, and particularly thin films [15].

Throughout the sol-gel process, before gelation occurs, the colloidal solution obtained can be utilized for applying thin films via dip- or spin-coating. Spin-coating proves to be a swift and convenient method, particularly for the mass production of ZnO thin film coatings with high structural uniformity over extensive areas, typically ranging from a few nanometers. In essence, spin-coating involves uniformly coating the surface of a rotating substrate with a sol containing the desired materials, employing a well-defined rotational speed [15].

In this section of our thesis, we have chosen to focus on the production and analysis of ZnO thin films, both with and without sulfur doping (ZnO:S). Sulfur concentrations ranging from 0% to 100% were employed in this study using the Sol-Gel spin coating method. This chapter will comprehensively detail the materials, experimental conditions, and procedural steps essential for depositing these thin films on glass substrates via the sol-gel spin-coating technique. Following deposition, the structural, morphological, and optical characteristics of the thin films will be evaluated using X-ray diffraction (XRD), atomic force microscopy (AFM), and UV-Visible spectroscopy.

The optical transmission spectra will be analyzed to determine the absorption coefficient and gap energy of the samples. The obtained results will be thoroughly examined with a focus on their potential applications in solar cell technology.

IV.2 Starting materials and thin films fabrication

For the fabrication of ZnO thin films, whether pure or Sulfur doped, we have chosen the sol-gel spin-coating method, which known to be one of the most straightforward, efficient, and cost-effective chemical techniques available. This section will cover in more detail the empiricist and technical specifications for preparing the sol-gel spin-coating of pure or sulfur-doped ZnO thin films onto glass substrates, and how to subject them to curing and annealing processes.

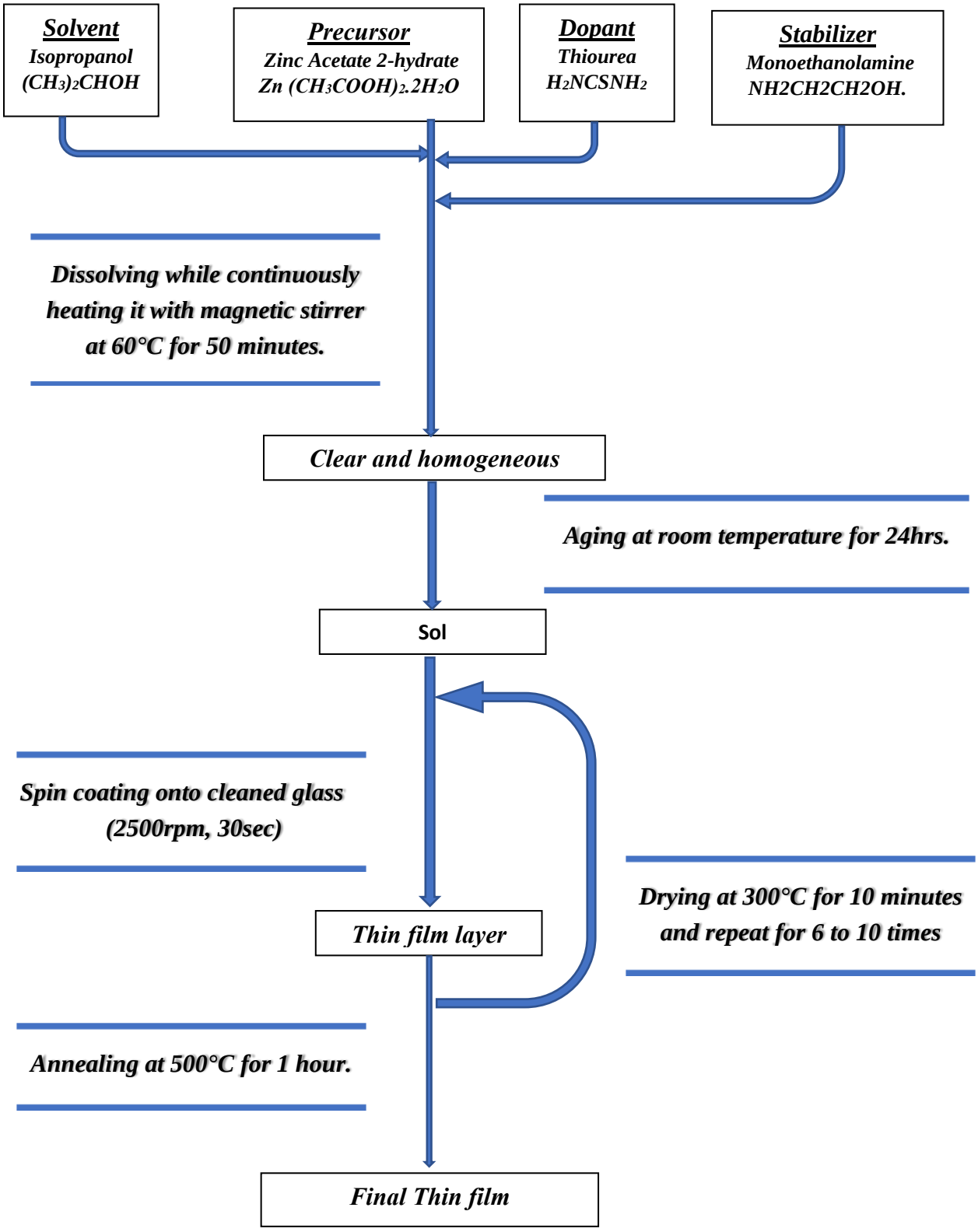

Fig. IV.1: Deposition of Sulfur-doped ZnO thin films using spin-coating technique.

The spin-coating process can be broken down into three main steps:

- Preparing the precursor sol;
- Depositing the film onto a rotating glass substrate;

- Applying heating treatment (including drying and annealing) to achieve the desired film.

Fig. IV.1 provides the flowchart of pure and Sulfur-doped ZnO thin films, using Sol-Gel spin-coating method, following the hereinbefore three steps.

IV.2.1 Starting materials

- **The precursor [Zinc Acetate 2-hydrate]**
  - Formula: Zn (CH3COOH)2.2H2O .
  - Form: Solid.
  - Color : White
  - Molecular Weight: 219.49 g/mol.
  - Density: 1.74 g/cm^3.
  - Solubility in Water: 430 g/l at 20 °C.
- **The stabilizer [Monoethanolamine]**
  - Formula: $NH_2CH_2CH_2OH$.
  - Form: liquid.
  - Color: yellow.
  - Molecular Weight: 61.08 g/mol.
  - Density: 1.01 g/cm^3.
- **The solvent [Isopropanol]**
  - Formula: $(CH3)_2CHOH$.
  - Form: Liquid.
  - Color: Colorless.
  - Molecular Weight: 60.1 g/mol.
  - Density: 0.786 g/cm3.
- **Source of sulfur dopant [Thiourea]**
  - Formula: H2NCSNH2
  - Form: Solid.
  - Color: White.
  - Molecular Weight : 76.12 g/mol.
  - Density: 1.4 g/cm3.
  - Solubility in Water: 117.5 at 20 °C

IV.2.2 Preparation of precursor solution

Table IV.1 summarizes the weights and concentrations of all materials used to prepare different solutions needed for synthesizing the pure and S-doped ZnO thin films (2, 4 and 8%).

Table IV.1 Materials weights and concentrations.

	Pure ZnO	**2%**	**4%**	**8%**
Molarity of ZnO solution [mol/L]	0.6	0.6	0.6	0.6
Mass of Zinc Acetate [g]	1.317	1.308	1.299	1.280
Mass of Thiourea [g]	0	0.009	0.018	0.0365
MEA Volume[mL]	0.363	0.363	0.363	0.363
Isopropanol Volume [mL]	8.880	8.879	8.878	8.8753
Final solution volume (mL)	10	10	10	10

- **For ZnO material**

To prepare the precursor solution, zinc acetate 2-hydrate [$Zn(CH_3COO)_2.2H_2O$] was utilized, along with Monoethanolamine [MEA: $NH_2CH_2CH_2OH$] and Isopropanol [2Propanol: $CH_3CH(OH)CH_3$] as stabilizer and solvent, respectively. The procedure involved dissolving zinc acetate dehydrate in isopropanol and continuously heating it with magnetic stirrer at a fixed temperature of 60°C for 50 minutes, to obtain a pure ZnO film with a concentration of Zn metal ions at 0.6 mol/L. Next, MEA was added drop-by-drop to the alcoholic solution and continuously heated with magnetic stirrer for 2 hours at the same temperature, while maintaining the molar ratio of MEA to metal ions at 1.0. The clear and colorless solution was then kept for aging at room temperature for 24 hours [1].

- **For Sulfur-doped ZnO materials**

To obtain S-doped ZnO (ZnO:S) thin films, we followed the same steps as described in paragraph hereinabove, but with the use of Thiourea [NH_2CSNH_2] as the source of sulfur dopant. The percentage of dopant was determined by the S/(S+Zn) ratio, with values of 2, 4,

and 8 mol%. The Zn and S metal ion concentrations in the doped mixture solutions were both at a concentration of 0.5 mol/L.

- **For ZnS material**

In the synthesis of pure ZnS thin film, zinc acetate and thiourea were utilized as precursor sources for Zn and S, respectively. To create the sol, 1M concentrations of zinc acetate and thiourea were dissolved in Isopropanol and then refluxed at 60°C while stirring (see Fig. IV.2). After gelation occurred, the resulting transparent pale-yellow homogeneous sol was left overnight at room temperature. This methodology was the same as that reported in [14].

Fig. IV.2: Solution refluxing and stirring at 60°C.

IV.2.3 Preparation of the glass substrates

To ensure consistent films quality and prevent yield loss, it is important to address surface contamination in glass substrates. This involves the removal of unwanted particles and chemicals from the substrate's surface. To achieve this, a process of sequential cleaning in acetone and deionized water at 40°C for 5 minutes using an ultrasonic cleaning machine is required (see Fig. IV.3), followed by drying with hot air from a blower. This process helps to maintain substrate homogeneity and improve film quality.

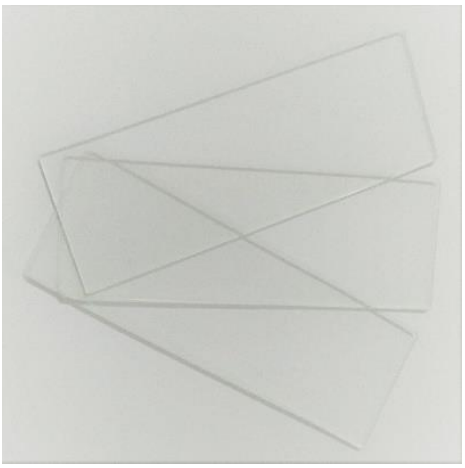

(b) **(a)**

Fig. IV.3: (a) Glass substrates & (b) ultrasonic cleaning bath FB15051.

IV.2.4 Thin film deposition

The gel was spin-coated onto cleaned glass substrates using the homemade spin-coater shown in Fig. IV.4. At a fixed rotation speed of 2500 rpm for 60 seconds, the coated samples were dried and heated on a hot plate (see Fig. IV.5). The films were deposited at 300°C for 10 minutes after each layer. This process was repeated 10 times to achieve the desired film thickness.

Fig. IV.4: Spin-coating system used to deposit S-doped ZnO samples.

Fig. IV.5: Hot plate used to dry the obtained samples.

IV.2.5 Annealing process of spin-coated S-doped ZnO thin films

The films were annealed in an open furnace (under air ambiance) (see Fig. IV.6) at 500°C for 45 minutes to ensure complete solvent evaporation and provide good crystallinity.

Fig. IV.6: Carbolite high-temperature tube Furnace used to anneal the S-doped ZnO obtained samples.

The structural, morphological, electrical and optical properties were accurately acquired using the characterisation devices mentioned in the introduction. The obtained measurements and results are presented through the included tables and figures hereinafter to be completely analyzed, discussed and assessed.

IV.3 Characterization of ZnO, Sulfure-doped ZnO and ZnS thin films

IV.3.1 Structural characterization with X-ray diffraction

X-ray diffraction (XRD) is a widely used technique for structural characterization of materials, including thin films. The XRD method relies on the interaction of X-rays with the crystal lattice of a material, leading to the diffraction of X-rays at specific angles. This diffraction pattern provides information about the crystal structure, lattice parameters, and orientation of the crystals within the material.

At first, to investigate thin-film material quality, it is essential to measure the change in the crystal structural and its properties of the material of interest. One useful method for evaluating the crystalline quality of fabricated sample is the X-ray diffraction. This technique is non-destructive and straightforward and enables the identification of different phases, evaluation of texture, average crystallite size, internal stress, and distribution of phases in the sample. X-rays are electromagnetic waves with wavelengths (0.5-50 Å) comparable to atomic separation distances. As they pass through a crystal, they interact with the lattice and diffract according to Bragg's law expressed by equation (IV.1), which describes the relationship between the distance (d_{hkl}) separating two parallel crystal planes (the atomic spacing of the crystal lattice), wavelength (λ) of X-rays and diffraction angle (θ) [17]:

$$2d_{hkl}\sin(\theta) = n\lambda \qquad \text{(IV.1)}$$

where n is the order of diffraction (usually n = 1).

During X-ray diffraction, a counter tube detects the diffracted radiation and moves across the angular range of reflections, in which the resulting intensities are recorded by a computer system. These data are then compared with the Joint Committee Power Diffraction Standards (JCPDS) to identify the sample of interest. Using all diffraction peaks of recorded XRD spectrum, it will be easy to indicate the crystalline nature of sample by comparing them to existed JCPDS data.

To get a clear view and more details about crystallization, the lattice constants ‘c’ and ‘a’, texture coefficient (TC), average crystallite size (D), micro-strain (δ) and dislocations density (δ) measurements should be involved in the investigation.

The **‘c’ and ‘a’** lattice constant of the film are calculated from [18]:

$$\frac{1}{(d_{hkl})^2} = \frac{4}{3}\left[\frac{h^2 + hk + k^2}{a^2}\right] + \frac{l^2}{c^2} \quad \text{(IV.2)}$$

where $dhkl$ – inter-reticular distance; hkl – Miller indices; a, c – Lattice parameters (constants) of the hexagonal crystal.

Using (100) and (002) diffraction peaks of recoded XRD spectra, it can be determined the lattice parameters (a) and (c) as [18]:

$$a = \frac{\lambda}{\sqrt{3}\sin(\theta_{100})}(\text{Å}) \quad \text{(IV.3)}$$

$$c = \frac{\lambda}{\sin(\theta_{002})}(\text{Å}) \quad \text{(IV.4)}$$

The lattice parameters (a) and (c) of pure ZnO are found to be: ***a = 3.231274108 Å*** and ***c = 5.17810904 Å***, in good agreement with values reported in the literature [19].

The texture coefficient (TC) illustrates the preferred orientation of the crystals in films in comparison with the chosen (JCPDS) intensity and is calculated for all samples using significant (hkl) planes through the relation (4.5) [18]:

$$TC_{hkl} = \frac{I(hkl)/I_0(hkl)}{\frac{1}{n}\sum_1^n I(hkl)/I_0(hkl)} \quad \text{(IV.5)}$$

where TC_{hkl} – Texture coefficient of (hkl) plane; (hkl) – Measured intensity of (hkl) plane obtained from the film; $I_0(hkl)$ – Standard intensity (JCPDS data card 00-036-1451); n – Number of diffraction peaks taken into account.

TC_{hkl} value of unity represents the plane without preferred orientation, whereas TC_{hkl} values higher than unity indicates the abundance of crystallites in a given (hkl) direction.

To estimate ***the average crystallite size (D)*** of the samples, ***Scherrer's formula*** is applied, which involves calculating the full width at half maximum (FWHM) of the most intense diffraction peaks using the relation (IV.6) [20]:

$$D = \frac{k\lambda}{\beta\cos(\theta)} \quad \text{(IV.6)}$$

where D – The crystallite size (nm or Å); K – The Scherrer constant (0.87- 1); λ – The wavelength of X-ray (λ = 1.54056 Å for $CuK\alpha$); β – The full width at half maxima of the peak (FWHM) in radians; θ – The Bragg's angle (Rad).

The ***micro-strain (ε)*** is calculated according to the approach of Williamson and Smallman [21]:

$$\varepsilon = \frac{\beta \cos(\theta)}{4} \tag{IV.7}$$

We can calculate the ***dislocations density (δ)*** using the crystallite size values according to the approach of Williamson and Smallman [21]:

$$\delta = \frac{1}{D^2} \tag{IV.8}$$

IV.3.2 Crystallography of undoped, Sulfur-doped ZnO and ZnS thin films

All spin-coated samples were investigated by powder X-ray diffraction spectroscopy (XRD) using a Philips spectrophotometer equipped with CuKα radiation (λ=0.15406 nm). The recorded XRD spectra and their calculated parameters of crystal structures of pure ZnO and Sulfur-doped ZnO thin films spin-coated with 2%, 4% and 8% of Sulfur doping are provided by Fig. IV.7 and Table IV.2, respectively. While the XRD spectrum of spin-coated ZnS film and their calculated parameters of crystal structures are provided by Fig. IV.8 and Table IV.2, respectively. The hereinafter paragraphs provide discussions regarding the XRD data of pure ZnO and Sulfur-doped ZnO in the first place, and then the discussion regarding the XRD of ZnS film will be presented next.

a) Crystallographic studies of pure ZnO and Sulfur-doped ZnO thin films

Fig. IV.7 shows the XRD spectra of pure ZnO and Sulfur-doped ZnO films spin-coated with various Sulfur amounts (2%, 4% and 8%) in angular diffraction of (2θ) between 25° to 75°. Where, the pure ZnO, ZnO:S(2%), ZnO:S(4%) and ZnO:S(8%) spectra showed the presence of same diffraction peaks, with different intensities, for all spin-coated films, corresponding to the (100), (002), (101), (102), (110), (103) and (112) planes, demonstrating that the spin-coated films were polycrystalline in nature and they crystallized according to the hexagonal wurtzite structure with the $P6_{3mc}$ space group, as shown in Fig. IV.9 (JCPDS card no. 36-1451) [22,23]. Even with S amount of 8%, no evidence of impurity or formation of unexpected phase (S, Zn, ZnS) was detected.

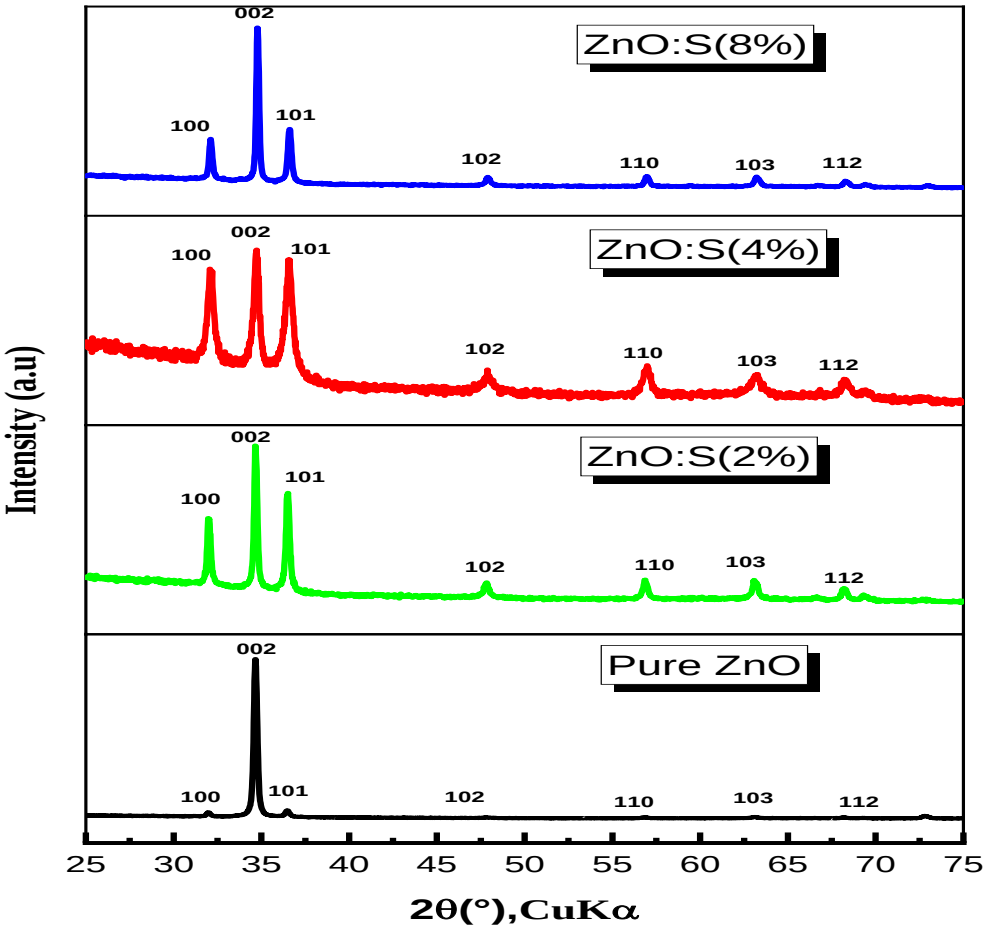

Fig. IV.7: X-Ray Diffraction patterns for pure and Sulfur-doped ZnO (2%, 4% & 8%).

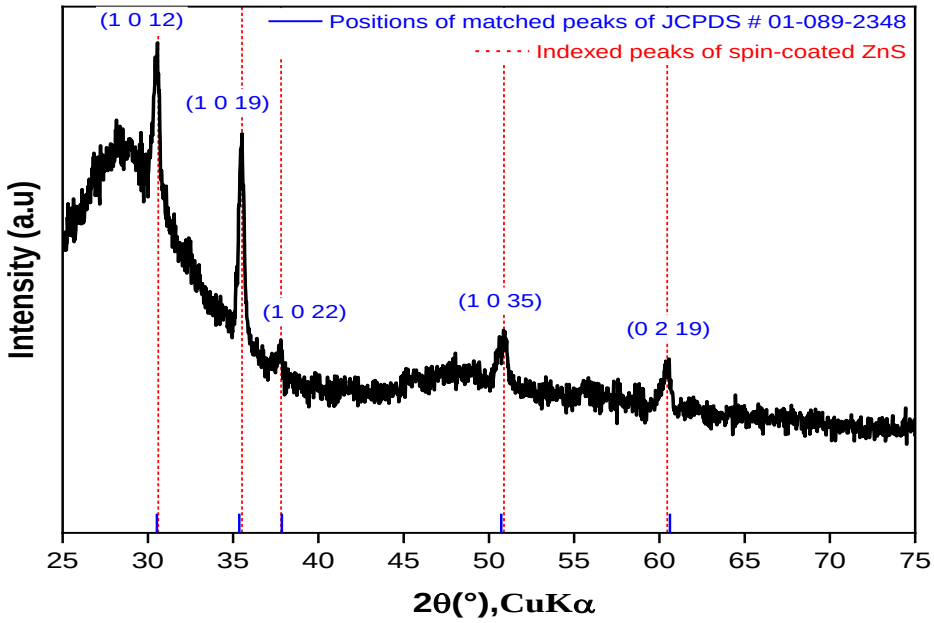

Fig. IV.8: X-Ray Diffraction pattern of ZnS sample.

Table IV.2: XRD computing data of ZnS, pure ZnO and ZnO:S (for 2%, 4% & 8%).

Sample		**Pure ZnO**	**ZnO:S (2%)**	**ZnO:S (4%)**	**ZnO:S (8%)**	**ZnS**
2θ (°) of intense peak		$34.6167_{(002)}$	$34.6179_{(002)}$	$34.6744_{(002)}$	$34.4557_{(002)}$	$35.5151_{(1019)}$
TC_{hkl}	(100)	0.0744	0.6657	0.8426	0.4845	-
	(002)	2.8061	1.3879	1.1178	1.8701	-
	(101)	0.1195	0.9463	1.0396	0.6454	-
	(1012)	-	-	-	-	1.6814
	(1019)	-	-	-	-	2.1270
	(1035)	-	-	-	-	0.5115
Crystallite Size D (nm)		38.4336	46.9842	42.2875	49.5074	42.49
Cell Parameters (Å)	a=b	3.2313	3.2309	3.2177	3.2501	3.823
	C	5.1781	5.1779	5.1698	5.2016	74.976
	c/a	1.6025	1.6026	1.6066	1.6004	19.6118
Micro-Strain $\varepsilon*10^{-3}$		2.91	2.36	2.67	2.37	4.35
Dislocation Densities $\delta*10^{15}$		0.6769	0.4529	0.5592	0.4079	0.5539
Root mean square roughness R (nm)		46.3	8.63	46.6	13.1	0.388

Reviewing the TC values in Table IV.2 and the high intensity of (002) peak in Fig. IV.7, it is found that all pure ZnO, ZnO:S(2%), ZnO:S(4%) and ZnO:S(8%) samples took the (002) as preferential growth plane especially for the spin-coated pure ZnO film, while the ZnO:S(8%) film showed a shifting to lower angles. All other films showed a tendency to shift to higher angles (Fig. IV.7). This shifting behavior demonstrates a modification in the lattice structure in all films that confirms the successful insertion of S dopant in crystal structure of spin-coated ZnO films with S doping of 2%, 4% and 8%. The notable difference in ionic radii between 1.38 Å of O^{2-} and 1.48 Å of S^{2-} caused the stretching modification in the ZnO crystal structure, where O^{2-} replaced by S^{2-} throughout the ZnO structure, causing

changes in cell parameters a and c, as shown in Table IV.2. In terms of XRD intensity, Fig. IV.7 showed a growing behaviour of peaks in all doped films with S, especially at (100) and (101), compared to the spin-coated pure ZnO film. Once again, the (002) peak witnessed a slight increase in intensity at 2% of S doping, then decreased to lower value at 4% of S doping, to increase further at 8% of S doping.

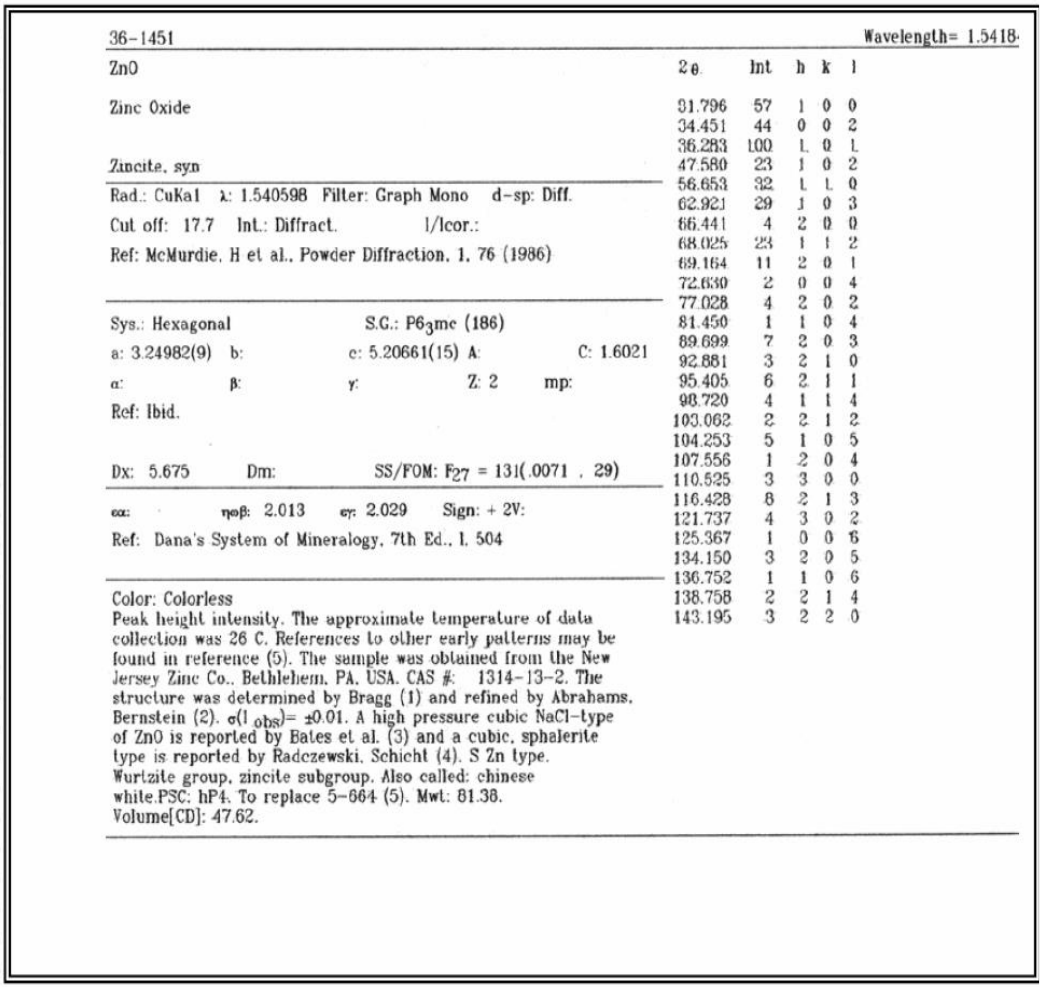

36-1451 Wavelength= 1.5418

ZnO

Zinc Oxide

Zincite, syn

Rad.: CuKa1 λ: 1.540598 Filter: Graph Mono d-sp: Diff.

Cut off: 17.7 Int.: Diffract. I/Icor.:

Ref: McMurdie, H et al., Powder Diffraction, 1, 76 (1986)

Sys.: Hexagonal S.G.: $P6_3mc$ (186)

a: 3.24982(9) b: c: 5.20661(15) A: C: 1.6021

α: β: γ: Z: 2 mp:

Ref: Ibid.

Dx: 5.675 Dm: SS/FOM: F_{27} = 131(.0071 , 29)

ωα: ηωβ: 2.013 εγ: 2.029 Sign: + 2V:

Ref: Dana's System of Mineralogy, 7th Ed., I, 504

Color: Colorless

Peak height intensity. The approximate temperature of data collection was 26 C. References to other early patterns may be found in reference (5). The sample was obtained from the New Jersey Zinc Co., Bethlehem, PA, USA. CAS #: 1314-13-2. The structure was determined by Bragg (1) and refined by Abrahams, Bernstein (2). $\sigma(I_{obs})$= ±0.01. A high pressure cubic NaCl-type of ZnO is reported by Bates et al. (3) and a cubic, sphalerite type is reported by Radczewski, Schicht (4). S Zn type. Wurtzite group, zincite subgroup. Also called: chinese white.PSC: hP4. To replace 5-664 (5). Mwt: 81.38. Volume[CD]: 47.62.

2θ	Int	h	k	l
31.796	57	1	0	0
34.451	44	0	0	2
36.283	100	1	0	1
47.580	23	1	0	2
56.653	32	1	1	0
62.921	29	1	0	3
66.441	4	2	0	0
68.025	23	1	1	2
69.164	11	2	0	1
72.630	2	0	0	4
77.028	4	2	0	2
81.450	1	1	0	4
89.699	7	2	0	3
92.881	3	2	1	0
95.405	6	2	1	1
98.720	4	1	1	4
103.062	2	2	1	2
104.253	5	1	0	5
107.556	1	2	0	4
110.525	3	3	0	0
116.428	8	2	1	3
121.737	4	3	0	2
125.367	1	0	0	6
134.150	3	2	0	5
136.752	1	1	0	6
138.758	2	2	1	4
143.195	3	2	2	0

Fig. IV.9: JCPDS card n° 36-1451 for Zinc Oxide (ZnO).

Regarding the average crystallite size (D), the most intense peak (002) was considered in calculation concerning the pure ZnO thin film, while all (100), (002) and (101) intense peaks were considered in calculation concerning spin-coated Sulfur-doped ZnO films. As represented in Table IV.2, the crystallite size values showed an increase from 38.43 nm for pure ZnO film to the range of 42.29 to 49.51 for S-doped ZnO films. This considered increase is due to the replacement of O by S dopants, which results volume increase in the lattice of wurtzite structure because of the outmatch of S^{-2} ion in radius compared to radius of O^{2-}. While the micro-strain values (Table IV.2) show a considered decrease for S-doped

ZnO films compared to the pure ZnO film, indicating that the range atomic order of lattice structures of doped films becomes more stable. While the dislocations density values (Table IV.2) show a considered decrease in the range from 17.4% to 39.7% compared to the spin-coated pure ZnO film indicating the level decrease of defection that occurs in the structure of spin-coated S-doped ZnO films because of S dopants.

b) Crystallographic study of ZnS thin film

Fig. IV.8 shows the XRD spectrum of spin-coated ZnS thin film, annealed at 500°C in angular furnace, the diffraction angles (2θ) were fixed between 25° to 75°. The pattern of this spectrum showed the presence of diffraction peaks corresponding to (1012), (1019), (1022), (1035) and (0219) planes, at angular locations 2θ of about 30.61°, 35.51°, 37.81°, 50.88 and 60.46° demonstrating that the obtained film was polycrystalline in nature and they crystallized according to the hexagonal structure with the P3m1 space group, as shown in Fig. IV.10 (JCPDS card no. 01-089-2348).

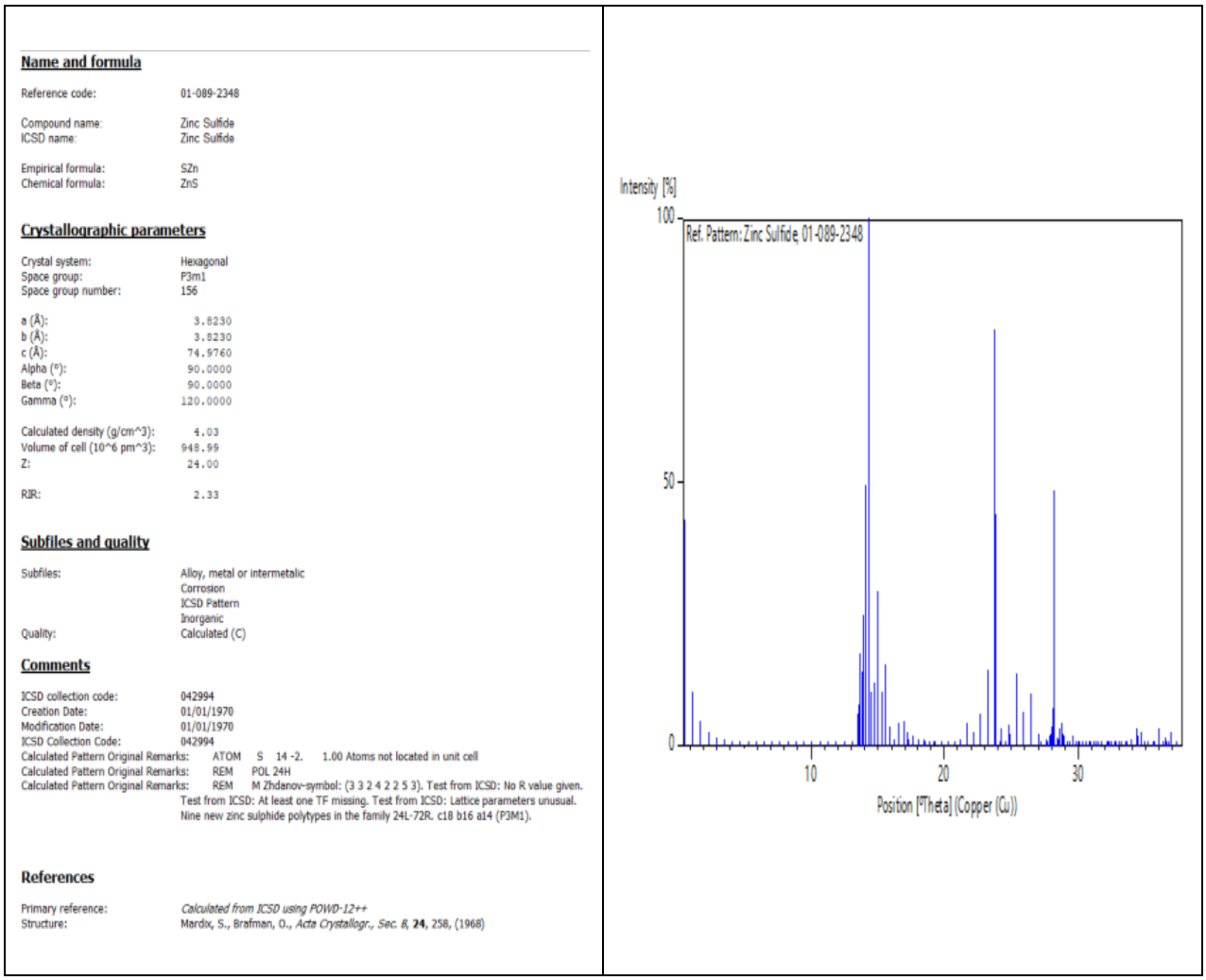

Name and formula

Reference code:	01-089-2348
Compound name:	Zinc Sulfide
ICSD name:	Zinc Sulfide
Empirical formula:	SZn
Chemical formula:	ZnS

Crystallographic parameters

Crystal system:	Hexagonal
Space group:	P3m1
Space group number:	156
a (Å):	3.8230
b (Å):	3.8230
c (Å):	74.9760
Alpha (°):	90.0000
Beta (°):	90.0000
Gamma (°):	120.0000
Calculated density (g/cm^3):	4.03
Volume of cell (10^6 pm^3):	948.99
Z:	24.00
RIR:	2.33

Subfiles and quality

Subfiles:	Alloy, metal or intermetalic Corrosion ICSD Pattern Inorganic
Quality:	Calculated (C)

Comments

ICSD collection code:	042994
Creation Date:	01/01/1970
Modification Date:	01/01/1970
ICSD Collection Code:	042994
Calculated Pattern Original Remarks:	ATOM S 14 -2. 1.00 Atoms not located in unit cell
Calculated Pattern Original Remarks:	REM POL 24H
Calculated Pattern Original Remarks:	REM M Zhdanov-symbol: (3 3 2 4 2 2 5 3). Test from ICSD: No R value given. Test from ICSD: At least one TF missing. Test from ICSD: Lattice parameters unusual. Nine new zinc sulphide polytypes in the family 24L-72R. c18 b16 a14 (P3M1).

References

Primary reference:	*Calculated from ICSD using POWD-12++*
Structure:	Mardix, S., Brafman, O., *Acta Crystallogr., Sec. B*, **24**, 258, (1968)

Fig. IV.10: JCPDS card n° 01-089-2348 for Zinc Sulfide (ZnS).

The intense and broad peaks in the ZnS diffraction pattern indicate good crystallization and formation of crystals with size of 42.49 nm. No evidence of impurity or formation of unexpected phase other than hexagonal phase ZnS was detected. The highly intense (1012) and (1019) peaks slightly shifted towards higher Bragg angles compared to the matched peaks of 01-089-2348 JCPDS card, indicating slight change in crystal size with cell parameters a = b = 3.823 Å and c = 74.976 Å. The ZnS micro-strain value of 4.35×10^{-3} (Table IV.2) shows a considered change in the range atomic order of its lattice structure compared to the pure and S-doped ZnO films. While the dislocations density value (Table IV.2) shows a decrease of 39.7% compared to the pure ZnO film indicating the level decrease of defection that occurs in the structure of ZnS film because of S and Zn binary composition.

IV.4 Morphological Study by Atomic Force Microscopy

Fig. IV.11 shows the Two- and Three-dimensions AFM graphs in a 1 μm^2 scan area of the surface profile for the spin-coated pure ZnO, ZnO:S(2%), ZnO:S(4%), ZnO:S(8%) and ZnS films onto glass substrates. It is observed that there is a significant change in morphology of the films surfaces as S-dopant amount increased. All undoped and S-doped ZnO surfaces had a topographic sinuosity involves uniform grains in size and without any cracks or pores. Generally, the increase of S doping produced surfaces with lower sinuosity (rheology) and large grain size compared to surfaces of pure ZnO. The AFM images of ZnO:S(4%) sample shown in Fig. IV.11 is not consistent with the behavior of others S-doped ZnO films, where its morphology is textured of large grains, which may be caused by the coalescence of small ZnO crystallites (~ 42.79 nm) due to normal-condition of spin-coating. Where, this coalescence resulted in a roughness surface with value of 46.6 nm, which is almost equal to the roughness 46.3 nm of pure ZnO. While other ZnO:S(2%) and ZnO:S(8%) showed small roughness of 8.63 nm and 13.1 nm, respectively. In addition, the very small roughness of 0.388 nm of spin-coated ZnS film confirms that the introduction of S element into the composition produces smooth surfaces.

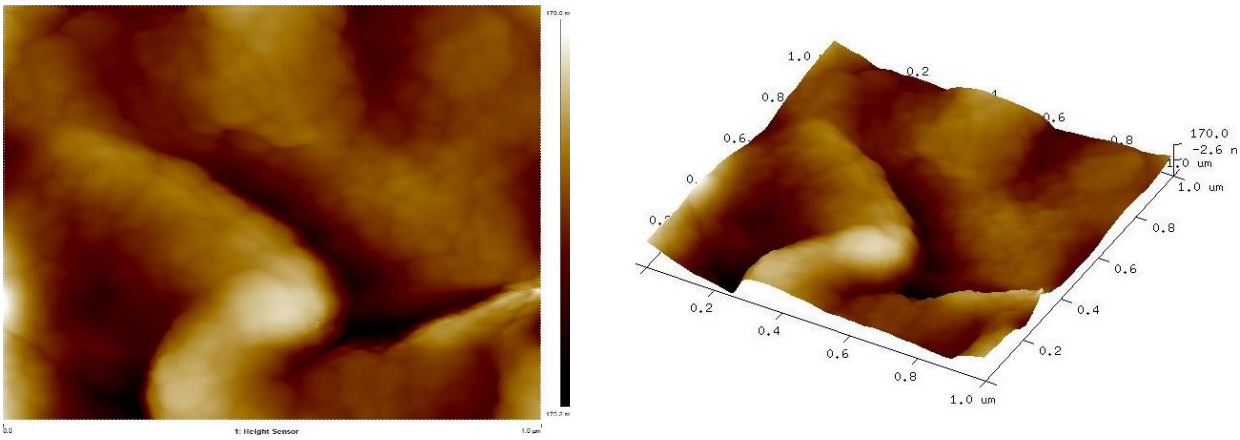

Pure ZnO

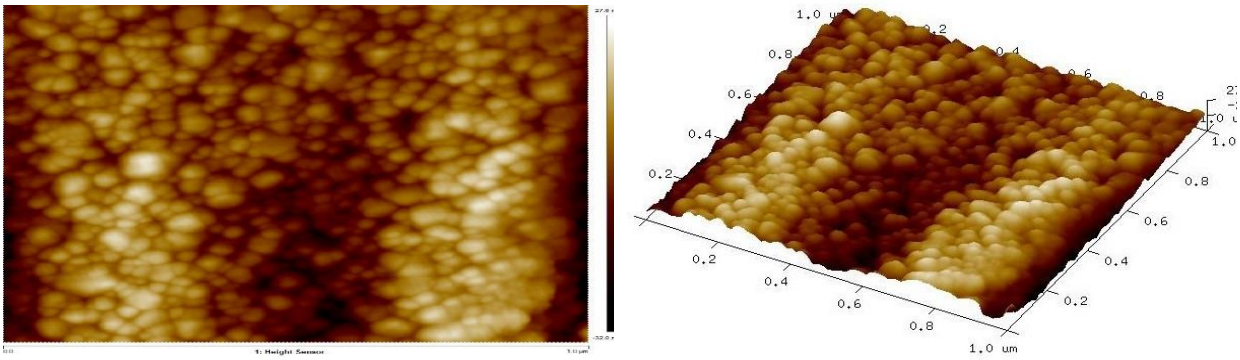

ZnO:S(2%)

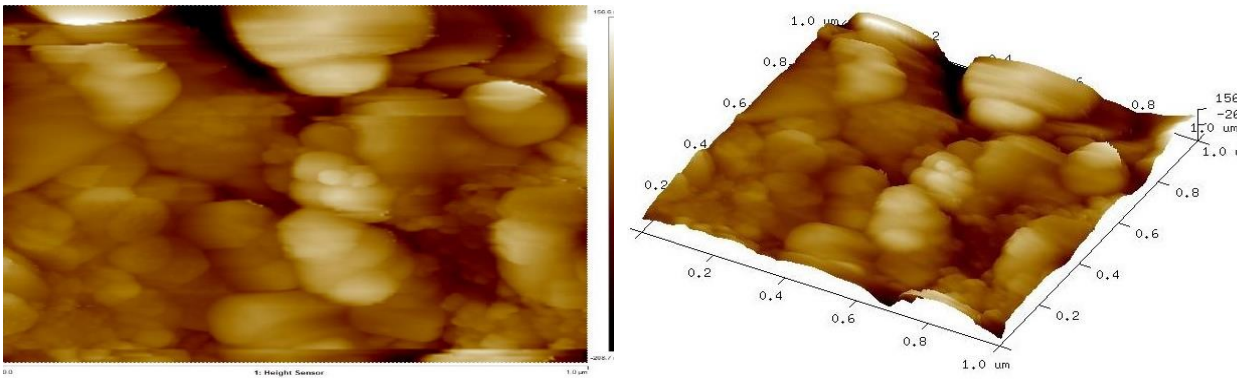

ZnO:S(4%)

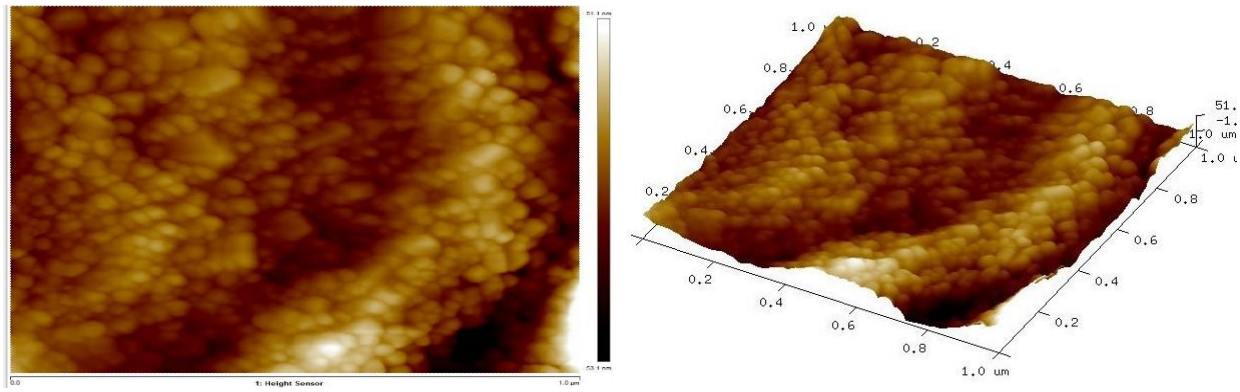

ZnO:S(8%)

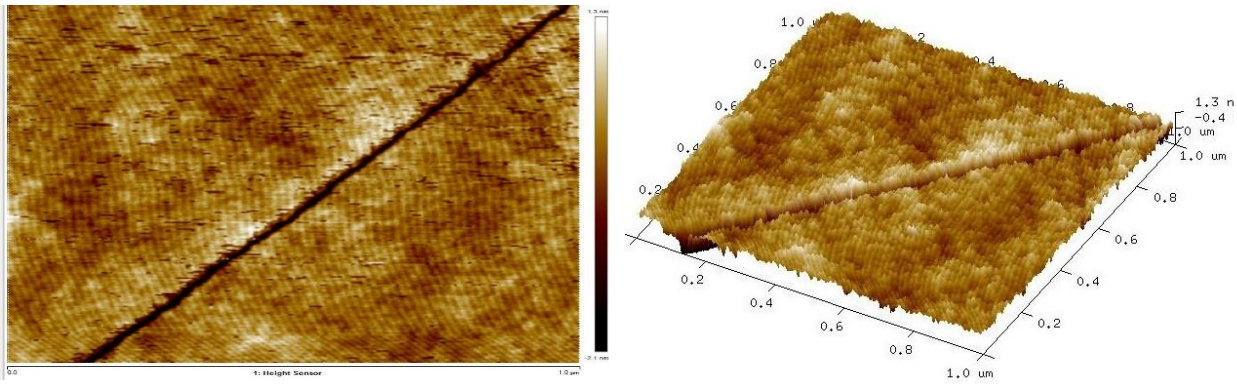

ZnS

Fig. IV.11: 2D- and 3D-AFM images of ZnS, pure ZnO and ZnO:S (2%, 4% & 8%).

IV.5 Optical study of Pure ZnO, Sulfur-doped ZnO thin films

IV.5.1 Transmittance

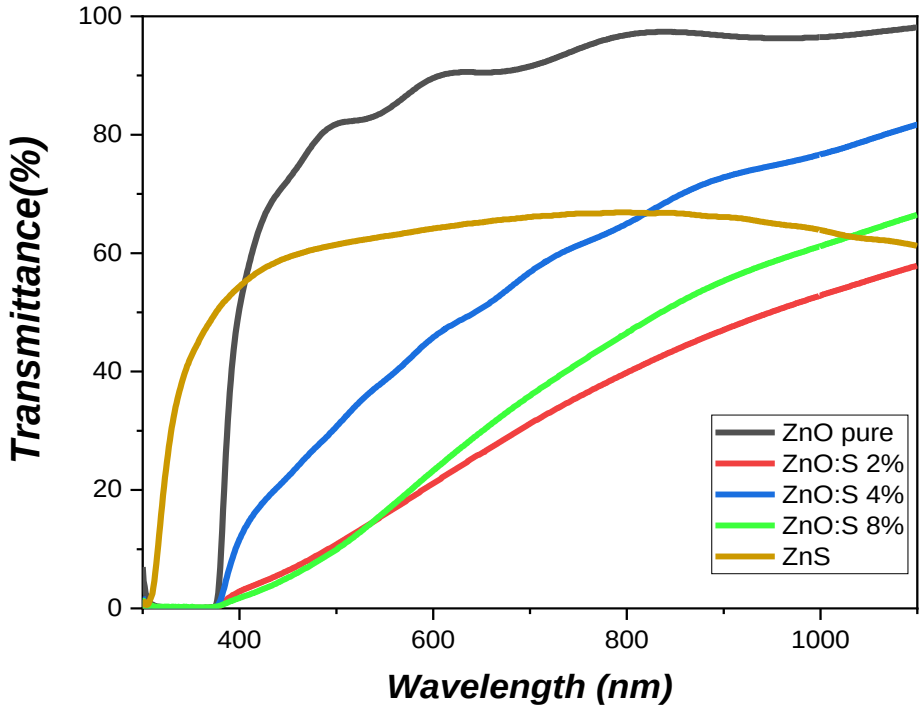

Fig. IV.12: Optical transmittance spectra of ZnS, pure ZnO and ZnO:S (2%, 4% & 8%).

Fig IV.12 depicts the transmittance spectra quarried through the UV-Visible spectroscopy device in the wavelength scan from 300 nm to 1100 nm for the spin-coated pure ZnO, ZnO:S(2%), ZnO:S(4%), ZnO:S(8%) and ZnS thin films. All S-doped ZnO films showed considered decrease in transparency compared to the pure ZnO demonstrating the increase of thickness of all S-doped ZnO films compared to the thickness of pure ZnO.

The ZnS film showed a transparency above 60% along the entire wavelength scan indicating that the spin-coated ZnS has a good crystallinity and weak defect density near the band edge.

IV.5.2 Absorbance

The absorbance spectra against wavelength from 300 to 1100 nm is calculated and presented in Fig. IV.13 for all spin-coated pure ZnO, S-doped ZnO and ZnS thin films. It is observed that the S doping increases the absorption in the short wavelength region for ZnO:S(8%) film compared to absorption (almost close to 0) of pure ZnO film; however, in the ultraviolet this absorption decreased with increasing of wavelength. The absorption of spin-coated ZnS film was almost constant along the scanned wavelength range and lied above the pure ZnO and down all S-doped ZnO films. The increase of absorption confirms the increase of films thicknesses due to the S dopants.

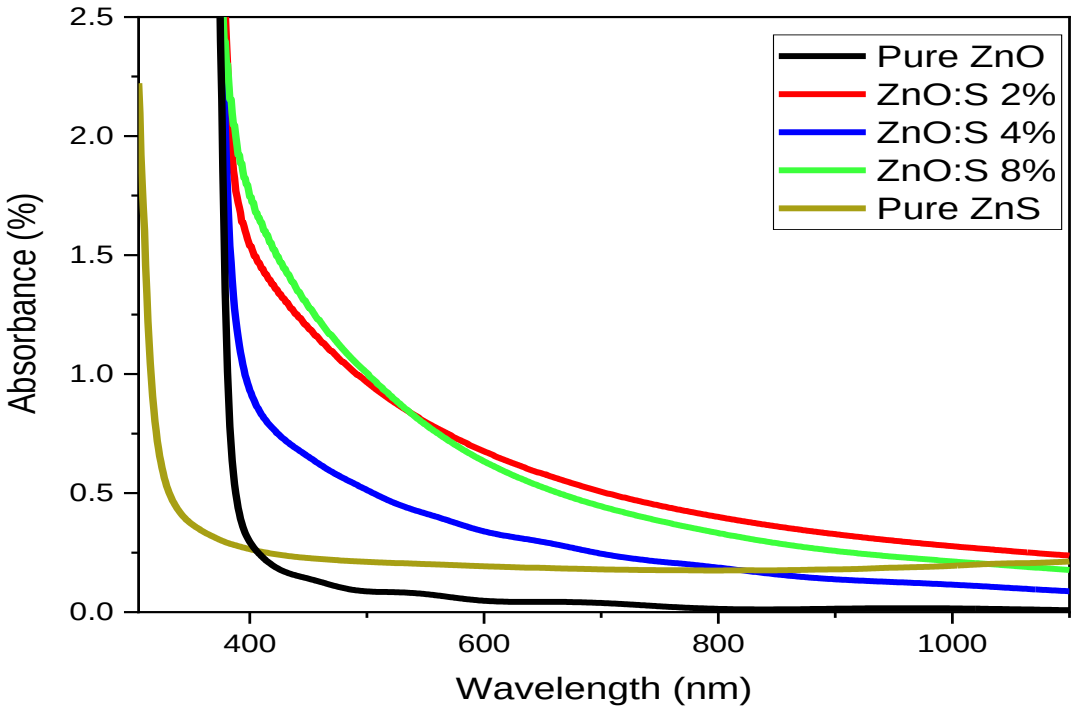

Fig. IV.13: Optical absorption spectra of ZnS, pure ZnO and ZnO:S (2%, 4% & 8%).

IV.5.3 Determination of optical band gaps

By relating the ($h\nu$) incident photon energy, (α) absorption coefficient and (E_g) band gap of the materials, the Tauc law [24] can be described as following:

$$\alpha h\eta = k(h\eta - E_g)^n \qquad \text{(IV.7)}$$

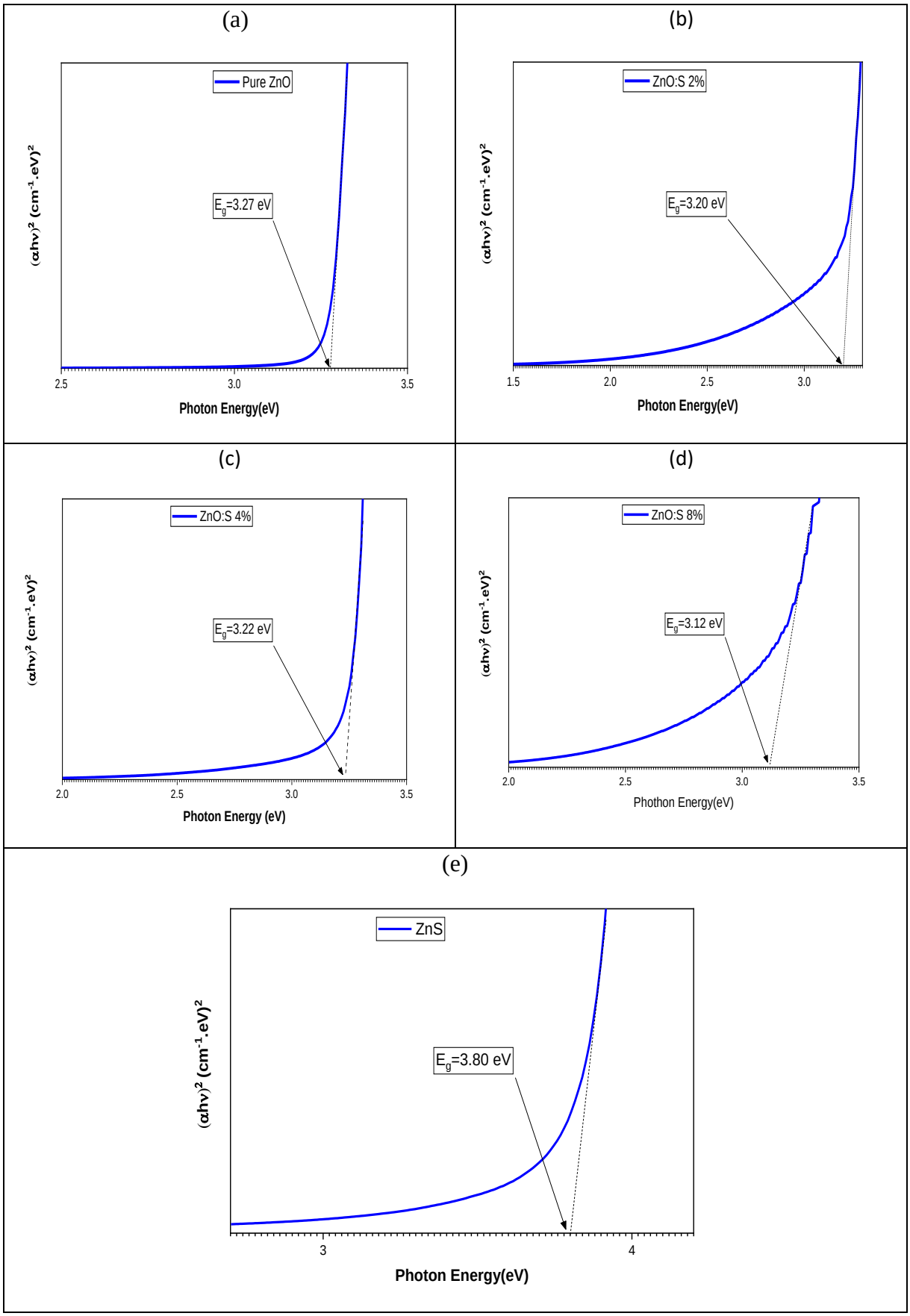

Fig. IV.14: Optical band gaps of (a) pure ZnO, (b) ZnO:S(2%), (c) ZnO:S(4%), (d) ZnO:S(8%) and (e) ZnS thin films.

where: α – Absorption coefficient; h – Plank's constant; η – Frequency of radiation; Eg – Optical band gap; K – Edge width parameter; n – characterizes the optical type of transition and takes the values 2, 1/2 (2 for allowed direct transitions or 1/2 for allowed indirect transitions) [25].

For pure ZnO and ZnS materials, the forbidden gap is a direct optical band, which can be described by plotting $(\alpha h\upsilon)^2$ vs $(h\upsilon)$ graph, as shown by the bluish curves in Fig. IV.14. In order to determine, the E_g optical band gaps for each material, the straight-line portion is extrapolated of the bluish curves to the $h\upsilon$ axis. The obtained E_g values are shown in Fig. IV.14.

The estimated band gaps of ZnO, ZnO:S(2%), ZnO:S(4%) and ZnO:S(8%) (see Fig. IV.13 (a-d)) are: 3.27, 3.20, 3.22 and 3.12 eV, respectively. These obtained band gaps showed a decrease for all spin-coated S-doped ZnO films compared to the band gap of pure ZnO oxide demonstrating that the S doping have an effect on the ZnO absorbance [26]. While the optical band gap of spin-coated ZnS film showed a value of 3.8 eV, which is confirmed for the wurtzite ZnS by various reported work [27].

IV.6 Conclusion

This chapter has focused on the fabrication of pure ZnO, Sulfur-doped ZnO, and ZnS thin films through Sol-Gel spin-coating method. The band gap of the ZnO film, deposited through spin-coating, measured as 3.27 eV, aligning closely with the reported value for the hexagonal ZnO structure [28]. While all spin-coated Sulfur-doped ZnO (2%, 4% and 8%) thin films showed the same hexagonal wurtzite structure, they showed large crystallite size in the range of 42.2875 to 49.5074 nm compared to the small size (38.43 nm) of pure ZnO crystals. In addition, the spin-coated ZnS film showed a hexagonal structure with crystallite size of 42.49 nm demonstrating that the introduction of S element through the spin-coating process causes an increase of crystals size within the structure of binary compounds of Zn, O and S elements. The S dopants had an effect on the morphology of spin-coated ZnO film and S-doped ZnO thin films, especially on their roughness, which were 46.3, 8.63, 46.6, 13.1 nm for pure ZnO, ZnO:S(2%), ZnO:S(4%) and ZnO:S(8%), respectively. While the extreme value of roughness of ZnO:S(4%) film may due to the normal condition, the ZnS roughness of 0.388 nm demonstrates that the introduction of S element results a smooth surfaces. The optical band gaps of 3.20, 3.22 and 3.12 eV, for ZnO:S(2%), ZnO:S(4%) and ZnO:S(8%) films, respectively, were smaller than the band gap of 3.27 eV of pure ZnO demonstrating

the effect of S dopants on the band gap of ZnO material. The band gap of spin-coated ZnS film was 3.8 eV and was similar to the reported value for hexagonal ZnS structure.

References

[1] Özgür, Ümit, et al. "Zinc Oxide Materials and Devices Grown by Molecular Beam Epitaxy." Molecular Beam Epitaxy, 2018, pp. 343–375, doi:10.1016/b978-0-12-812136-8.00016-5.

[2] Ichino, K., et al. "ZnS:N and ZnS:N,Ag Grown by Molecular Beam Epitaxy." Physica Status Solidi C, vol. 7, no. 6 (2010) pp. 1504 - 1506, doi:10.1002/pssc.200983239.

[3] Müller, Raphael, et al. "Chemical Vapor Deposition Growth of Zinc Oxide on Sapphire with Methane: Initial Crystal Formation Process." Crystal Growth & Design, vol. 19, no. 9, 16 July 2019, pp. 4964 – 4969.

[4] Zhenyi, Fang, et al. "CVD Growth of Bulk Polycrystalline ZnS and Its Optical Properties." Journal of Crystal Growth, vol. 237–239, Apr. 2002, pp. 1707–1710.

[5] Thote, Abhishek, et al. "High-Working-Pressure Sputtering of ZnO for Stable and Efficient Perovskite Solar Cells." ACS Applied Electronic Materials, vol. 1, no. 3 (2019) pp. 389 - 396.

[6] Hwang, Dong Hyun, et al. "Structural and Optical Properties of ZnS Thin Films Deposited by RF Magnetron Sputtering." Nanoscale Research Letters, vol. 7, no. 1, 5 Jan. 2012.

[7] Kurtaran, Sema. "Al Doped ZnO Thin Films Obtained by Spray Pyrolysis Technique: Influence of Different Annealing Time." Optical Materials, vol. 114, Apr. 2021, p. 110908.

[8] López, M.C., et al. "Growth of ZnS Thin Films Obtained by Chemical Spray Pyrolysis: The Influence of Precursors." Journal of Crystal Growth, vol. 285, no. 1–2, Nov. 2005, pp. 66–75.

[9] Winkler, Nina, et al. "MG-Doped ZnO Films Prepared by Chemical Bath Deposition." Journal of Materials Science, vol. 53, no. 7, 3 Jan. 2018, pp. 5159–5171.

[10] Wei, Aixiang, et al. "Preparation and Characterization of ZnS Thin Films Prepared by Chemical Bath Deposition." Materials Science in Semiconductor Processing, vol. 16, no. 6, Dec. 2013, pp. 1478–1484, doi: 10.1016/j.mssp.2013.03.016.

[11] Vignesh, K, et al. "Synthesis and Characterization ZnO Nanoparticles Using Sol-Gel Method and Their Antibacterial Study." IOP Conference Series: Materials Science and Engineering, vol. 1219, no. 1, 1 Jan. 2022, p. 012019, doi:10.1088/1757-899x/1219/1/012019.

[12] Khan, M.I., et al. "Characterizations of Multilayer ZnO Thin Films Deposited by Sol-Gel Spin Coating Technique." Results in Physics, vol. 7, 2017, pp. 651–655, doi: 10.1016/j.rinp.2016.12.029.

[13] Mursal, et al. “Structural and Optical Properties of Zinc Oxide (ZnO) Based Thin Films Deposited by Sol-Gel Spin Coating Method.” Journal of Physics: Conference Series, vol. 1116, Dec. 2018, p. 032020, doi:10.1088/1742-6596/1116/3/032020.

[14] Zaman, M. Burhanuz, et al. “Synthesis and Characterization of Spin-Coated ZnS Thin Films.” AIP Conference Proceedings, 2018, doi:10.1063/1.5033002.

[15] Ayana, Dawit Gemechu. “Synthesis and Characterization of Sol-Gel Derived ZnO Thin Films for Memristive Applications.” Synthesis and Characterization of Sol-Gel Derived ZnO Thin Films for Memristive Applications, Thesis / Dissertation ETD, University of Trento, 2017.

[16] Natsume, Y. and H. Sakata. "Zinc Oxide Films Prepared by Sol-Gel Spin-Coating." Thin Solid Films, vol. 372, no. 1-2, 2000, pp. 30-36.

[17] Cullity, B.D., Stock, S.R., (2010). Elements of X-Ray Diffraction., edited by Pearson New International Edition. ISBN 13: 978-1-292-04054-7.

[18] Shan, F. K. et al. "Blueshift of near Band Edge Emission in Mg Doped ZnO Thin Films and Aging." Journal of Applied Physics, vol. 95, no. 9, 2004, pp. 4772-4776, doi:10.1063/1.1690091.

[19] Zegadi, Chewki et al. "Influence of Sn Low Doping on the Morphological, Structural and Optical Properties of ZnO Films Deposited by Sol Gel Dip-Coating." Advances in Materials Physics and Chemistry, vol. 04, no. 05, 2014, pp. 93-104.

[20] Rouchdi, M. et al. “Synthesis and characteristics of Mg doped ZnO thin films: Experimental and ab-initio study, Results Phys. vol.7, 2017, pp. 620-627.

[21] Williamson, G. K. and R. E. Smallman. "Iii. Dislocation Densities in Some Annealed and Cold-Worked Metals from Measurements on the X-Ray Debye-Scherrer Spectrum." Philosophical Magazine, vol. 1, no. 1, 1956, pp. 34-46.

[22] Basnet, Parita et al. "Assessment of Synthesis Approaches for Tuning the Photocatalytic Property of ZnO Nanoparticles." SN Applied Sciences, vol. 1, no. 6, 2019.

[23] Singh, A. and H. L. Vishwakarma. "Study of Structural, Morphological, Optical and Electroluminescent Properties of Undoped ZnO Nanorods Grown by a Simple Chemical Precipitation." Materials Science-Poland, vol. 33, no. 4, 2015, pp. 751-759.

[24] Makula, P. et al. "How to Correctly Determine the Band Gap Energy of Modified Semiconductor Photocatalysts Based on Uv-Vis Spectra." J Phys Chem Lett, vol. 9, no. 23, 2018, pp. 6814-6817, doi: 10.1021/acs.jpclett.8b02892.

[25] Wang, Jinzhong et al. "Effect of Annealing on the Properties of N-Doped ZnO Films Deposited by Rf Magnetron Sputtering." Applied Surface Science, vol. 254, no. 22, 2008, pp. 7178-7182. doi: 10.1016/j.apsusc.2008.05.321

[26] Abraham, Paulosutty et al. "(002) Oriented ZnO and ZnO:S Thin Films by Direct Ultrasonic Spray Pyrolysis: A Comparative Analysis of Structure, Morphology and Physical Properties." Materials Today Communications, vol. 35, 2023.

[27] Della Gaspera, E. et al. "Augmented Band Gap Tunability in Indium-Doped Zinc Sulfide Nanocrystals." Nanoscale, vol. 11, no. 7, 2019, pp. 3154-3163.

[28] Mamat, M. H. et al. "Influence of Doping Concentrations on the Aluminum Doped Zinc Oxide Thin Films Properties for Ultraviolet Photoconductive Sensor Applications." Optical Materials, vol. 32, no. 6, 2010, pp. 696-699.

General conclusion and perspectives

General conclusion and perspectives

This study focuses on exploring CZTS thin-film solar cells. The investigation begins with numerical modeling of conventional CZTS solar cells and includes the proposal of various layer materials, parameter optimizations, and structural configurations. Additionally, the experimental aspect is addressed by detailing transparent conductive oxide (TCO) films employed in CZTS solar cells as buffer or window layers. The goal is to examine the structural, optical, and electrical properties of these films through theoretical and experimental studies, with the intention of utilizing them in photovoltaic applications.

After briefly examining numerical methods for solar cell modeling and techniques for parameter extraction, our attention shifted to the structure of CZTS solar cells. Initially, we calculated the photovoltaic characteristics of the conventional substrate Metal/CZTS/CdS/ZnO/ZnO:Al solar cell. Substantial performance enhancement in cell efficiency is anticipated by incorporating In_2S_3 or Zn(O,S) as a buffer layer. Notably, efficiencies of 14.28% and 13.88% were achieved, respectively. We introduced a promising design for CZTS bifacial solar cells and investigated the impact of the barrier height at the p-CZTS/n-TCO interface in ZnO:Al/CdS/CZTS/TCO/SLG solar cells under both front and backside AM1.5G illuminations. Several key observations emerged for each illumination scenario. Under front side illumination, the optimal CZTS absorber layer thickness of 2 µm demonstrated a notable enhancement in performance, particularly in short-circuit current density (J_{SC}). This improvement suggests that the high energy barrier at the CZTS/TCO interface led to a significant degradation in bifacial solar cell performance, primarily attributed to a reduction in short-circuit current density. This observation was further confirmed by external quantum efficiency measurements. Simulation results indicated that maintaining the energy barrier height at ≤ 0.5 eV can enhance open-circuit voltage (V_{oc}), fill factor (FF), and overall efficiency for a 2 µm CZTS thickness with $N_A(\text{CZTS}) = 2 \times 10^{16}$ cm^{-3}. The bifacial CZTS solar cell, featuring a low energy barrier, achieved an efficiency of approximately 4.5% under AM1.5G backside illumination. Additionally, the best internal quantum efficiency reached around 40% in the visible range. Finally, we will explore the applications of (TCOs) as an intermediate layer in tandem CZTS/CZTSe solar cells. The optimal photovoltaic parameters derived from this study include $\eta = 19.94\%$, FF = 82.62%,

VOC = 1.46 V, and JSC = 16.5 mA/cm² for CZTS and CZTSe layers with thicknesses of 1.25 µm and 1.3 µm, respectively.

In the second section, the DFT method is employed to scrutinize the structure, electronic, and optoelectronic properties of the $ZnS_{1-x}O_x$ system. The $ZnS_{1-x}O_x$ alloy exhibits anisotropic optical parameters, with a band gap ranging from 2.5 eV to 3.6 eV. The refractive index plays a crucial role as photons traverse the material, especially in cases of covalent atomic bonds. The static refractive index experiences a decrease from 2.1 to 1.5 as the oxygen content *x* increases from 0 to 1. Both in-plane and out-of-plane extinction coefficients initiate at an energy corresponding to the direct band gap value of the $ZnS_{1-x}O_x$ alloy. $ZnS_{1-x}O_x$ demonstrates UV light absorption within the 4 eV to 10 eV range, validating its potential for use in optical and photovoltaic devices due to its band gap properties.

Finally, our focus shifted to fabricate pure ZnO, Sulfur-doped ZnO, and ZnS thin films onto glass substrates using the Sol-Gel spin-coating method. The spin-coated pure ZnO film exhibited conventional characteristics, such as a 3.27 eV band gap and a hexagonal wurtzite structure. Although all spin-coated S-doped ZnO (with 2%, 4%, 8%) thin films retained the same hexagonal wurtzite structure, they displayed larger crystallite sizes ranging from 42.2875 to 49.5074 nm, in contrast to the smaller size (38.43 nm) of pure ZnO crystals.

Furthermore, the spin-coated ZnS film exhibited a hexagonal structure with a crystallite size of 42.49 nm, indicating that the introduction of S element through the spin-coating process led to an increase in crystal size within the structure of binary compounds of Zn, O, and S elements. The S dopants had a notable impact on the morphology of spin-coated pure ZnO and S-doped ZnO thin films, particularly on their roughness. While the extreme value of roughness in the ZnO:S(4%) thin film may be attributed to normal conditions, the ZnS film demonstrated a low roughness of 0.388 nm, highlighting that the introduction of S element resulted in a smooth surface.

The optical band gaps for ZnO:S(2%), ZnO:S(4%), and ZnO:S(8%) thin films were measured at 3.20, 3.22, and 3.12 eV, respectively, which were smaller than the band gap of 3.27 eV observed in pure ZnO. This difference underscores the influence of S dopants on the band gap of ZnO material. The band gap of the spin-coated ZnS film was determined to be 3.8 eV, aligning closely with the reported value for a hexagonal ZnS structure.

Ultimately, various perspectives can be considered to enhance the completion of this work. Firstly, additional characterizations on the deposited films, such as Scanning Electron Microscopy (SEM), Hall effect measurements, and Energy Dispersive X-ray Spectroscopy

(EDX), could be conducted. These characterizations aim to extract more parameters that can contribute to the theoretical modeling of CZTS solar cells. Furthermore, the incorporation of alternative deposition techniques, such as electrochemical and deep coating methods, is essential to achieve a good quality TCO and/or CZTS layers.

Publications and conferences

Publications

[1] Bouchama, Idris and **Salim Ali-Saoucha**. "Effect of Wide Band-Gap TCO Properties on the Bifacial CZTS Thin-Films Solar Cells Performances." Optik, vol. 144, 2017, pp. 370-377, doi:10.1016/j.ijleo.2017.07.009.

[2] **Saoucha, S. A**. et al. "Effect of Oxygen Content on Structural and Optoelectronic Properties of $ZnS_{1-x}O_x$ Alloy in the Wurtzite Structure." Solid State Communications, vol. 354, 2022, doi:10.1016/j.ssc.2022.114897.

International Conferences

[1] A. Mekhannene, **S.Ali Saoucha**, I.Bouchama , "Effect of Environmental Conditions on the Substrate Cu(In,Ga)Se2 Solar Cell Performances", FICSE 2015, Bordj Bou-Arreridj.

[2] **S. Ali Saoucha**, Bouchama Idris, Samah Boudour, Nowshad Amin, "Properties of electronic potential barriers of superstrate InSe/ODC/CIGS solar cells using one-dimensional model", IS-TCM2016, Greece.

National Conferences

[1] **S.Ali Saoucha**, I.Bouchama, A.bouloufa, "Extraction of Solar Cell Parameters Based on Single Diode Model ", NCENT'2015, M'sila.

ملخص

ركزت هذه الاطروحة على دراسة الطبقات الرقيقة التي تدخل في صناعة الخلايا الشمسية المبنية على رقائق (CZTS) من الناحية النظرية باستعمال برنامجي (Silvaco) و (AMPS-1D) بمحاكات مختلف التركيبات الممكنة (أحادية الوجه، ثنائية الوجه، الترادفية) مع التركيز على ميزات رقائق الاوكسيد الناقل واستعمالاته كوجه شفاف او نافذة أو كطبقة وسيطة، كما تم باستعمال برنامج (Wien2k) حساب مختلف الخصائص الكهربائية و الضوئية لمركب (ZnO_xS_{1-x}) ، ومن الناحية التطبيقية تم ترسيب رقائق من مركب (ZnO) و (ZnO) و(ZnO) بنسب 2%،4%،8% باستعمال تقنية الطرد المركزي للمحلول الهلامي ،وتحديد خصائصها الهيكلية والمورفولوجية والبصرية باستعمال تحليل انحراف الاشعة السينية (DRX) و مجهر القوة الذرية (AFM) و مطيافية الأشعة المرئية وفوق البنفسجية (UV-vis).

الكلمات المفتاحية: الخلايا الشمسية، الطبقات الرقيقة، كبريت الزنك، أكسيد الزنك، التطعيم.

Abstract

This study primarily investigates CZTS thin-film solar cells. We employ numerical modeling through Silvaco Atlas and AMPS-1D software to analyze CZTS solar cells, including substrate, bifacial, and tandem configurations. A notable aspect of our research involves proposing an innovative design for CZTS bifacial solar cells. We specifically examine the influence of the barrier height at the p-CZTS/n-TCO interface in the structure ZnO:Al/CdS/CZTS/TCO/SLG. The efficiency results reveal 15.8% under front-side illumination and 4% under back-side illumination. In the subsequent section, we utilize the Density Functional Theory (DFT) method to scrutinize the structure, electronic, and optic properties of the ZnS1-xOx alloy. Shifting our focus to experimentation, we employ the Sol-Gel spin-coating method to fabricate pure ZnO, sulfur-doped ZnO, and ZnS thin films. The spin-coated films are characterized by analyzing their structural, morphological, and optical properties through techniques such as X-ray diffraction (XRD), Atomic Force Microscopy (AFM), and UV-VIS spectroscopy.

Keywords: solar cells, thin films, ZnO, ZnS, ZnO:S, Silvaco, AMPS-1D.

Résumé :

Cette thèse se concentre sur les cellules solaires à base de CZTS. Nous servant des logiciels Silvaco_Atlas et AMPS-1D pour modéliser numériquement les cellules solaires à CZTS (substrat, bifaciales et tandem). Nous examinons spécifiquement l'influence de la hauteur de la barrière à l'interface p-CZTS/n-TCO dans la structure ZnO:Al/CdS/CZTS/TCO/SLG. L'efficacité révèlent 15,8% sous illumination direct et 4% sous illumination du côté arrière. Puis, nous utilisons la Théorie de la Fonctionnelle de la Densité (DFT) pour examiner la structure, les propriétés électroniques et optiques de l'alliage $ZnS_{1-x}O_x$. Pour le coté expérimentale, nous utilisons la méthode de dépôt par centrifugation Sol-Gel pour fabriquer des couches minces de ZnO pur, de ZnO dopé au soufre et de ZnS. Les films déposés sont caractérisés en analysant leurs propriétés structurales, morphologiques et optiques à l'aide de techniques telles que la diffraction des rayons X (DRX), la microscopie à force atomique (AFM) et la spectroscopie UV-VIS.

Mots clés : cellules solaires, couches minces, ZnO, ZnS, ZnO:S, Silvaco, AMPS-1D.